The Physics and Applications of a 3D Plasmonic Nanostructure

A Thesis

Submitted to the Faculty

of

Drexel University

by

Brandon B. Terranova

In partial fulfillment of the

requirements for the degree

of

Doctor of Philosophy

November 2015

ACKNOWLEDGEMENTS

I want to first thank my wife Jocelyn for standing by me through all of my self-exploration, and listening to me talk about plasmonics and Fano resonances all the time. Next, my advisor Dr. Adam Fontecchio has been very patient and generous with me throughout the PhD process, has provided me with all the resources I needed for my studies, and has believed in me and treated me as an equal since the day we met. Many others are to thank for all their assistance, such as my lab mates, several undergraduate students, and Chad Eichfeld at Penn State's nanofabrication facility. Lastly, I want to acknowledge my son, Chance Maxwell Terranova, who has inspired me in many ways throughout the final years of the PhD program.

TABLE OF CONTENTS

LIST OF TABLES

LIST OF FIGURES

ABSTRACT

The Physics and Applications of a 3D Plasmonic Nanostructure

Brandon B. Terranova
Adam K. Fontecchio, Ph.D.

In this work, the dynamics of electromagnetic field interactions with free electrons in a 3D metallic nanostructure is evaluated theoretically. This dissertation starts by reviewing the relevant fundamentals of plasmonics and modern applications of plasmonic systems. Then, motivated by the need to have a simpler way of understanding the surface charge dynamics on complex plasmonic nanostructures, a new plasmon hybridization tree method is introduced. This method provides the plasmonicist with an intuitive way to determine the response of free electrons to incident light in complex nanostructures within the electrostatic regime. Next, a novel 3D plasmonic nanostructure utilizing reflective plasmonic coupling is designed to perform biosensing and plasmonic tweezing applications. By applying analytical and numerical methods, the effectiveness of this nanostructure at performing these applications is determined from the plasmonic response of the nanostructure to an excitation beam of coherent light. During this analysis, it was discovered that under certain conditions, this 3D nanostructure exhibits a plasmonic Fano resonance resulting from the interference of an in-plane dark mode and an out-of-plane bright mode. In evaluating this nanostructure for sensing changes in the local dielectric environment, a figure of merit of 68 is calculated, which is competitive with current localized surface plasmon resonance refractometric sensors. By evaluating the Maxwell stress tensor on a test particle in the vicinity of the nanostructure, it was found that under

the right conditions, this plasmonic nanostructure design is capable of imparting forces greater than 10.5 nN on dielectric objects of nanoscale dimensions.

The results obtained in these studies provides new routes to the design and engineering of 3D plasmonic nanostructures and Fano resonances in these systems. In addition, the nanostructure presented in this work and the design principles it utilizes have shown performance metrics which make it an important contribution to the fields of LSPR biosensing and plasmonic trapping and force transduction.

CHAPTER 1: INTRODUCTION

§1.1 MOTIVATION

The aim of this dissertation is to numerically and analytically evaluate a quasi-three dimensional plasmonic nanostructure for the applications of refractometric sensing and plasmonic force transduction.

The study of plasmonics has evolved from a scientific novelty to having broad-reaching applications. Plasmonic systems have been designed to perform myriad functions ranging from applications in the research laboratory to biosensing and even aerospace propulsion systems. Plasmonics offers a way of breaking the diffraction limit encountered when using classical optics systems, and the strong electric field confinement possible within metallic nanostructures opens the door to extreme light focusing, high sensitivity to changes in refractive index, amplification of weak molecular signals, enhancement of catalytic reactions, selective heating of nanoscopic regions, enhanced near-field heat transfer, highly sensitive spectroscopies, nanoscale signal guidance, lasing, nanoscopic particle confinement, negative index of refraction, targeted infrared cancer therapies, and electromagnetically induced transparency or "cloaking" applications.

The work presented in this dissertation is focused on the evaluation of a particular three-dimensional plasmonic nanostructure which has applications specifically in the areas of biosensing and plasmonic force transduction. The work done on the passive nanostructure presented here serves as an example of how to take a plasmonic nanostructure design from concept to prototype. Using numerical simulations, it is shown that the nanostructure designed is suited for multiple applications, and the careful evaluation of the structure's plasmonics reveals new insights into the behavior of plasmonic nanostructures which extend out of the plane of the substrate.

§1.2 A BRIEF HISTORY OF PLASMONICS

James Clerk Maxwell's first major discovery was the creation of the world's first color photograph in the year 1861. This achievement, while monumental, was overshadowed by his historical synthesis four years later. In his 1865 treatise *A Dynamical Theory of the Electromagnetic Field*, Maxwell was able to correctly formulate the fundamental classical equations of electrodynamics.[1] Shown here in their modern Heaviside-Lorentz form, Maxwell's equations, which fully describe electrodynamics and electromagnetism on the microscale and larger, are now expressed in the following form:

$$\boldsymbol{\nabla} \cdot \boldsymbol{E} = \rho \tag{1}$$

$$\boldsymbol{\nabla} \cdot \boldsymbol{B} = 0 \tag{2}$$

$$\boldsymbol{\nabla} \times \boldsymbol{E} = -\frac{\partial \boldsymbol{B}}{\partial t} \tag{3}$$

$$\boldsymbol{\nabla} \times \boldsymbol{H} = \boldsymbol{J} + \frac{\partial \boldsymbol{D}}{\partial \mathrm{t}} \tag{4}$$

This set of equations has been the backbone of electrophysics and electrical engineering work since their inception. In fact, nearly a century after Maxwell wrote down these now famous equations, Rufus Ritche predicted a new type of material excitation known as a plasmon (coined by Ritche himself) by using Gauss' law (equation (1)) in 1957.[2] The bulk plasmons Ritche found were the result of investigating the origins of electron energy loss in experiments with fast electrons passing through thin metallic foils.

Before plasmons were discovered and described mathematically, artisans from the 4th century AD knew of the optically transformative powers of metallic "dust" when painted onto glass substrates to create "stained glass". One of the earliest and most famous examples of this technique is found in the Roman style cage-cup known as the Lycurgus cup, shown in Figure 1. Although unknown at the time, the mechanism for the emergence of the colors observed in the glass upon illumination is due to the electromagnetically induced oscillations of the free electrons on the surface of the spherical metallic nanoparticles embedded in the glass.

Figure 1: Lycurgus cup shown with external illumination (left) and internal illumination (right).

Normally, the electron oscillations on a large metallic surface prohibit the light from penetrating the metallic surface beyond the "skin depth" of the material by phase shifting the incoming radiation; however, due to the subwavelength size of the nanospheres, delocalized electrons on their surface instead are forced to oscillate collectively (surface plasmons) at certain frequencies, thus absorbing and scattering light differently (amplifying and damping) for different frequencies of the incident electromagnetic (EM) field. The curved surface of the nanospheres creates a spatially curved distribution of positive ion cores which in turn generate a restoring force against the driven surface electrons. It is therefore apparent that the geometry of the metallic nanostructure influences resonances inside and outside the nanoparticle and thus their associated field amplifications. These geometrically dependent surface excitations are referred to as localized surface plasmons (LSPs).

In contrast to the spatially confined LSPs, when the conditions are right, light can couple to these surface plasmons to create surface plasmon polariton (SPP) quasiparticles which can be considered as dressed electromagnetic waves. Although not fully understood at the time, the first observation of SPPs was in 1902 by Robert W. Wood, who correctly attributed the effect to the presence of a grating in his observations, stating "…there may be something akin to resonance in the action of this grating".[3] The first experimental realization of SPPs came in 1968, when Andreas Otto was able to successfully excite SPPs (called surface plasmon waves at the time) on smooth surfaces by taking advantage of phase matching techniques through the fastidious arrangement of insulators of different dielectric constants now known as the Otto configuration shown in Figure 2a.[4] Three years later, an analogous configuration was created to excite SPPs by Erwin Kretschmann shown in Figure 2b.[5]

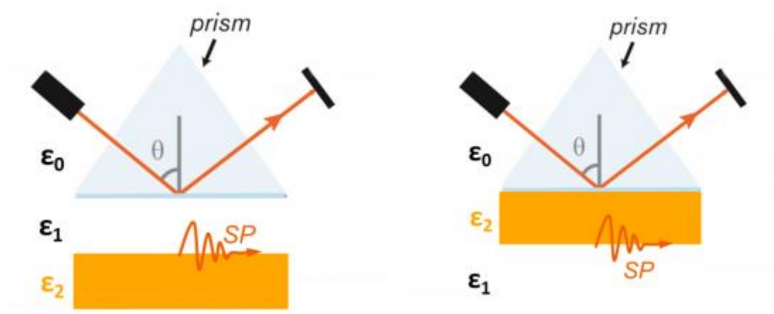

(a) (b)

Figure 2: a) Otto configuration; b) Kretschmann configuration.

§1.3 METAL OPTICS

Metals can be thought of as a lattice of fixed positive nuclei within a sea of free electrons swimming around them. These conduction electrons can be well described mathematically using the plasma model over a wide frequency range. This method is valid for alkali metals up to ultraviolet frequencies, but for noble metals, interband transitions at visible frequencies invalidate this approach. The plasma model describes the free electron's response to an externally applied field by considering the electrons as damped simple harmonic oscillators. Assuming the driving field has a harmonic time dependence, $\boldsymbol{E}(t) = \boldsymbol{E}_0 e^{-i\omega t}$, we can write the equation of motion for an electron in the plasma sea with the damping term γ equal to the inverse of the relaxation time τ, which is typically on the order of 10^{-14} s at room temperature:

$$m\ddot{\boldsymbol{x}}(t) + m\gamma\dot{\boldsymbol{x}}(t) = -e\boldsymbol{E}(t). \tag{5}$$

Where m and e are the mass and charge of the electron respectively. Substituting a particular solution of this equation, $\boldsymbol{x}(t) = \boldsymbol{x}_0 e^{-i\omega t}$, we arrive at

$$\boldsymbol{x}(t) = \frac{e}{m(\omega^2 + i\gamma\omega)}\boldsymbol{E}(t). \tag{6}$$

Using the definition of macroscopic polarization density written as the product of the electron density with the charge displacement in the material, $\boldsymbol{P} = -n_e e\boldsymbol{x}$, and the definitions of the electric displacement, $\boldsymbol{D} = \varepsilon_0\boldsymbol{E} + \boldsymbol{P}$ and $\boldsymbol{D} = \varepsilon(\omega)\boldsymbol{E}$, and the plasma frequency of the free electron gas, $\omega_p^2 = \frac{n_e e^2}{\varepsilon_0 m}$, we now arrive at the dielectric function of the free electron gas in the plasma model:

$$\varepsilon(\omega) = 1 - \frac{\omega_p^2}{\omega^2 + i\gamma\omega}. \tag{7}$$

This complex dielectric function, or permittivity, can be used to predict the dispersion behavior of plasmons in most metallic systems. In the case of large frequencies close to the plasma frequency, $\omega\tau \gg 1$, so that damping becomes negligible, and equation (7) becomes

$$\varepsilon(\omega) = 1 - \frac{\omega_p^2}{\omega^2}. \tag{8}$$

As the dispersion relation of EM fields can be determined from $k^2 = \frac{\varepsilon\omega^2}{c^2}$, the dispersion of traveling EM fields in a free electron gas within this frequency regime is thus

$$\omega(k) = \sqrt{\omega_p^2 + k^2c^2}. \tag{9}$$

As shown in Figure 3, the propagation of transverse electromagnetic waves in a free electron gas is prohibited below the plasma frequency. For frequencies above ω_p, longitudinal waves propagate with a group velocity $v_g = \frac{d\omega}{dk} < c$.

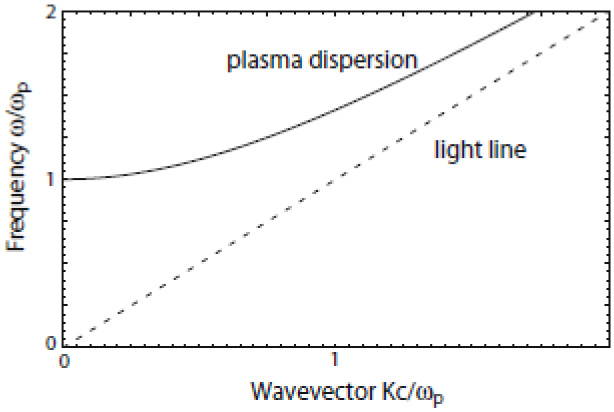

Figure 3: Dispersion in the plasma model. Transverse wave propagation is forbidden for $\omega < \omega_p$. [6]

§1.4 SPPs AT METAL/INSULATOR INTERFACES

At a simple planar interface between positive and negative permittivity materials, SPPs can propagate as long as the SPP propagation wavevector β is greater than the wavevector in the dielectric. Figure 4 shows the simplest spatial configuration of materials which support SPPs. For metals satisfying the condition $\mathrm{Re}\{\varepsilon_1(\omega)\} < 0$, excited transverse magnetic (TM) SPP modes can exist and travel along the interface. However, excitations of SPPs on a smooth planar interface such as this are not possible with a three dimensional beam from a far field source unless phase matching techniques are employed such as is done in the Otto and Kretschmann configurations.

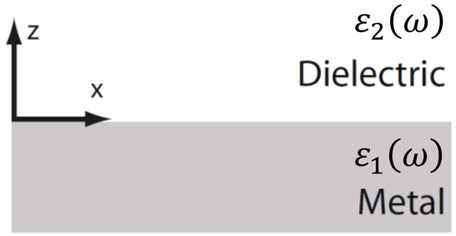

Figure 4: Metal/insulator interface geometry.

We can fully quantify the dynamics of EM fields confined to the metal surface by solving the EM wave equation

$$\nabla^2 \boldsymbol{E} - \frac{\varepsilon}{c^2}\frac{\partial^2 \boldsymbol{E}}{\partial t^2} = 0 \tag{10}$$

using appropriate boundary conditions. Again assuming a harmonic time dependence of the EM wave, $\boldsymbol{E}(t) = \boldsymbol{E}_0 e^{-i\omega t}$, we can recast equation (10) as the Helmholtz equation:

$$\nabla^2 \boldsymbol{E} - k_0^2 \varepsilon \boldsymbol{E} = 0 \tag{11}$$

where $k_0 = \frac{\omega}{c}$ is the wave vector of the propagating wave in vacuum. Assuming the EM waves propagate along the x-direction of a cartesian coordinate system, we can write the total wave vector as

$$k = \sqrt{k_x^2 + k_y^2 + k_z^2}, \tag{12}$$

and using the complex propagation constant $\beta = k_x$, the Helmholtz equation describing the electric field of the EM wave is now

$$\frac{\partial^2 \boldsymbol{E}(z)}{\partial z^2} + (k_0^2 \varepsilon - \beta^2)\boldsymbol{E}(z) = 0. \tag{13}$$

There is of course an analogous equation for the magnetic field as well. Using equations (3) and (4) we can arrive at a set of six coupled equations from which three represent the TM modes and the other three the transverse electric (TE) modes. Since SPPs can only exist as TM modes (since the divergence free nature of the H-field requires the in-plane component of the magnetic field to have opposite directions above and below the interface, prohibiting continuity at the boundary [6]), we are left with these two equations:

$$E_x = -\frac{i}{\omega\varepsilon_0\varepsilon}\frac{\partial H_y}{\partial z} \tag{14}$$

$$E_z = -\frac{\beta}{\omega\varepsilon_0\varepsilon}H_y \tag{15}$$

since only the E_x, E_z, and H_y components are non-zero for TM modes traveling in the *x*-direction within the *xy*-plane. Using these relationships we can now arrive at the wave equation for SPP TM modes:

$$\frac{\partial^2 H_y}{\partial z^2} + (k_0^2\varepsilon - \beta^2)H_y = 0. \tag{16}$$

Applying equations (14), (15), and (16) to the regions $z > 0$ and $z < 0$, and noting H_y and $\varepsilon_i E_z$ (i = 1, 2) are continuous at the interface, we arrive at

$$\frac{k_2}{k_1} = -\frac{\varepsilon_2}{\varepsilon_1} \tag{17}$$

Inserting the expression for H_y into the wave equation (16), we now have

$$k_1^2 = \beta^2 - k_0^2\varepsilon_1 \tag{18}$$

$$k_2^2 = \beta^2 - k_0^2\varepsilon_2 \tag{19}$$

Combining this with equation (17), we arrive at the full dispersion relation of SPPs propagating at the simple planar interface between the metal and the insulator:

$$\beta = k_0\sqrt{\frac{\varepsilon_1\varepsilon_2}{\varepsilon_1 + \varepsilon_2}}. \tag{20}$$

This equation completely describes the spatial and temporal dynamics of SPPs confined to a perfectly flat planar interface between two materials having permittivities of differing sign.

§1.5 SURFACE PLASMON POLARITONS IN MIM STRUCTURES

Relevant to work contained in this thesis, we will now describe the dispersion behavior of SPPs in a simple metal-insulator-metal (MIM) heterostructure configuration as depicted in Figure 5. Using the process outlined in the previous section, we arrive at the dispersion relation for this structure:

$$\tanh k_1 d = -\frac{k_2 \varepsilon_1}{k_1 \varepsilon_2} \tag{21}$$

$$\tanh k_1 d = -\frac{k_1 \varepsilon_2}{k_2 \varepsilon_1}. \tag{22}$$

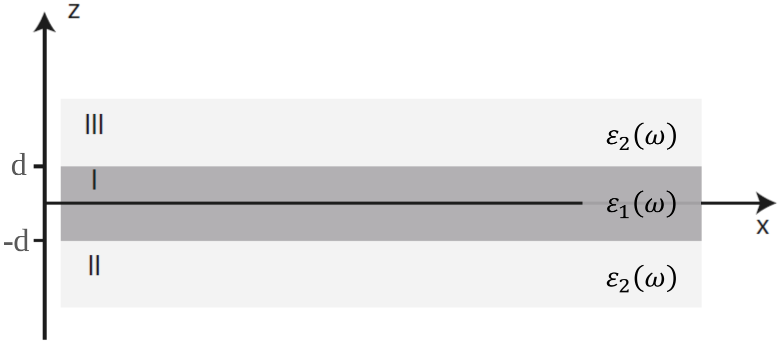

Figure 5: MIM geometry.

This particular geometry allows for modes with opposite vector parity. Equations (21) and (22) describe the anti-symmetric and symmetric modes respectively. The MIM geometry allows for extreme concentration of fields within the dielectric layer, allowing for stronger energy confinement and large propagation constants. The MIM geometry supports modes which propagate along the interfaces of the dielectric layer, and allow for very large propagation vectors as the gap width decreases, as seen in Figure 6 which shows the dispersion of SPPs in a Ag/SiO$_2$/Ag MIM heterostructure.

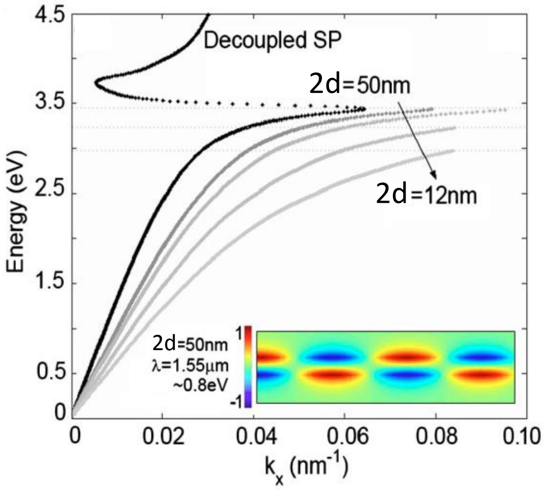

Figure 6: MIM anti-symmetric modes for various dielectric thicknesses and subplot showing associated electric field distribution.[7]

§1.6 EXCITATION OF SURFACE PLASMON POLARITONS

As mentioned briefly in the discussion on the nanoparticles in the Lycurgus cup, it is possible to excite plasmons by shining light onto metallic nanostructures. The LSPs on those nanospheres arise from the electric field of the incident light pushing on the free electrons on the surface, and the curved distribution of charges on the sphere pushes back, establishing a resonance condition. Later in this dissertation we will learn that the geometry of a nanostructure plays a central role in the dynamics of localized and propagating plasmons alike. In the previous two sections, we investigated the spatial and temporal properties of SPPs at one and two interfaces, but we did not discuss how the SPPs were excited in the first place. Experimentally, the excitation of SPPs can be achieved via charged particle impact, as was seen in the electron energy loss experiments studied by Ritche as discussed earlier, however more modern techniques use a specially designed experimental apparatus such as the Otto or Kretschmann configurations as shown in Figure 2, or carefully prepared excitation beams which permit phase matching conditions at the metal-dielectric interface.

Since SPP field confinement is due to the fact that $\beta \gg k_d$ at the surface plasmon frequency, in order to achieve phase matching conditions for plasmon resonance, one must chose an excitation method that increases the amplitude of the incident beam's wavevector component at the metal-dielectric interface. Normal p-polarized light cannot excite SPPs at smooth planar interfaces, as expected—by the fact that the bound plasmons lie to the right of the light-line in the dispersion plot for the planar interface.

§1.7 CONTRIBUTIONS AND SCOPE OF THIS THESIS

This work encompasses several areas of plasmonics, with a focus on the application-specific design of nanostructures and the investigation of their response to external electromagnetic fields. The 3D plasmonic design presented in this work is analyzed via numerical simulation, analytical evaluation, and experimental verification methods. In the next chapter, an overview is given describing the current state of the art in the areas relevant to the research contained in this dissertation. In chapter 3, the design and optimization of a new plasmonic nanostructure appropriate for biosensing and trapping applications is introduced. Preliminary numerical simulations and hybridization diagrams are shown to guide the design process. In this chapter, plasmon hybridization trees are introduced to simplify the evaluation of the dipolar plasmonic response of complex plasmonic nanostructures in the static limit. In chapter 4, we study the various resonances in the nanostructure that was introduced in chapter 3, and discuss the discovery of a novel out-of-plane Fano resonance in the nanostructure. Chapter 5 details a numerical study of the coaxial nanopillar introduced in chapter 3 for use as a biosensor, and it is shown that a high figure of merit is obtained for the nanostructure under investigation.[8] Chapter 6 deals with the evaluation of the nanostructure for trapping applications, including a derivation of an expression for the force resulting from plasmons within an infinite coaxial cable as well as numerical results indicating a longitudinal force component which is two to three orders of magnitude greater than most other plasmonic trapping systems.[8] Lastly, chapter 7 provides an overview of the contributions of this dissertation.

CHAPTER 2: CURRENT STATE OF THE ART

§2.1 MODERN RESEARCH METHODS IN PLASMONICS

The design and evaluation of plasmonic systems for research and for engineering applications is dependent on the current tools available to the plasmonicist. In this chapter we will briefly review the current computational and experimental methods used for the design and evaluation of plasmonic systems, and finish the chapter by discussing the applications of plasmonic systems relevant to the work completed in this dissertation.

§2.1.1 COMPUTATIONAL ELECTROMAGNETICS

Most areas of engineering design currently rely on computer aided design (CAD) and subsequent computer simulation of physics in these designs. Plasmonic nanostructures can likewise be designed using CAD software and simulated with various computational electromagnetic solvers. Simply stated, the full dynamics of any electromagnetic system on the nanoscale to the macroscale can be represented accurately by solving Maxwell's equations on a grid. The difficulty that arises is dealing with the various reflections, refractions, and diffractions which occur in modeled systems. The vectorial nature of the boundary conditions and the size-dependent computational time are also other factors which present difficulties. The first computational method used to simulate EM fields was an integral-based solution technique, which provides extremely accurate solutions for scattering problems, but are less appealing for broadband simulations, and problems including transmission through materials, complex materials, and random effects.[9] Integral equation solvers include the discrete dipole approximation (DDA) which uses an integral form of Maxwell's equations solved over a finite array of polarizable dipole points as an approximation to the continuum of the simulated object. Another integral method is the method of moments (MoM) or boundary element method (BEM). The BEM is a popular integral equation solver, as it overcomes some of the limitations of the DDA method, however due to the fact that this method relies on calculated only boundary values, it is implicitly limited in the generality of problems it can be applied to. There are a few other integral methods such as the fast multipole method and the partial element equivalent circuit method, but these are outside the scope of this thesis, and we will now instead focus on finite element techniques.

Although computationally more demanding, finite element techniques solve Maxwell's equations on triangulated nodes on a mesh covering a CAD object. There are many differential equation solvers, such as the multiresolution time-domain, the finite element method, the pseudo-spectral spatial domain and the transmission line matrix technique, however the most popular technique by far is the finite-difference time-domain (FDTD) technique. One of the most powerful advantages of the FDTD method is that since it is a time-domain technique, a single simulation can be performed to get the results from a wide frequency range. In this technique, the electric field is solved at a given instant of time, then the magnetic field is solved in the next instant of time, and this process is repeated.

Like any other numerical technique, the FDTD method has advantages and disadvantages. The FDTD method discretizes space and time in order to solve Maxwell's equations. Since

$\boldsymbol{E}(\boldsymbol{r},t)$ and $\boldsymbol{H}(\boldsymbol{r},t)$ are calculated everywhere in space (within the computational domain) as they evolve in time, FDTD simulations can be easily translated into visualizations of the EM field through the model. This is very useful for understanding the electrodynamics of complicated structures and provides a tool to verify that the simulation is working properly.

Although the FDTD technique can model physical systems very accurately, the user must be cautious with domain choice and step size ($\Delta\boldsymbol{r}$ and Δt) to ensure realistic results. Also, since the FDTD method is so rigorous, it requires a lot of computational resources to be able to model realistic dimensions. Specifically, for a given computational time frame, results of calculations at all points in the computational domain must be stored in the random access memory (RAM) of a computer, and this imposes a limit on the possible domain size for a given computer. As an example, consider modeling a 50x50 μm^2 core waveguiding structure. If we would like to use the FDTD technique to model the complete structure, a typical domain volume for a 1 mm length waveguide would be 150x150x1000 $\mu m^3 = 2.25x10^7 \mu m^3$. If a step size of $\Delta x = \Delta y = \Delta z = 0.05$ μm is chosen, then there will be $2.25x10^7/(0.05)^3 = 1.8x10^{11}$ “calculation nodes.” If each calculation produces 176 bits of data (or 22 bytes, typical size of the numerical output), this domain would require $3.96x10^{12}$ bytes, or 4 petabytes of RAM. While possible, by current standards, this is completely unrealistic. Not only would the cost of such a system be extremely high, but with current technology, the computational time of such a simulation would be unreasonable.

§2.1.2 FABRICATION TECHNIQUES

The physical realization of these plasmonic systems involves nanofabrication methods. The most heavily utilized technologies for the patterning of nanoscale structures is the use of scanning beam based lithography tools. These include electron beam lithography (EBL), focused ion beam lithography (FIB), and direct laser writing. These methods use particles such as electrons, ions, and photons to scan and write patterns on a substrate as dictated by a CAD object. EBL is the most accurate method, and the most advanced electron beam tools currently can resolve a linewidth below 5 nm.[10] EBL is very time consuming and currently can only be used in small volume prototyping. FIB also has a low throughput, although it is capable of directly patterning materials such as metals instead of having to pattern a resist and using another step such as thermal evaporation to deposit metals into the resist template.

In addition to the direct write techniques described above, there exist other methods to create nanostructures. Nanoimprint lithography (NIL) is a newer fabrication technology which uses a mold (which must be fabricated with another method), and this mold is then pressed onto a thin layer of resist that can be deformed to yield the mold's negative structures. Similar to this technology is template stripping lithography (TSL), which likewise uses a mold as a reusable template for the fabrication of metallic nanostructures. This technique uses a patterned resist mold and the thermal evaporation of metals to create nanostructures with unparalleled smoothness. Dapeng Yu's group at Peking University in China produced several metallic nanostructures with this technique and evaluated the smoothness of the resultant objects using an atomic force microscope.[11] The root mean square (RMS) roughness of the silicon wafer used in the experiment was 0.21 nm and the

EBL patterned poly (methyl methacrylate) (PMMA) was 0.28 nm. After using TSL, the RMS roughness of the deposited metal surface on the PMMA was 0.88 nm, and the RMS roughness of the deposited metal on the Si was 0.55 nm. The smoothness of metals is extremely important in the fabrication of plasmonic nanostructures, as the SPPs traveling at the interface of these structures will diffract off of features on the surface.

§2.2 PLASMONICS PHENOMENA AND APPLICATIONS

Here we will review some applications of plasmonic systems relevant to the work contained in this thesis. Plasmonics is a relatively new field, and it has already generated excitement in many different areas. One of the major promises of plasmonic systems is that they hold the possibility to make a major impact in data communication systems, as the sub-wavelength confinement we have already seen in MIM systems allows for the possibility of smaller interconnects for chip-scale integration. Additionally, solar cell designs have benefited from the inclusion of plasmonic elements, as the increased confinement of light allows for an increase in the probability of exciton creation. Other areas of applications include nanolithography, apertureless near field scanning optical microscopy, nanoscale antennas, and plasmonic systems have even been suggested for photo-thermal cancer therapy.

In addition to applications, it is important to mention that these plasmonic systems allow for the precise control of light-matter interactions on the nanoscale, enabling scientists and engineers to develop systems which push our understanding of how material systems can interact with light. Plasmonic metamaterial systems (engineered materials created from arrays of smaller elements) have been designed that demonstrate extraordinary optical transmission—the transmission of light through apertures which would otherwise prohibit such transmission. These and other metamaterials can be engineered to manipulate lightwaves at an interface such that the metamaterial can exhibit a negative index of refraction, and it has also been demonstrated that plasmonic metamaterials can be used to coax light in such a way to give the observer of the material an illusion of invisibility. This exotic state of matter could theoretically allow for the creation of “invisibility cloaks”—a concept previously only in the domain of science fiction.

§2.2.1 PLASMONIC BIOSENSING

Localized surface plasmons that are tightly bound to a metal-dielectric interface have a high surface energy and are thus highly sensitive to any change in permittivity at the interface. Optical detection of changes in the local refractive index of a dielectric has been achieved by measuring the transmission or reflection spectrum from metallic nanoparticles or periodic arrangements of metallic nanostructures such as 2-dimensional nanoholes or 3-dimensional nanopillars.[12] Figure 7 shows a dark field microscope image of nanoparticles of various shapes and extinction spectra, with similar particles emitting colors at their characteristic radiant frequencies. The spectrum of these nanoparticles can be tuned by varying the geometry and materials. Nanoparticles and arrays of plasmonic nanostructures act as transducers that convert small changes in the local index of refraction into shifts in the extinction spectrum obtained from transmission or reflection spectroscopy. This feature makes systems such as this attractive for biosensing applications because molecular binding events on the plasmonic nanostructures cause an increase in the local refractive index, as most biomolecules have refractive indexes higher than the buffer solution. This optical detection scheme has been especially popular in the biosensor community as a way to detect the binding event between two compatible biological molecules such as antibody-antigen binding, protein-protein binding, and protein-carbohydrate binding.[13, 14] Plasmonic biosensors can be roughly grouped into two main categories: LSP resonance (LSPR) and SPP resonance (SPR) sensors.

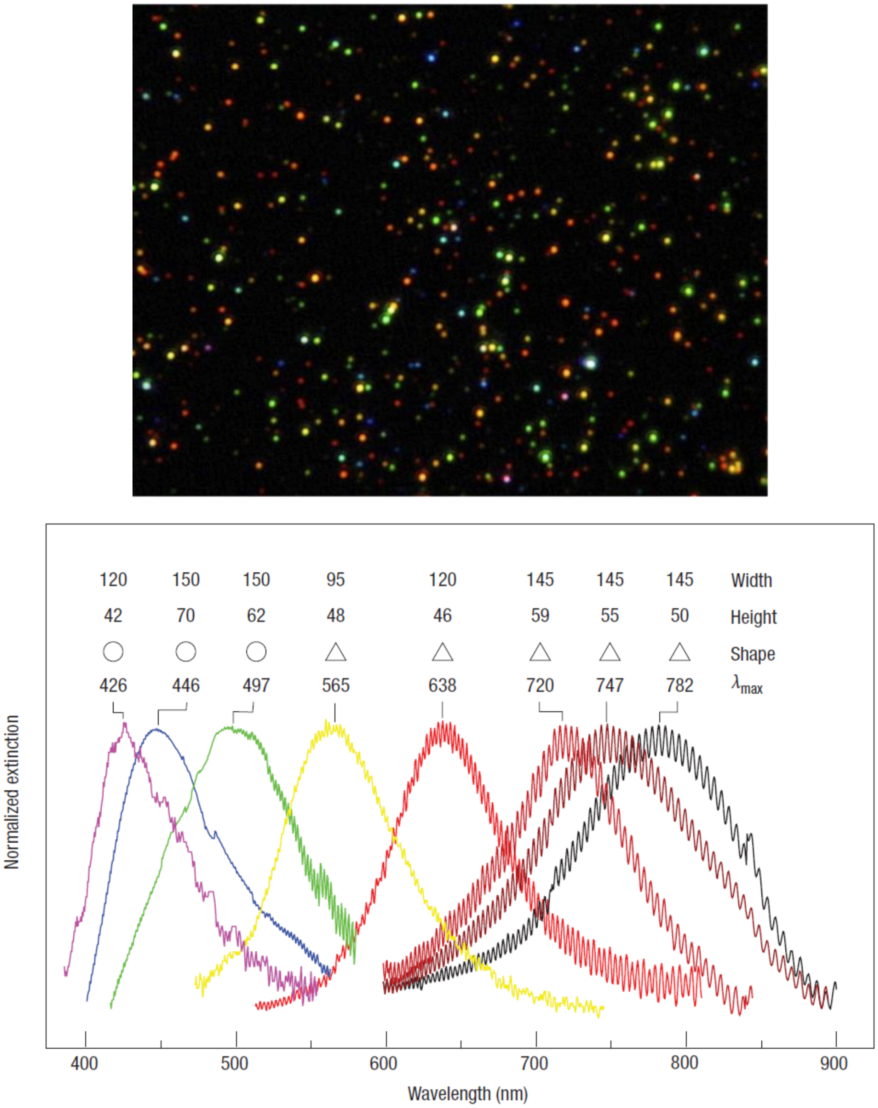

Figure 7: Above: Darkfield image of Au nanorods, spheres and prisms [15]; Below: Extinction spectra of Ag spheres and prisms [16].

SPR sensors were initially favored in the scientific community, as these sensors exhibited large refractive index sensitivities ($\approx 2 \times 10^6$ nm RIU^{-1})[17] whereas LSPR sensors demonstrated sensitivities four orders of magnitude smaller ($\approx 2 \times 10^2$ nm RIU^{-1})[18]. It has been discovered however that LSPR sensors can increase their sensitivity due to their ability to support short and tunable surface plasmon decay lengths.[19] This short decay length enables LSPR sensors to take advantage of extremely confined and concentrated fields that are very sensitive to changes in the local refractive index and enables LSPR sensors to have much smaller sensor areas (~ 2 mm spot size for SPR sensors compared to ~ 20 nm spot size for LSPR sensors). Other advantages of LSPR sensors over SPR sensors are: portability, lower cost, and better small molecule sensitivity.

The performance evaluation of these types of biosensors ushered in a refractometric biosensor figure of merit (FoM) which is now becoming standardized for the characterization of biosensor designs. The FoM for plasmonic biosensors is defined via bulk refractive index sensitivity ($S = \frac{\Delta\lambda}{\Delta n}$) divided by the broadening of the resonant signal (full width half maximum of resonant peak (FWHM)). Thus the FoM is defined as follows:

$$\mathrm{FoM} = \frac{S}{\mathrm{FWHM}}. \tag{23}$$

As the scientific community better understood how LSPR biosensors could be improved, there has been a strong interest in the design of 3D plasmonic nanostructures for the possibility of increasing the mode confinement and intensity enhancement of the electric field within the structure where it can come into contact with the analyte. In recent work completed at the University of Illinois at Urbana-Champaign, Gartia et al. showed that LSPR sensors can possess a FoM much higher than their SPR counterparts. Shown in [20],

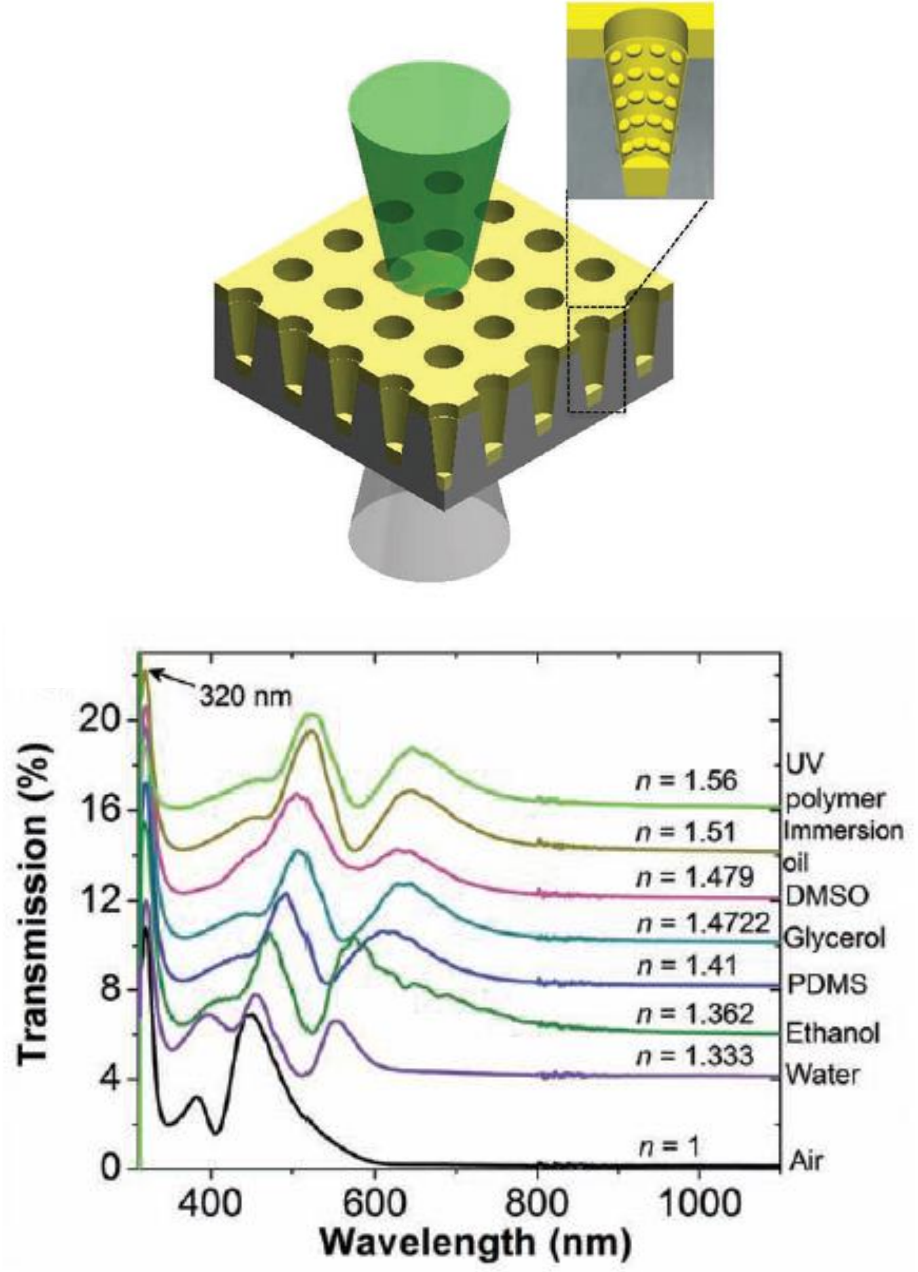

Figure 8: Above: Nano Lycurgus cup array with inset showing sidewalls lined with nanoparticles; Below: Associated transmission spectra for various dielectric refractive indexes.[20]

their design appears similar to the Lycurgus cup, and theoretically boasts an average FoM of ~179 and a maximum of ~1022.[20] Considering SPR sensors typically exhibit a FoM of ~108 (see Appendix §B.1), this particular LSPR design creates possibilities for sensor performance an order of magnitude greater than most SPR sensors.[21] The spectra shown in Figure 8 highlight the redshifting of the spectral peaks with an increase in the index of refraction of the superstrate.

Using modern nanofabrication techniques, most designs are easily fabricated and eliminate the need for additional labeling molecules to detect binding events, which enables fast, real-time identification of biomolecules. The research described above benchmark the design of modern plasmonic biosensors. In chapter 6 of this dissertation, a novel nanostructure is evaluated for its feasibility as a refractometric sensor. This particular design boasts a FoM competitive with some of these benchmark designs, owing its performance to the fact that this particular structure extends into the bulk of the superstrate and possesses design elements which strongly enhance and confine electric fields within the nanostructure.

§2.2.2 PLASMONIC TRAPPING

The gradient of the optical potential energy near a metal-insulator interface can provide an optical trapping force that can be used for the localization and manipulation of subwavelength particles similar to classical optical tweezers. An overview of optical tweezing and the construction of a classical optical tweezer (OT) experimental apparatus using common optics equipment is given in Appendix A. This phenomenon not only enables plasmonic systems to be used for nanometric positional control of nanoscopic objects, but as the object is trapped, this technology also enables the system to be simultaneously used for surface enhanced Raman spectroscopy (SERS).

Traditional microscopic optical trapping experiments work by striking a balance between the scattering force of coherent light incident on a microparticle, and the so-called gradient force on the microparticle—which arises from an intensity gradient around a diffraction-limited focus created by a high numerical aperture microscope objective. Plasmonic optical tweezer (POT) operation is similar to that of traditional optical tweezers in that both take advantage of the gradient in the intensity in a region, however the diffraction limit of the OT limits the size of the object able to be trapped for sufficient periods of time. Plasmonic tweezers offer the possibility for subwavelength confinement, enabling the trapping of submicron objects. Jennifer Dionne's group at Stanford University recently published numerical simulations showing the possibility of trapping particles as small as 2 nm in diameter using a laser power of less than 100mW.[22] The coaxial nanostructure uses the strong field localization in a small cylindrical channel as shown in Figure 9 to create an optical potential well that satisfies the condition for trapping ($U_{well} \geq 10k_BT$), where T is the temperature of the dielectric medium, and k_B is Boltzmann's constant.[23] Using a linearly polarized simulated incident field below the coaxial aperture, Saleh and others in Dionne's group were able to show that the silver coaxial structure would support plasmon modes that could exert a stable trapping force on a 2 nm diameter dielectric sphere with a maximum force of 77 pN/100 mW when the surrounding dielectric is modeled as air. The results of this work show that plasmonic systems can provide trapping solutions for subwavelength particles.

Plasmonic trapping has been achieved experimentally as well. Grigorenko et al. has demonstrated the stable trapping of 200 nm polystyrene spheres using plasmonic “nanodot” pairs. These pairs of tapered pillars were fabricated using electron beam lithography on a glass substrate and demonstrated stable trapping as recorded by a quadrant photodiode nanometric position detecting system. While not as impressive as the possibility of trapping 2 nm diameter objects, the 200 nm spheres were still beyond the diffraction limit of the incident light in this experiment (1,064 nm neodymium-doped YVO_4 diode pumped solid-state laser). Their results can be seen in Figure 10, which shows the trapped sphere position over time. The slight variations in position are due to the Brownian motion of the polystyrene sphere.

It has also been demonstrated that stable plasmonic trapping can be achieved without the need for nanostructured substrates. Changjun Min et al realized they could overcome some of the difficulty in exciting surface plasmons on a smooth surface by modifying the polarization of the incident beam. Using a vortex phase plate with circularly polarized light, they were able to create a radially polarized beam that was incident on a gold thin film (see Figure 11 for experimental setup). This configuration allowed for the momentum carrying electric field vector to be oriented radially about the beam cross-section, forcing the surface charges toward the center of the beam’s focus. The resultant polaritonic excitation looks similar to a Bessel beam, and the research presented in their work experimentally confirmed that this field was capable of trapping and manipulating metallic nanoparticles.[24]

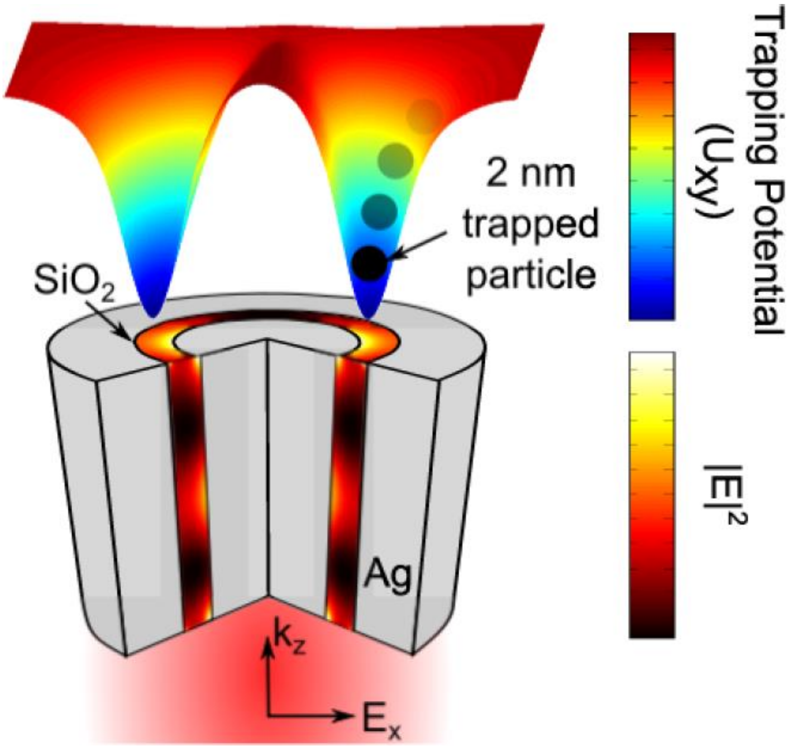

Figure 9: Coaxial plasmonic aperture and associated transverse trapping potential.[22]

Results presented in chapter 6 provide numerical evidence that the addition of a metallic substrate can improve the performance of plasmonic nanotrapping systems. The design presented in the next chapter displays performance enhancements as compared to the coaxial design used in reference [22], made possible by utilizing the reflected plasmonic field from the inclusion of a reflective, planar metallic substrate.

In this chapter we have explored the state-of-the-art research in plasmonic biosensing and plasmonic trapping. We will find that plasmonic nanostructures can be created that perform both of these functions. The remainder of this thesis will discuss the design and evaluation of such a nanostruture as a tool for biosensing and trapping experiments.

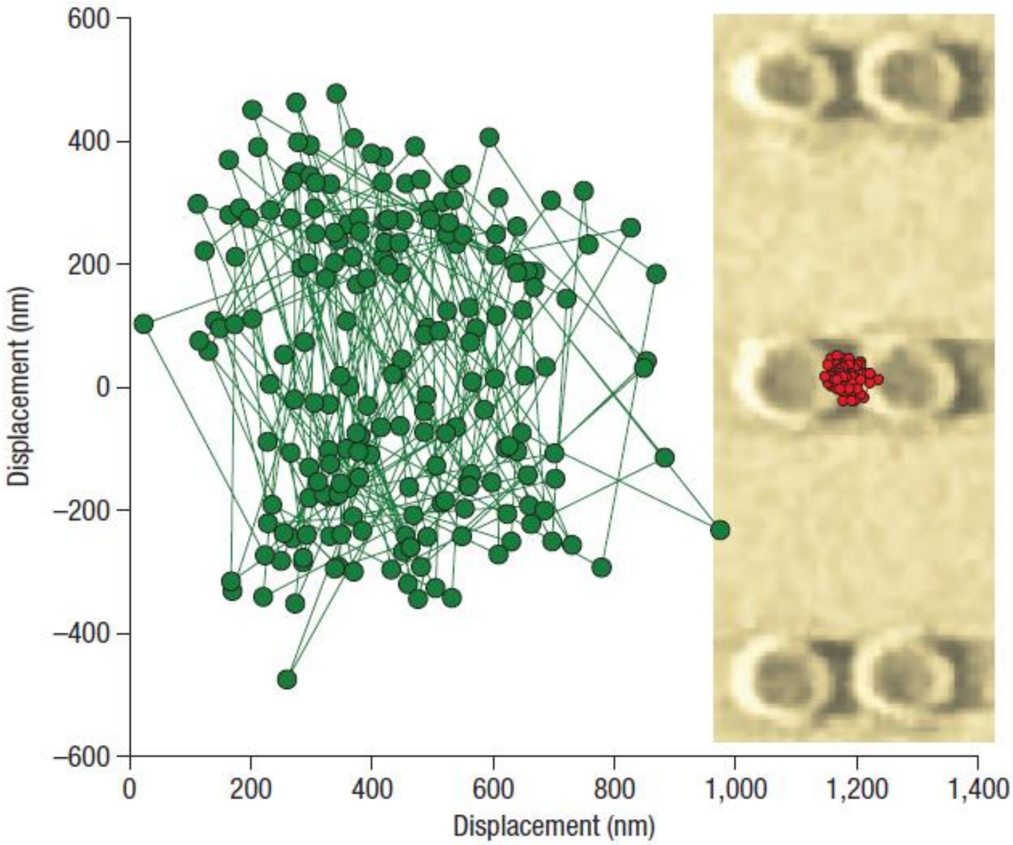

Figure 10: Trapped bead position as a function of time (green circles are bead positions at 5 ms intervals). Inset shows nanodot pairs with red circles also indicating trapped bead position over time.[25]

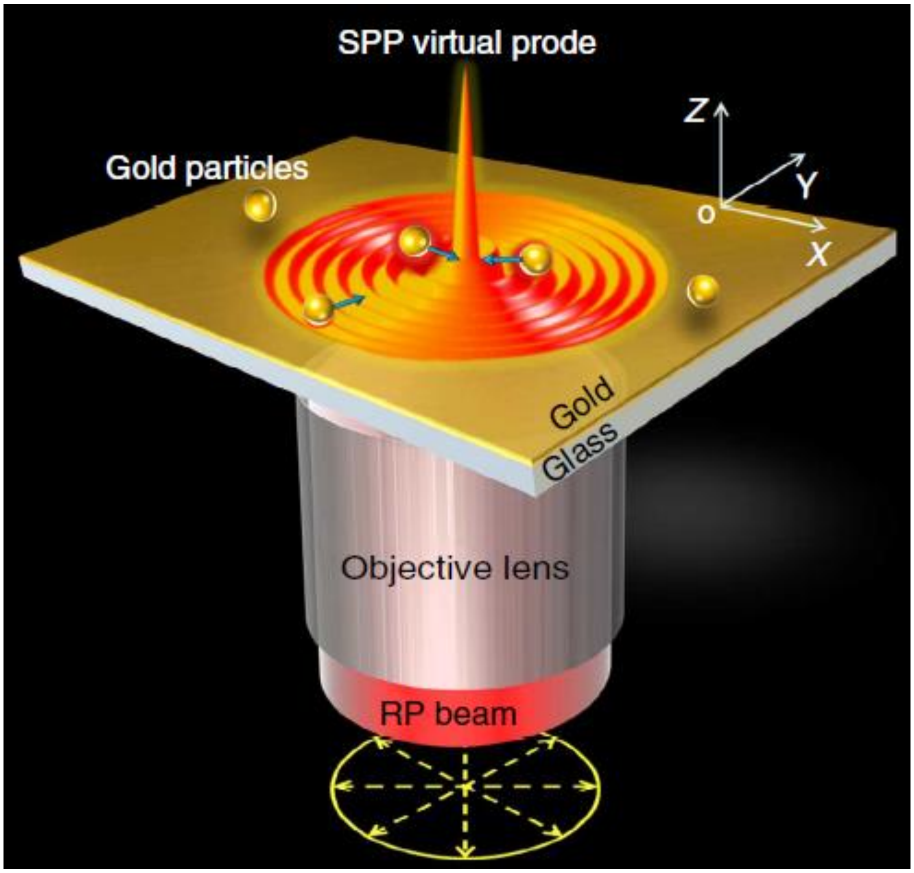

Figure 11: Plasmonic tweezers without nanostructured substrate.[24]

CHAPTER 3: CNP NANOSTRUCTURE PLASMONICS

§3.1 DESIGN

By controlling the geometry of a metallic nanostructure, resonances and field enhancements can be engineered for specific applications. Many shapes and structures have been investigated including nanospheres [26, 27], nanorods [28-30], nanocubes [31], nanopillars [32, 33], nanorice [34], bullseyes [35], nanoshells [36], bowties [37], dolmen structures [38], split-ring resonators [39], ring-disk structures [40-44], pyramids [45], mushrooms [46], and many more. Design of these nanostructures is typically approached phenomenologically, adding features to nanostructure designs based on previously observed attributes. For instance, as we understand that coulombic repulsion causes surface electrons to huddle around sharp edges, we can use this insight to engineer regions in a nanostructure which should support confined, enhanced electric fields. Once a general design is decided upon, then numerical optimization routines can be implemented to find the optimal values for the geometrical and material parameters.

Another resource in the plasmonicist’s toolbox for designing plasmonic nanostructures is the plasmon hybridization (PH) method developed by Emin Prodan in 2003.[47] The PH method is a predictive model used to theoretically analyze the surface charge distribution in complex plasmonic nanostructures by considering the hybridization of plasmons on primitive geometries such as disks and cavities.

Using phenomenological guidance along with PH diagrams, a versatile nanostructure has been designed that will be shown later in this thesis to perform as both a biosensor and a platform for plasmonic trapping. The ability of surface plasmons to be spatially confined well beyond the excitation wavelength diffraction limit enables the plasmonic designer to be free to create gratings, grooves, or channels that have dimensions that can be just several nanometers in extent. The nanostructure evaluated in this dissertation is a coaxial nanopillar (CNP) that stands upon a metallic substrate as shown in Figure 12. This pillar uses a cylindrical channel to confine electromagnetic fields of both plasmon and polariton nature, and the resulting confinement yields significant field enhancement and exotic resonances whose fields extend into the surrounding medium, which makes this arrangement ideal for refractometric sensing. The spatial distribution of the plasmons also enables this design to be a strong candidate for nanometric plasmonic trapping experiments, as it has already been shown that similar coaxial plasmonic nanostructures support optical potential wells enabling stable trapping events.[22]

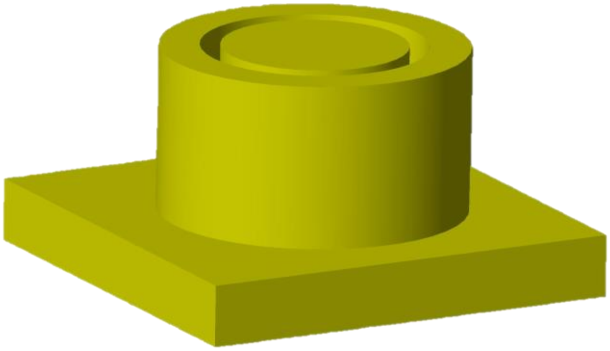

Figure 12: CNP geometry.

§3.1.1 CNP PLASMON HYBRIDIZATION TREE

Since this structure extends out of the plane of the substrate, the dipole charge distribution induced in the nanostructure by an excitation beam cannot fully be described using the PH method. The PH method is an electrostatic analysis method that does not take retardation effects into account. The CNP is a quasi-3D nanostructure, and can be viewed as a ring-disk structure extending into the third dimension. As mentioned earlier in this chapter, ring-disk structures have been the topic of considerable research, and plasmon hybridization diagrams have been worked out for the ring-disk structure.[48] Using the hybridization technique adopted from molecular orbital theory, the PH diagram for the ring-disk structure is complicated as seen in figure 2 of the previous referenced article, and more complex structures can have even more complicated diagrams. Because of this, we developed a new representation for the plasmon hybridization seen in Figure 13 which is simpler and more intuitive. We call this diagram a plasmon hybridization tree (PHT). In the PHT for the ring-disk structure, we show the direction of the electric field from the incident EM wave responsible for the simple dipole excitation of the charges on the geometric structures. To build a complex nanostructure, we start with two primitive geometries seen in region (a) of Figure 13: a disk and a cavity and their associated charge distributions. Using dashed lines, we can then display their two hybridized structures, a high energy (anti-bonding) antisymmetric charge distribution and a low energy (bonding) symmetric charge distribution shown in region (b). Lastly region (c) in Figure 13 shows the final possible hybridized plasmon states resulting from the plasmon coupling between the various primitive and previous hybridized structures in the PHT.

In the PHT there exist brackets that contain objects which can hybridize. These brackets allow for an energy comparison of the enclosed structures without the need to create complicated PH diagrams that work with a single energy axis. The PHT method also provides the plasmonicist with a new design tool, as this method is superior to the previous PH method in that it allows one to "build" a plasmonic nanostructure with desired properties based on the electronic response of the constitutive elements.

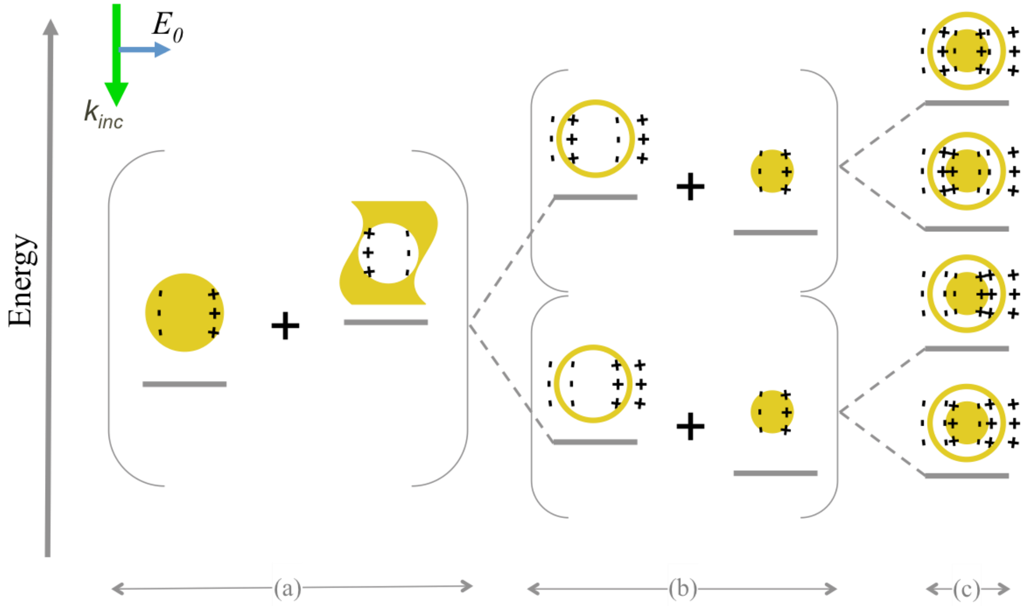

Figure 13: Plasmon hybridization tree for CNP ring-disk structure.

§3.1.2 TM MODES IN AN INFINITE COAXIAL CABLE

We now turn our attention to finding analytic expressions for the electric and magnetic fields supported in an infinite coaxial cable geometry in the electrostatic limit. Since plasmonic fields are always TM, we can start with the Helmholtz equation (Equation (11)) in its cylindrical form in one dimension for a TM wave (z, the direction along the longitudinal axis):

$$\frac{1}{\rho}\frac{\partial}{\partial\rho}\left(\rho\frac{\partial E}{\partial\rho}\right)+\frac{1}{\rho^2}\frac{\partial^2 E}{\partial\phi^2}+\frac{\partial^2 E}{\partial z^2}+k_c^2 E=0. \tag{24}$$

As TM waves always have a cutoff frequency (corresponding to the surface plasmon frequency), we can use the definition of the cutoff wavevector in our analysis, $k_c^2=k_0^2+\beta^2$, where again β represents the longitudinal propagation wavevector.

Since E can be represented as the product of the radial, azimuthal, and longitudinal functions, $E(\rho,\phi,z)=R(\rho)\Phi(\phi)Z(z)$, we can use the method of separation of variables to solve Equation (24). After substitution of $E(\rho,\phi,z)$ and subsequent identification of constant quantities, the Helmholtz equation takes the form of Bessel's equation:

$$\rho\frac{d}{d\rho}\left(\rho\frac{dR}{d\rho}\right)+[(k_c\rho)^2-\Lambda^2]R=0 \tag{25}$$

where $-\Lambda^2=\frac{1}{\Phi}\frac{\partial^2\Phi}{\partial\phi^2}$ is a constant, as it is independent of ρ and z. The standing wave portion of the E-field in the coaxial line $E_0(\rho,\phi)=R(\rho)\Phi(\phi)$ can thus be obtained:

$$E_0(\rho,\phi)=[A\sin\Lambda\phi+B\cos\Lambda\phi][CJ_n(k_c\rho)+DY_n(k_c\rho)]. \tag{26}$$

With the inclusion of the harmonic spatial dependence, this can be extended to include the longitudinal part:

$$E_z(\rho,\phi,z)=E_0(\rho,\phi)e^{-i\beta z}. \tag{27}$$

Applying the boundary conditions $E_{\phi}(r_1, \phi, z) = 0, E_{\phi}(r_3, \phi, z) = 0, E_z(r_1, \phi, z) = 0, E_z(r_3, \phi, z) = 0$ to E_z, we can eliminate the coefficients C and D by setting the determinant to zero and arrive at an eigenvalue equation for the cutoff wavevector:

$$J_n(k_c r_1) + Y_n(k_c r_2) = J_n(k_c r_2) + Y_n(k_c r_1). \tag{28}$$

The full expression for the longitudinal E-field cannot be solved for analytically, and has the form:

$$E_z(\rho, \phi, z) = [A \sin \Lambda\phi + B \cos \Lambda\phi][Y_n(k_c r_1) J_n(k_c \rho) - J_n(k_c r_1) Y_n(k_c \rho)] e^{-i\beta z}. \tag{29}$$

Substitution of this function into Maxwell's equations yields the remaining transverse fields of the TM wave:

$$\begin{aligned} E_{\rho}(\rho, \phi, z) &= -\frac{i\beta}{k_c^2}\frac{\partial E_z}{\partial \rho} \\ &= -\frac{i\beta}{k_c}[A \sin \Lambda\phi + B \cos \Lambda\phi][Y_n(k_c r_1) J'_n(k_c \rho) - J_n(k_c r_1) Y'_n(k_c \rho)] e^{-i\beta z} \end{aligned} \tag{30}$$

$$\begin{aligned} H_{\phi}(\rho, \phi, z) &= \frac{i\omega\varepsilon}{k_c^2}\frac{\partial E_z}{\partial \rho} \\ &= -\frac{i\omega\varepsilon}{k_c}[A \sin \Lambda\phi + B \cos \Lambda\phi]\big[Y_n(k_c r_1) J'_n(k_c \rho) - J_n(k_c r_1) Y'_n(k_c \rho)\big] e^{-i\beta z}. \end{aligned} \tag{31}$$

§3.2 NUMERICAL ANALYSIS

The analytical results presented in the previous section describe the response of an infinite coaxial cable. The CNP as pictured in Figure 12 shows a finite structure that exhibits similarities to the infinite coaxial cable, but ultimately cannot be described exactly using analytical methods within the current framework. The CNP nanostructure has a reflective surface beneath and a truncated upper surface which is exposed to the dielectric environment. The infinite coaxial cable allows all frequencies, while the finite CNP cavity only allows certain discrete frequencies and phase changes. It will be shown in this section that reflections of the EM modes within the channel of the CNP yields cylindrical EM standing wave modes. These geometrically-induced or "spoof" plasmons are identical in nature to the surface plasmons first discussed in Chapter 1, yet are established in a slightly different way. In fact, almost any disturbance of a flat metallic surface produces a SPP-like bound surface state.[49]

This section investigates the response of the CNP and its primitive structures under various polarization states of the excitation beam using FDTD numerical simulations via the commercial software Lumerical FDTD Solutions. Geometrical parameters are varied and sweeps of these parameter spaces reveal optimal geometric configurations for the CNP.

§3.2.1 NEAR FIELD ANALYSIS OF THE CNP

The permittivity of gold cannot be accurately represented by the Drude (plasma) model, as lattice potential and electron-electron interactions are neglected using this approach. To overcome this limitation, Lumerical's software implements a multi-coefficient model (MCM) which utilizes a more extensive set of basis functions to better fit the dispersion profiles of the materials. In the simulations presented in this work, gold is modeled using the MCM method, and for the CNP structure in this study, seven coefficients were used in all simulations to best fit gold's experimental complex permittivity from material data obtained from Johnson and Christy.[50] All simulations also used twelve perfectly matched layers (PML) around the simulation, and all simulations performed are fully three-dimensional. Lastly, the excitation beam used in all simulations presented herein was a total-field scattered-field (TFSF) source which separates the simulation region into two different regions. The simulation region containing the CNP was the total field part of the TFSF source and the region outside this bounding box computed the scattered field only. The dimensions of the FDTD simulation region was set to be at least $0.5\lambda_{\mathrm{inc}}$ between metal surfaces and the PML boundaries to ensure that local evanescent fields decay before reaching the boundary. The extinction spectrum data used throughout this dissertation was obtained by integrating the power loss ($\propto \mathrm{Im}\{\varepsilon_{\mathrm{metal}}\}$) over the boundaries of an analysis region set around the CNP. This produces the average absorption of energy (divergence of the Poynting vector) by the metallic nanostructure due to the wavepacket of incident light.

§3.2.2 VERIFICATION OF NUMERICAL RESULTS

To verify the validity of the numerical results in this dissertation, we compare results obtained using the approach employed in the studies herein to a previously published study of a similar system. Hao et al. has evaluated a quasi-2D version of the CNP in their ACS Nano article from 2009 and has used a similar FDTD approach to evaluate the extinction in their nanostructure.[41] Figure 14 compares results they obtained in their study for a shorter (h = 50 nm) version of the CNP on a silica substrate to results obtained in an identical system using our approach. Their approach employed a plane wave excitation to excite the plasmonic modes in their gold nanostructure whose permittivity was modeled using a 4-term Lorentzian fit to the Johnson and Christy data. We instead use the Lumerical recommended TFSF source, as it better handles scattering events which are important in the CNP whose permittivity is modeled as a 10-term MCM fit to the Johnson and Christy data. The silica substrate appears to be modeled as a linear dielectric in Hao's study, where the permittivity is set at 2.25 F/m, with a corresponding index of refraction, *n* = 1.5. Our study used a MCM fit to the results of Palik's study on the permittivity of water.[51] The slight differences in the features of the broad anti-bonding resonance is thought to be due to the differences in the way the materials were modeled. For slight differences in the refractive index difference between substrate and superstrate, Fresnel's equations predicts different reflectivities, and this particularly affects the higher frequency resonance (dipolar anti-bonding resonance or DAR) due to the coupling of the reflected plasmons as discussed in more detail in the next chapter. In addition, this difference in refractive index also gives rise to the slight redshift between results ($\lambda_{\text{DAR,ours}} - \lambda_{\text{DAR,theirs}} \approx 24$ nm). Lastly, the way absorption is calculated may be different as well between the studies. Overall, the extinction profiles match well between the two studies.

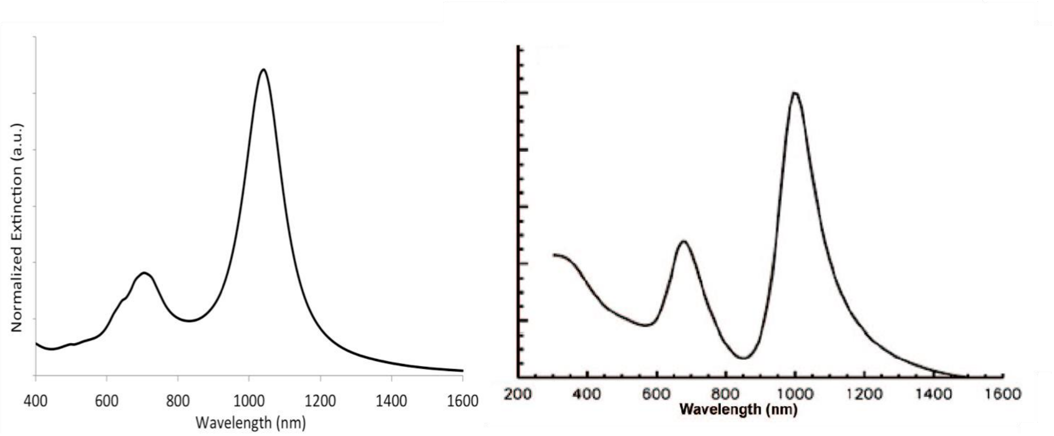

Figure 14: Verification of numerical results based on comparison with previously published data in a similar system.

§3.2.3 ERROR ANALYSIS

In simulating the plasmonic response of metallic nanostructures using FDTD, one must be concerned with several factors including the proximity of the PML layers, the number of PML layers, the material modeling technique, the calculation mesh size, the time step, and the interpolation of monitor data. Certain good practices in setting up simulations in the Lumerical FDTD environment help avoid many of the errors associated with several factors above such as number of PML layers and the proximity to the PML layers as mentioned in §3.2.1, and the proper use of excitation sources and physics monitors. To ensure accurate modeling of the simulated materials using the MCM method as described in the previous section, enough coefficients must be used to reproduce the experimental permittivity results. With the PML layers, excitation sources, physics monitors and materials set up carefully, the accuracy of the simulation is largely dependent on the appropriate choice of time step (Δt) and the spatial mesh step (Δx, Δy, Δz). The time step is set by the Courant-Friedrichs-Lewy (CFL) stability requirement, $\Delta t = \Delta x / \sqrt{2}c$, where c is the speed of light. The smallest spatial mesh used in the simulations in this thesis is Δx = 2.20 nm, corresponding to a required time step of ~ 5.19 attoseconds, which is larger than the time step used for all simulations, ~ 4.13 attoseconds. With the time step set appropriately, the remaining factor to ensure physically accurate simulations is the spatial mesh resolution. Each simulation requires a different minimal mesh size, dictated by the size of the simulated structures and the spatial extent of the resulting fields on the metallic nanostructures. To determine an appropriate spatial mesh, a series of simulations is performed for each unique simulation. Simulations are performed at increasingly smaller mesh sizes until the results of a simulation converge to the same trend. In the following example, a convergence simulation is shown that corresponds to the smallest nanostructure feature size (5 nm gap) in this dissertation. Results from this simulation provide an upper bound to the possible error in the simulated results presented in this thesis. From Figure 15 we can see that the simulations converge to a common result near a mesh size of 2.30 nm. Results above 2.50 nm do not represent physical solutions, as there is only one mesh cell (Yee cell) within the 5 nm gap.

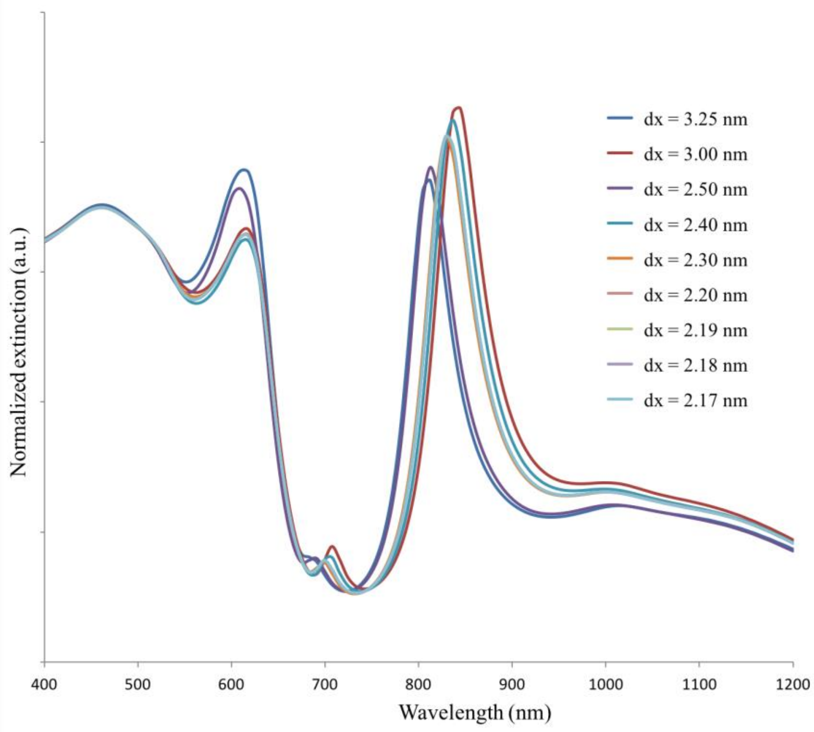

Figure 15: Convergence study for spatial mesh on CNP with 5 nm gap.

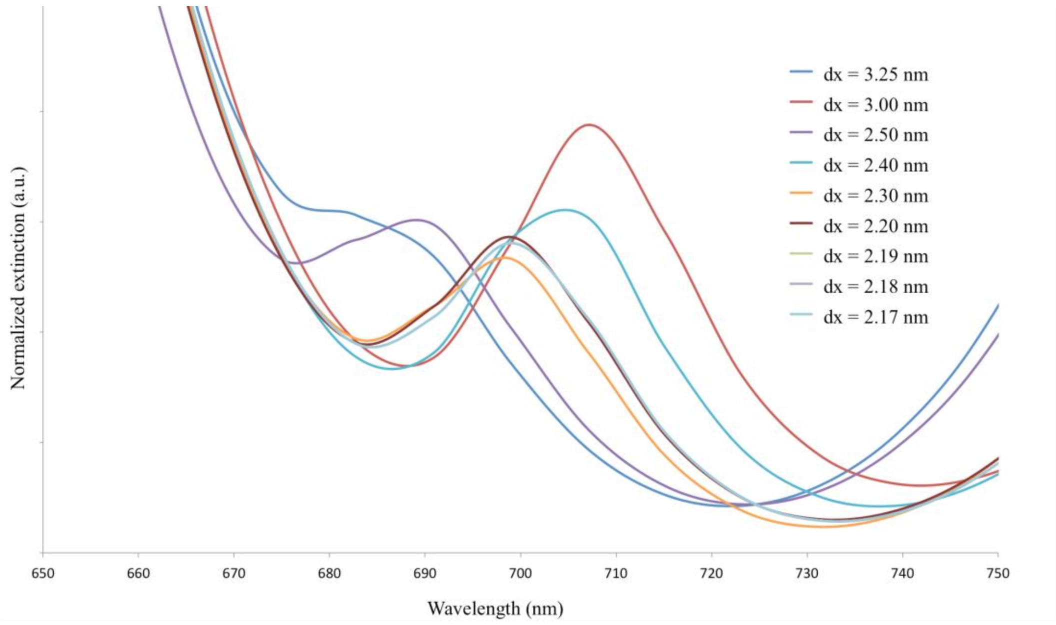

Figure 16: A closer view of the peak near 699 nm from the previous figure.

The simulations of the mesh sizes 2.17 – 2.19 nm yielded identical results. The Δx = 2.20 nm simulation is compared to the Δx = 2.19 nm using the following equation:

$$Error\ \% = 100 \times \left|\frac{\sigma_{2.20} - \sigma_{2.19}}{\sigma_{2.20}}\right|. \tag{32}$$

Here, σ represents the normalized extinction value at a particular wavelength. The average error % between the two cases was 0.414 %. This small error is only present in the results from the simulations of the CNP with the 5 nm gap. All other simulations contained in this thesis have results which converge to an exact value.

§3.2.4 GEOMETRIC PARAMETERS FOR RESONANCE OPTIMIZATION

When designing plasmonic nanostructures, one is primarily concerned with resonance engineering. To find the optimal geometry of a gold nanopillar on a gold substrate as shown in Figure 17, we can utilize numerical routines that optimize the geometry by examining the EM extinction in the nanostructure for various parameter values. Sweeping over the radial and longitudinal parameter spaces, the color plots were generated in figures 16-19 below using a perpendicularly oriented TFSF source in the range of frequencies corresponding to wavelengths between 400-1000 nm, whose orientation is depicted in Figure 17.

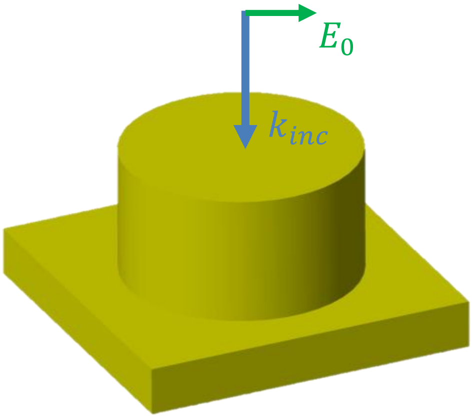

Figure 17: Gold pillar on gold substrate showing a perpendicularly incident excitation beam.

High frequency excitation of the nanopillar yields resonances over a broad range of heights for both of the fixed radii in Figure 18 and Figure 19, and to a similar extent for both of the fixed height radius sweeps in Figure 20 and Figure 21. From these plots and for ease of fabrication, a height of 130 nm and a radius of 140 nm was chosen for our nanopillar.

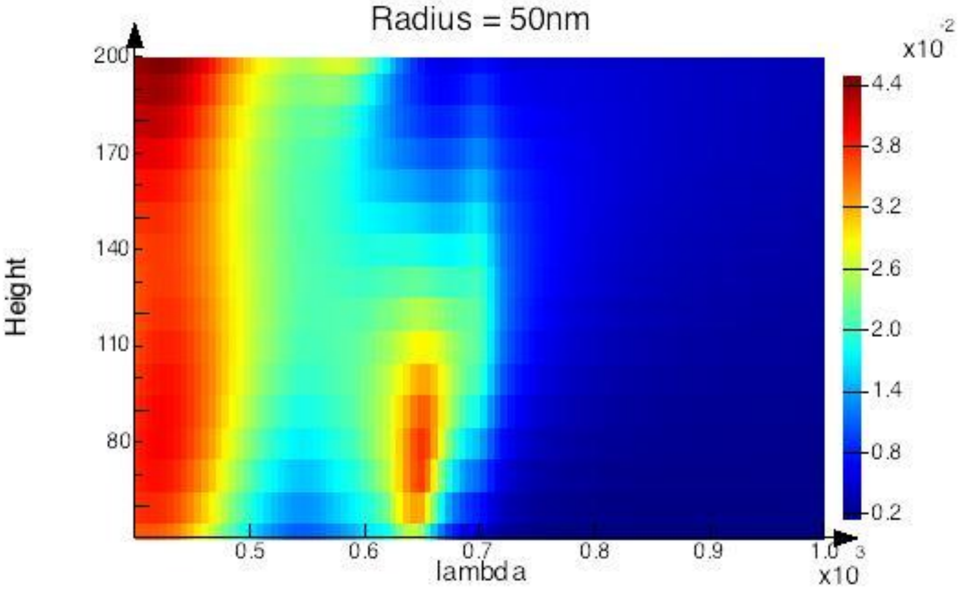

Figure 18: Nanopillar height sweep at fixed radius of 50 nm.

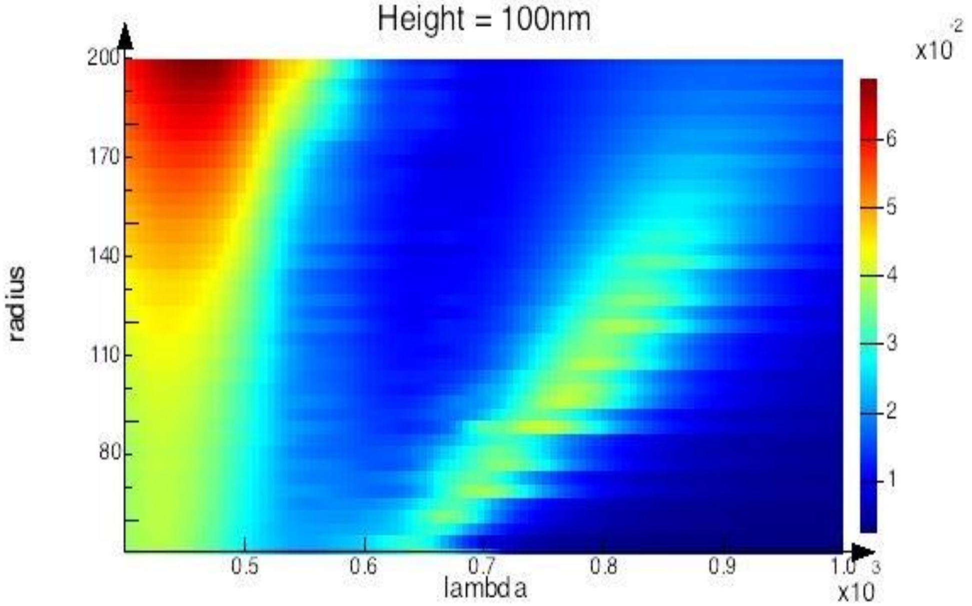

Figure 19: Nanopillar height sweep at fixed radius of 100 nm.

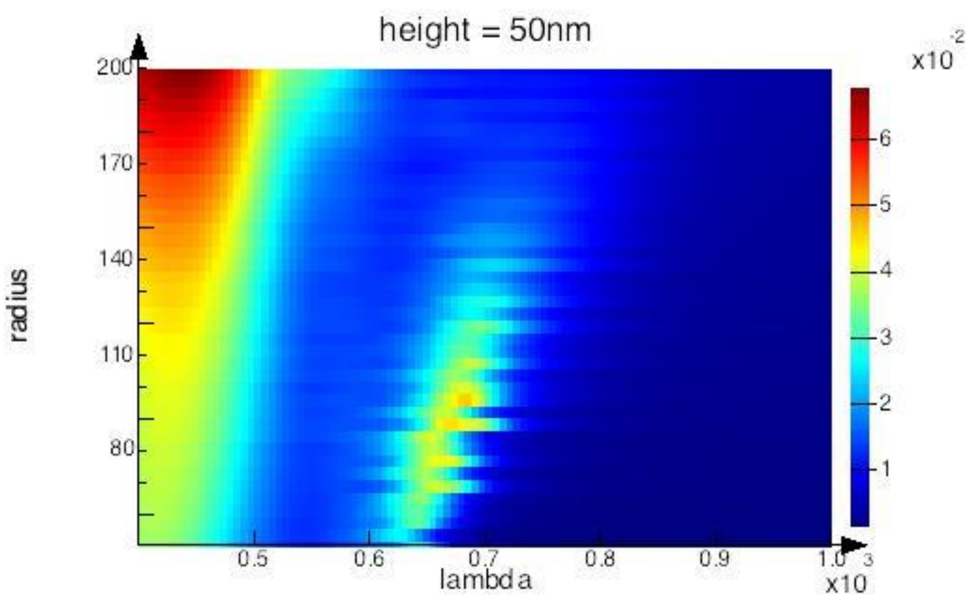

Figure 20: Nanopillar radius sweep at fixed radius of 50 nm.

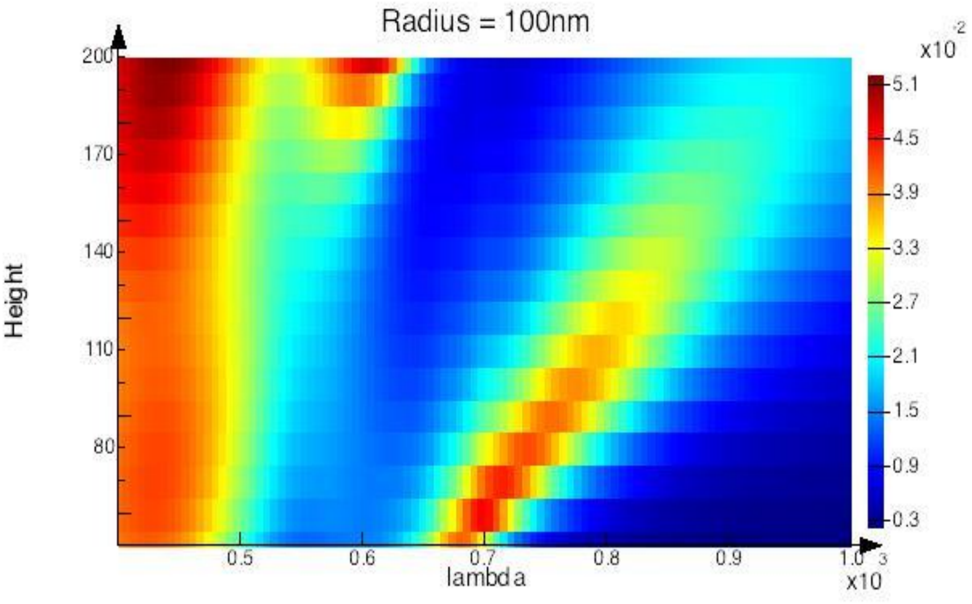

Figure 21: Nanopillar radius sweep at fixed radius of 100 nm.

The shape of the near-IR resonance in the color plots shows some interesting physics of this system. The 50 nm fixed radius and height cases show a similar spectral position of this peak while varying the other spatial parameter, while the 100 nm fixed radius and height show a peak that is redshifted when the other spatial parameter is varied. This indicates that the smaller fixed geometry cases are less affected by varying the other spatial parameter and thus the resonances must be more a result of the intraband transitions in gold. The larger fixed geometry cases indicate that the spoof plasmons play a larger role. The redshifting of the plasmon resonance in the nanopillar is most likely due to an increased amount of coupling with the surface plasmons with a time-retarded field arising from reflections from the gold substrate. In fact, retardation-related frequency shifts are always red, as plasmon resonances induce quasistatic currents within the conductor which in turn generate magnetic fields that subsequently generate secondary electric fields which contribute to the Poisson equation, causing redshifts in the electrostatic eigenvalues of this equation.[52]

§3.2.5 CYLINDRICAL CHANNEL

Here we will discuss the inclusion of a cylindrical channel into our nanopillar to create the coaxial structure as was depicted previously in Figure 12. The addition of a cylindrical channel on the top of the nanopillar introduces interesting changes in the response of the system to an excitation beam. Firstly, the channel needs to be deep enough to contain plasmonic modes. Secondly, the channel position is important as geometric inclusions such as gaps typically increase plasmonic resonance when they are placed at regions where resonance was at a maximum without the inclusion. Figure 22 shows the extinction spectra of various gap positions for a cylindrical channel gap with a depth of 50 nm and a width ($g = r_2 - r_1$) of 20 nm. The extinction of the EM excitation is at a maximum nearest the perimeter of the pillar as expected. The lower energy broad peak, or bright mode, is due to the bare pillar structure, and the narrower peak is observed due to the inclusion of the cylindrical channel gap. The narrow, or dark mode, peak is redshifted with increasing radius, indicating that the time-retarded field couples more strongly with the gap plasmons as the average channel radius is increased.

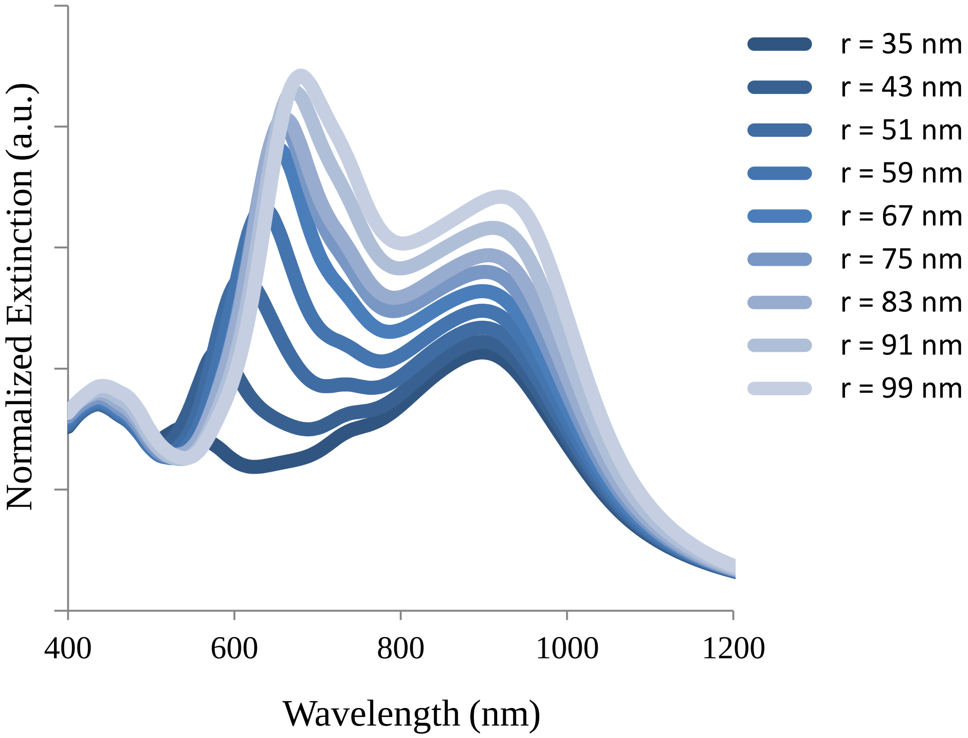

Figure 22: Extinction spectra for various average channel radii ($r_{avg} = (r_2 - r_1)/2$) for CNP with g = 20 nm.

Lastly, the width of the gap affects the total modal volume available for gap plasmons and should also be optimized. Figure 23 shows the extinction spectra for various gap widths, each placed at an average radius $r_{avg} = (r_2 - r_1)/2 = 50\ \text{nm}$, illustrating a strong redshifting of the dark mode with increasing amplitude for decreasing gap widths. This is due to the fact that the smallest gap sizes act as a diffractive element and the larger gap sizes contain more of the field modal volume.

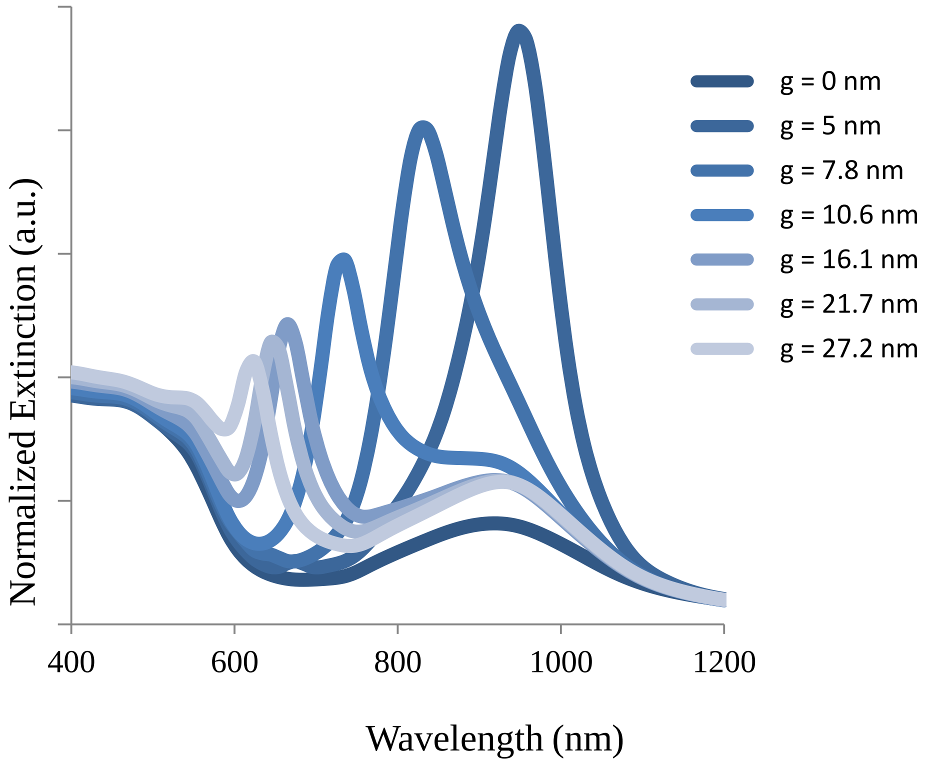

Figure 23: Extinction spectra for various channel widths for CNP with $r_{avg} = (r_2 - r_1)/2 = 50\ \text{nm}$.

§3.2.6 EFFECT OF SUBSTRATE

We will begin our analysis by considering a bare nanopillar on a glass substrate with a linearly polarized excitation beam directed perpendicular to the upper surface of the nanopillar as shown in Figure 24. Many plasmonic nanostructures are investigated by other researchers on glass substrates for use in transmission studies. While imaging of the system is more difficult, the inclusion of a reflecting substrate has several advantages over the use of a glass substrate.

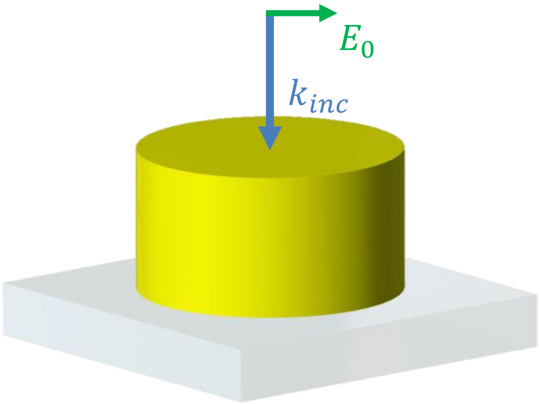

Figure 24: Gold pillar on glass substrate showing a perpendicularly incident excitation beam.

Firstly, the use of a dielectric substrate such as glass allows for the plasmons to bleed into the substrate, away from the structure where the fields are needed. Kai Wang and Kenneth Crozier from Harvard University have already investigated the effect of the substrate in a similar gold nanopillar system.[33] Their study investigated the electric field profile around the nanopillar with and without a reflective substrate, and the thermal impact of using a metallic substrate.

Figure 25 shows the effect of a dielectric substrate on the electric field distribution around the nanopillar. Here we can see that the field that would otherwise surround the metallic nanostructure has bled into the substrate, deleteriously affecting the performance of the structure for whichever application it is intended for.

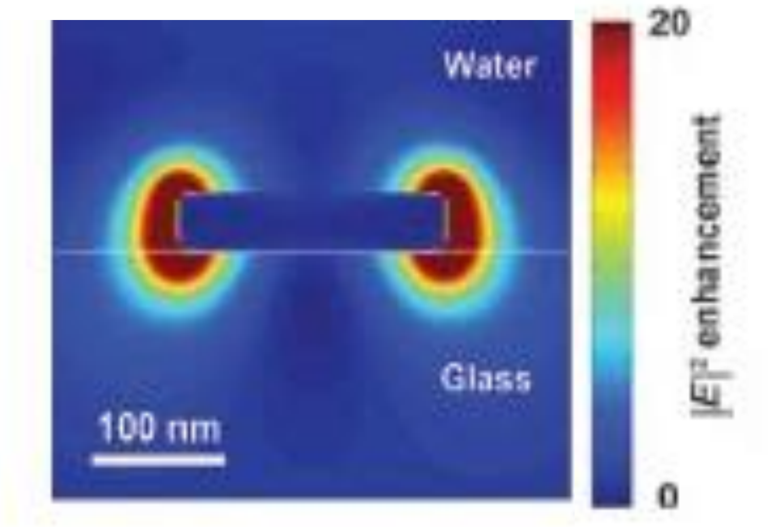

Figure 25: Effect of dielectric substrate on E-field distribution.[33]

The second advantage of a reflective substrate is that the reflected (time-retarded) field can subsequently couple with plasmons on the upper surface of the pillar, increasing the enhancement there. We will see in the next chapter that this retarded field can couple to other fields within the cylindrical channel of the CNP to induce highly sensitive resonances. Lastly, in addition to providing the reflected field, the inclusion of a metallic substrate also acts as a heatsink which can mitigate the thermal response of the superstrate to the inherent power associated with the enhanced electric field on the surface of the nanostructure. Figure 26 shows results from a Comsol Multiphysics simulation performed by Wang and Crozier.

In this study it was determined that the use of a substrate with a higher thermal conductivity such as diamond creates the same temperature increase of the superstrate (water) as glass, but only when the incident intensity of the linearly polarized light was 250-fold.

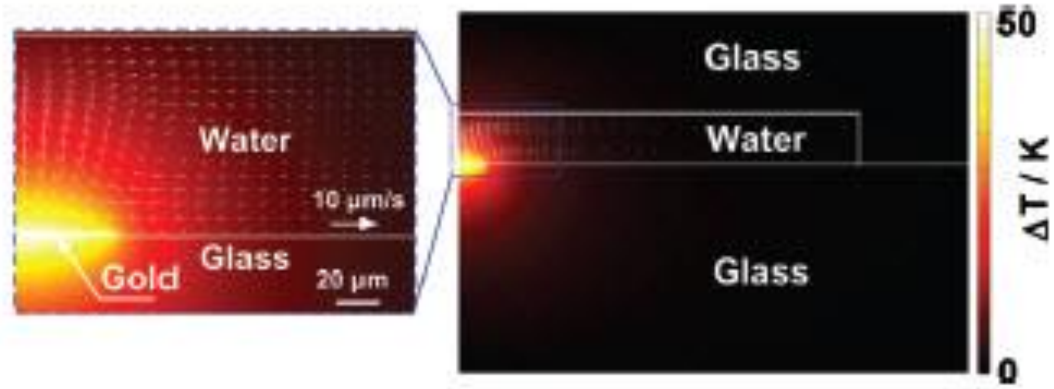

Figure 26: Thermal response of superstrate due to a $10\ \mu W/\mu m^2$ excitation.[33]

In addition to the advantages described above, it has also been shown that the substrate can induce additional resonances in plasmonic systems.[31] Results of this study indicate that the presence of a substrate can induce quadrupolar resonances in a nanostructure from the "image" of a dipolar resonance in the substrate.

In addition to the effects of substrate and channel on the response of the CNP, the angle and the polarization of the incident excitation beam affects the electrodynamics of the system. The next section describes how the polarization of normally incident light affects the response of the CNP.

EXTINCTION IN VARIOUS GEOMETRIC CONFIGURATIONS

To determine the impact of the various geometrical elements on the CNP's response to illumination, we now look at a comparison of the EM extinction in several different primitive structures which compose the CNP. Figure 27 shows that the extinction resulting from the normal illumination of a bare pillar with no substrate (blue plot) in water with $h = 130$ nm and $r_3 = 140$ nm is relatively flat in the near-IR. The inclusion of a reflecting substrate to the bare pillar (orange plot) produces a broad superradiant peak near 958 nm due to the reflected field interacting with the pillar plasmons. Upon addition of a channel with $g = 10$ nm (grey plot), we see a pronounced narrow peak emerge at 901 nm and a shoulder around 642 nm. Lastly, the full CNP on a reflective substrate is shown to possess the features present in the other spectra, but now reveals a new peak centered near 836 nm on the blue side of the narrow peak which arose from the addition of the channel to the system. As this peak only appears when all the elements are present, it must be due to the interaction of the channel plasmons with the field reflected from the substrate.

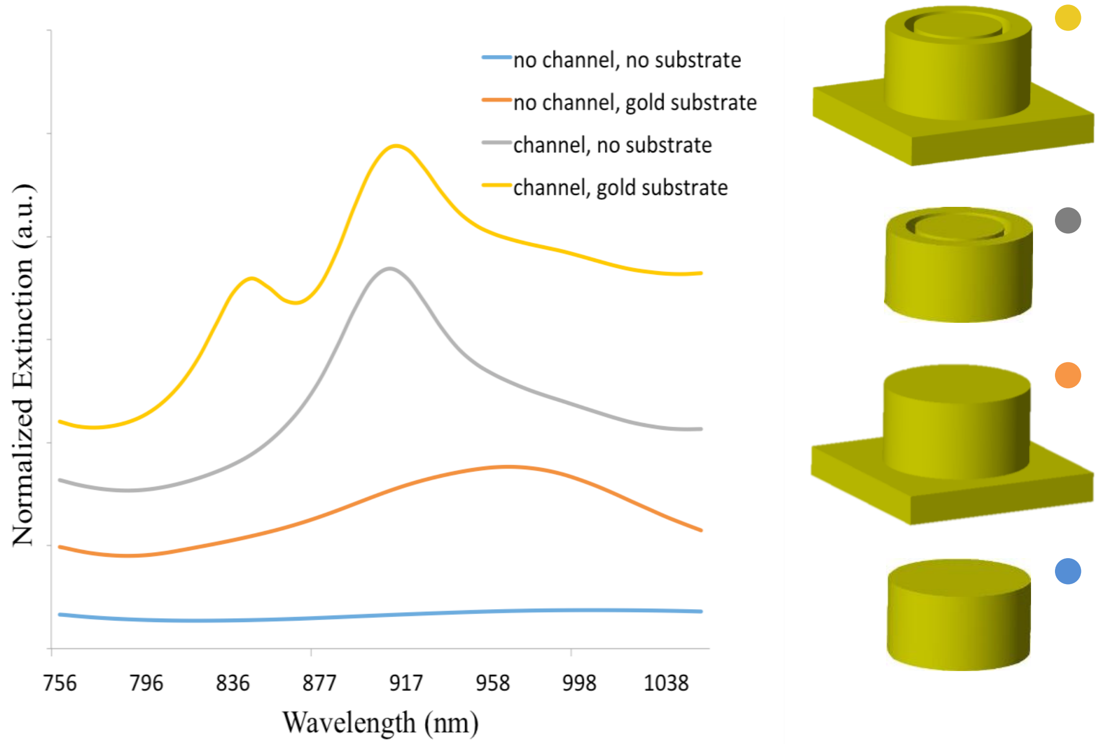

Figure 27: Stack plot highlighting the effect of channel and substrate on the extinction in the CNP.

§3.2.7 EFFECT OF POLARIZATION ON MODE DYNAMICS

The mode patterns that exist in the CNP naturally depend on the polarization of the incident light. Here we will explore two interesting cases, first we will investigate how linearly polarized incident light interacts with the CNP, then we will see how changing the polarization to a circularly polarized incident beam affects the mode dynamics in and around the CNP.

LINEAR POLARIZATION

Linearly polarized light incident on a CNP excites a Fabry-Pèrot resonance within the cylindrical channel, and in terms of plasmon hybridization, this dipolar bonding resonance

(DBR) can be tuned with gap size. The cylindrical channel plasmons have a pronounced narrow DBR peak as we have already seen in Figure 23. For smaller gap sizes, this DBR peak results from plasmon scattering at the small gap. Figure 23 also illustrates a redshift in the DBR peak for decreasing gap size, indicating a stronger coupling of the plasmonic energy into the channel as the gap size becomes larger as expected. Figure 28 shows the electric field distribution on the upper surface of the CNP under illumination with linearly polarized light oriented normal to the upper surface of the CNP. This shows that very large field enhancements ($E_{inc}/E_{channel}$ = 360) are possible when taking advantage of the reflected field.

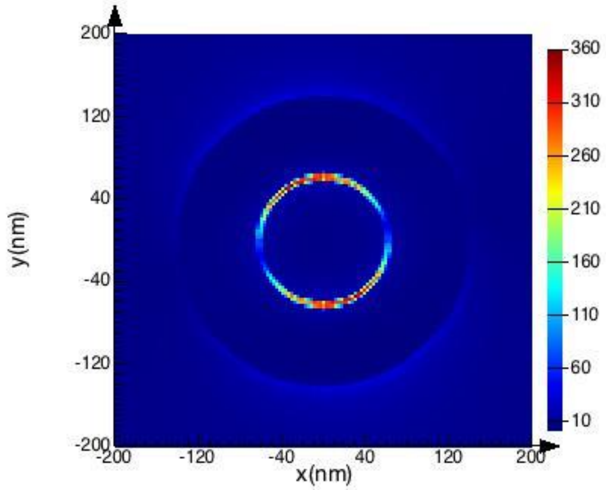

Figure 28: Fabry-Pèrot resonance resulting from illumination with linearly polarized light oriented normal to the CNP demonstrating 360x E-field enhancement.

CIRCULAR POLARIZATION

Upon excitation with circularly polarized light, the CNPs support whispering gallery modes in the cylindrical channel. Figure 29 shows a sequence of still images of a WGM in an *XY*-plane crossection of a CNP under illumination from a normally incident beam with circular polarization obtained with a time-domain FDTD monitor of the electric field distribution from a 2.67 femtosecond pulse.

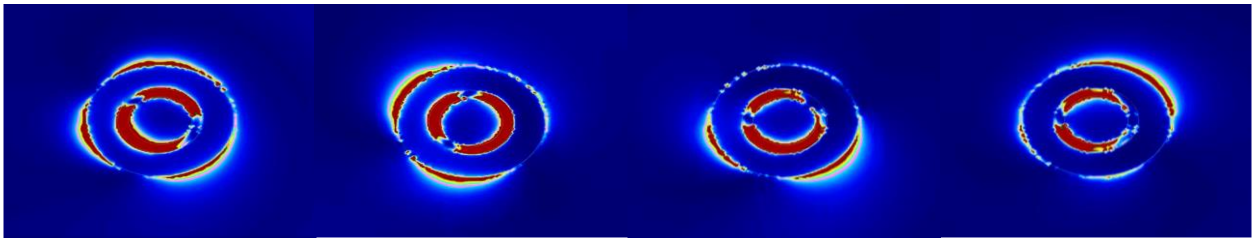

$t_0 = 0$ $t_1 = 10$ fs $t_2 = 20$ fs $t_3 = 30$ fs

Figure 29: Time sequence of a whispering gallery electric field mode in an *XY*-plane cross-section of the CNP.

CHAPTER 4: OUT OF PLANE FANO RESONANCE IN CNP

§4.1 INTRODUCTION

Fano resonance is the result of the quantum mixing of a discrete state and a continuum of states.[53] In plasmonic systems these states typically take the form of dark mode (subradiant) and bright mode (superradiant) or background continuum radiative waves.[54] They have attracted attention in the research community because they allow the excitation of quasi-localized modes with suppressed radiative damping allowing for the development of active plasmonics and nanolasers.[55] Additionally, the characteristic Fano asymmetric lineshape is highly sensitive to changes in the local dielectric environment, as its narrow linewidths are ideal for refractometric sensing.[13, 14, 19]

§4.2 BACKGROUND

In 1961, Ugo Fano discovered an asymmetric resonance in the quantum mechanical study of autoionizing states of atoms.[53] This Fano resonance was different in lineshape and origin from typical Lorentzian resonances. Fano correctly described this resonant phenomenon by attributing it to an interference of continuum and discrete wavefunctions.

Figure 30 shows how the quantum mixing of the wavefunctions of the continuum and discrete resonances leads to the characteristically asymmetric Fano resonance.

Later it was realized that other wave phenomena such as those found in optics can exhibit Fano resonances as well. Plasmonic systems are no exception, and the continuum resonance can come from background radiative waves, or bright mode resonances.[54]

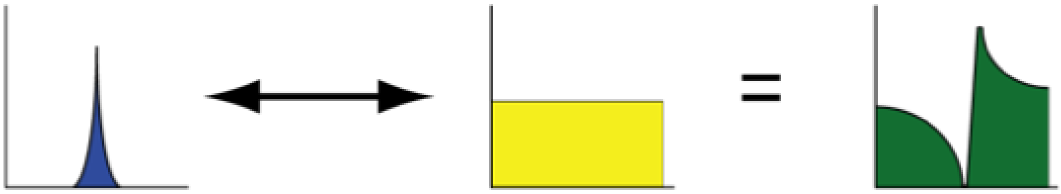

Figure 30: Fano resonance as described by the mixing of two wavefunctions.

§4.3 METAMOLECULE ANALYSIS

The following study numerically evaluates a quasi-three-dimensional plasmonic metamolecule (metamaterial unit cell) composed of a gold-dielectric coaxial nanopillar on a gold substrate as discussed previously. Metamolecules of this nature possess near-field “molecule-like” electromagnetic fields, which give rise to tunable light-matter interactions, and can have emergent far-field “material-like” behavior when assembled into an array (metamaterial).

Structural asymmetries can give rise to Fano resonances, but it is not a necessary condition for the phenomenon, as clusters of particles have also been shown to exhibit the characteristically asymmetric lineshape of the plasmonic Fano resonance.[56, 57]

Metamaterial unit cell structural asymmetries in 2D as depicted in Figure 31a give rise to in-plane (in-plane here is defined as parallel to the substrate) Fano resonances. These particular resonances have been observed in systems where there is a form of symmetry-breaking such as the “nanoegg”, dual-disk ring or non-concentric disk/ring cavity.[41-44]

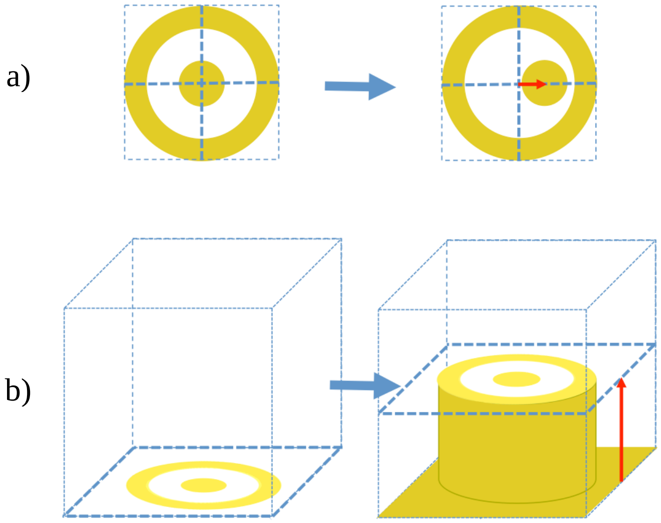

Figure 31: Comparison of a) 2D and b) 3D symmetry breaking.

The CNP metamolecule investigated here is designed to optimize the local field enhancements in the nanostructure, and to support out-of-plane (OOP) plasmon interference. The graphic in Figure 31b describes how this quasi-3D metamolecule has a 3D analog of the 2D symmetry breaking which has been shown to induce a Fano resonance. Simulated extinction spectra reveal a Fano-like resonance in the CNP believed to result from the interference of the radial electric field component of a discrete dipolar plasmon resonance in the channel $(\vec{E}_{ch,\rho})$ and a spatially perpendicular electric field from the pillar’s reflected surface plasmon’s radial electric field $(\vec{E}_{p,\rho})$ component as depicted in Figure 32.[58] Herein we show that a narrow dark mode such as those found in 2D concentric ring disk cavities (CRDC) can interfere with a broad bright mode made available as a result of the reflection of the outer pillar surface plasmons from a metallic substrate beneath the nanostructure. The resulting resonance exhibits a continuously tunable Fano-like resonance over a range of cylindrical channel gap widths, heights of the CNP, incident excitation angles, and permittivities of the superstrate.

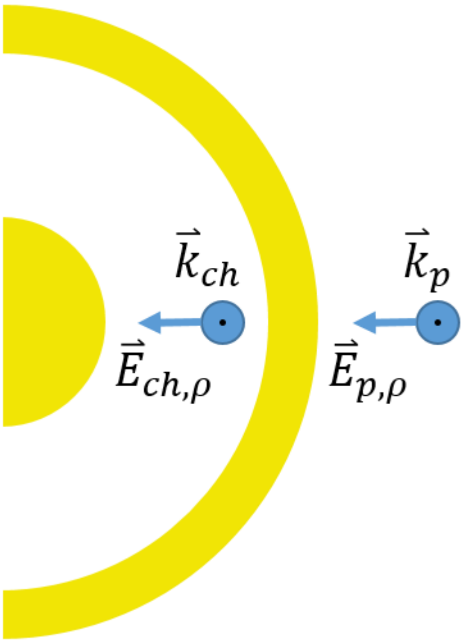

Figure 32: Possible interference mechanism for OOP Fano resonance occurring at the top of the CNP.

For a CNP with dimensions h = 210 nm, r_3 = 140 nm, r_{avg} = 50 nm, g = 10 nm, we find that under normal incidence, a Fano-like resonance as observed around λ = 683 nm as seen in Figure 33.[58] The inset E-field plots in this figure show the *XY* and the *XZ* plane electric field profiles at each resonance peak in the plot. At 820 nm we see the DBR resulting from the channel plasmons, and now we can also observe another resonance at 594 nm as well as a small peak at 683 nm. The E-field profiles at 820 nm show the familiar Fabry-Pèrot dipolar resonance in the channel resulting from the normally-incident linearly polarized excitation beam. The E-filed profiles at 594 nm display a quadrupolar field in the *XY* profile and the reflected surface plasmon's E-field on the side of the nanopillar is visible in the *XZ* profile. The peak at 683 nm is thought to arise from the mixing of these two resonances, the bright mode at 594 nm and the dark mode at 820 nm. This Fano resonance thus occurs from the interference of the channel plasmon and the phase retarded plasmons on the side of the pillar. The E-field profile for the quadrupolar resonance is very telling. It shows that the quadrupolar field as excited corresponds to when the pillar plasmons have a minimum at the top of the pillar. This drives the dipolar mode to interact with the quadrupolar mode resulting in the Fano resonance.

To examine the effect of varying the height of the CNP, extinction spectra was obtained by sweeping over heights from 70 nm to 230 nm in increments of 20 nm. The results of the parameter sweep are shown in Figure 34. The graph is oriented in such a way such that the Fano resonance peaks are hidden, however we can see that the DBR peak is at a maximum at a CNP height of 150 nm, and the quadrupolar peak is at a maximum at a CNP height of 210 nm. Both dipole and quadrupole peaks are seen to rise to a maximum value then fall again as the height of the CNP is increased further. Due to the inability for our computer to handle simulations beyond the height of 230 nm, we are not able to see beyond this data, however one can intuit that this oscillatory trend would continue as height increases, with an eventual decay of the maxima as the pillar plasmons reach their decay lengths. Under normal incidence, we can see the Fano resonance clearly at the larger CNP heights, yet at shorter pillar heights, the Fano resonance is seen in the case of normal incidence around λ = 655 nm for g = 5 nm and λ = 685 nm for g = 7.5 nm as depicted again in Figure 35 which is from data previously discussed in Figure 23.[58] The size of the channel gap thus plays a fundamental role in the establishment of the Fano resonance. This is due to the fact that at smaller gap sizes, the field enhancement is generally greater than the larger gap sizes, thus providing a greater electric field magnitude from the channel's contribution to the Fano resonance.

In addition to changing the height and the gap size of the CNP, it has also been observed that even a very small increase in the incident angle significantly increases the interaction between the channel's dark mode and the pillar's bright mode.[58] A 2° incident excitation is enough to create a significant increase in the weak interaction between these two modes. Figure 36 shows the extinction spectra from the same CNP that produced Figure 23, however now the incident light is oriented at 2° away from the normal as depicted in the inset image in the figure.

The adjustment of the CNP's geometrical parameters and/or the angle of incidence can be used to control the radiative damping of the dark mode, and thus the degree of interaction between the dark mode and the phase retarded radiative waves it interferes with.

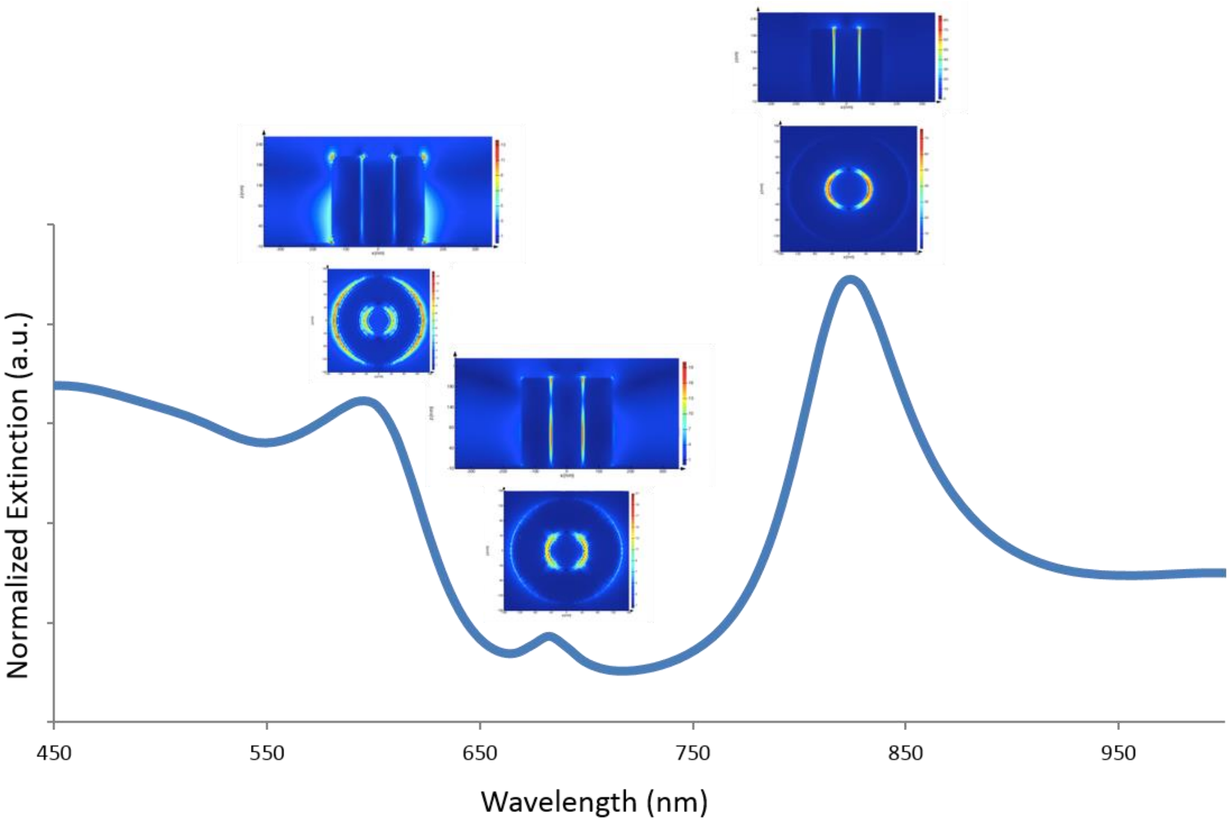

Figure 33: Extinction spectra for CNP under normal incidence with h = 210 nm, g = 10 nm.

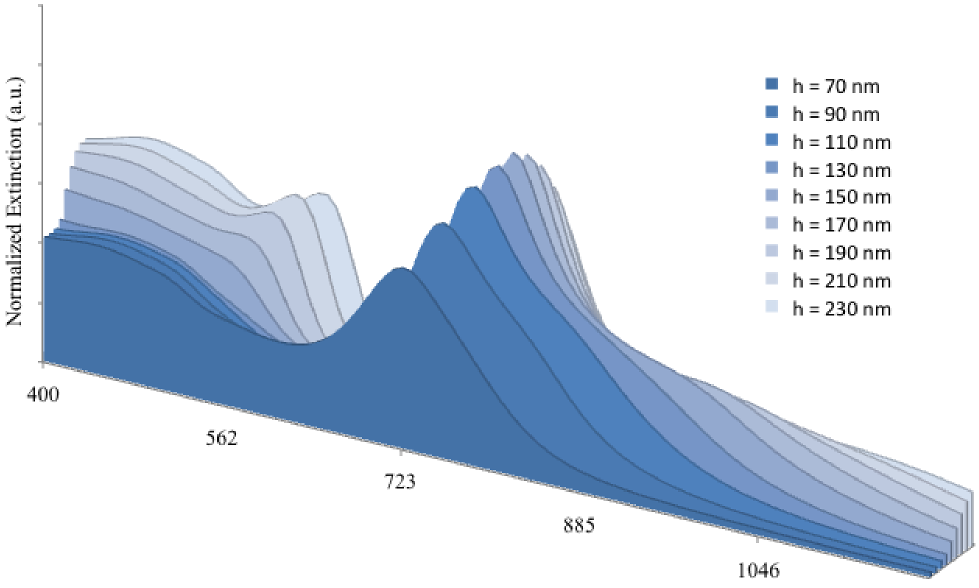

Figure 34: Extinction spectra for *g* = 10 nm CNP with various heights.

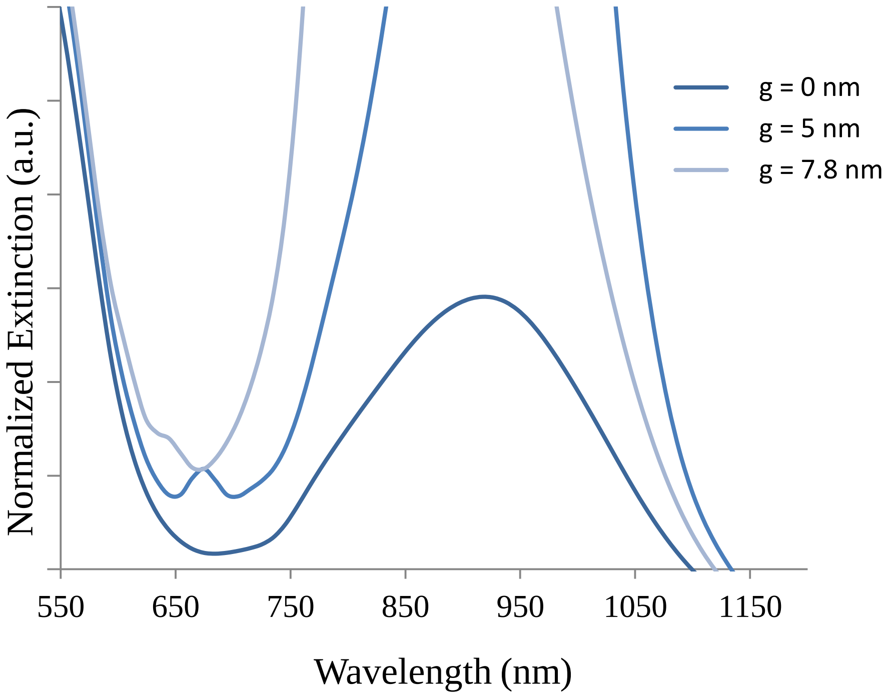

Figure 35: Extinction spectra for various channel widths for CNP with $r_{avg}=((r_2-r_1))/2=50$ nm and *h* = 130 nm.

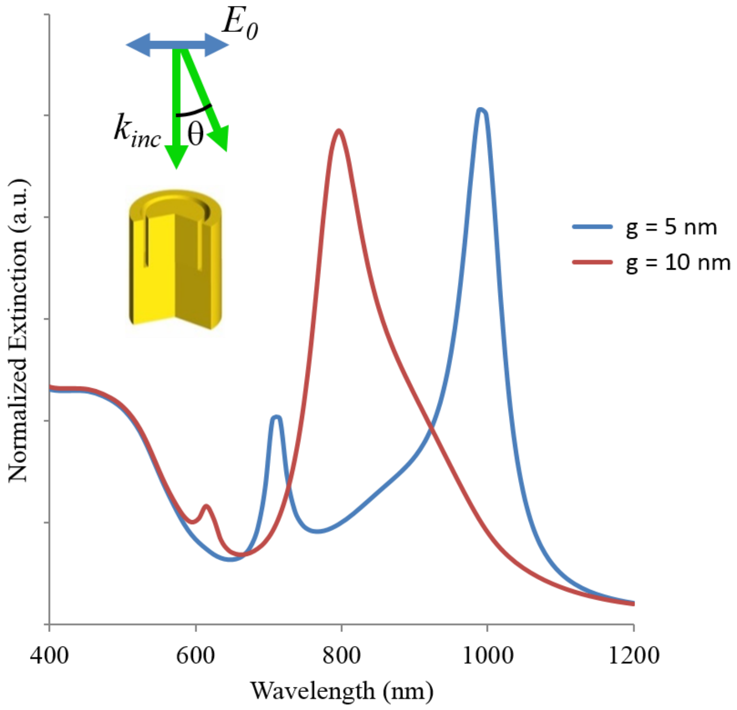

Figure 36: Extinction spectra for two gap sizes at 2° incidence.

§4.4 METAMATERIAL ANALYSIS

When the metamolecule is repeated in a square array and analyzed, other emergent phenomena arise. Specifically, there is now a dependence on the spacing between the CNP unit cells (pitch). In the following, we investigate the extinction spectra of CNP square arrays with a large pitch (*p* = 1500 nm), which we will refer to as the “large array” and is depicted graphically (not to scale) in Figure 37. For the large array, we can assume that the incident beam only couples with one CNP at a time in our region of interest, as the pitch is greater than the largest wavelength simulated. Later on, we will examine the effect of varying the pitch to see how it influences the spectra.

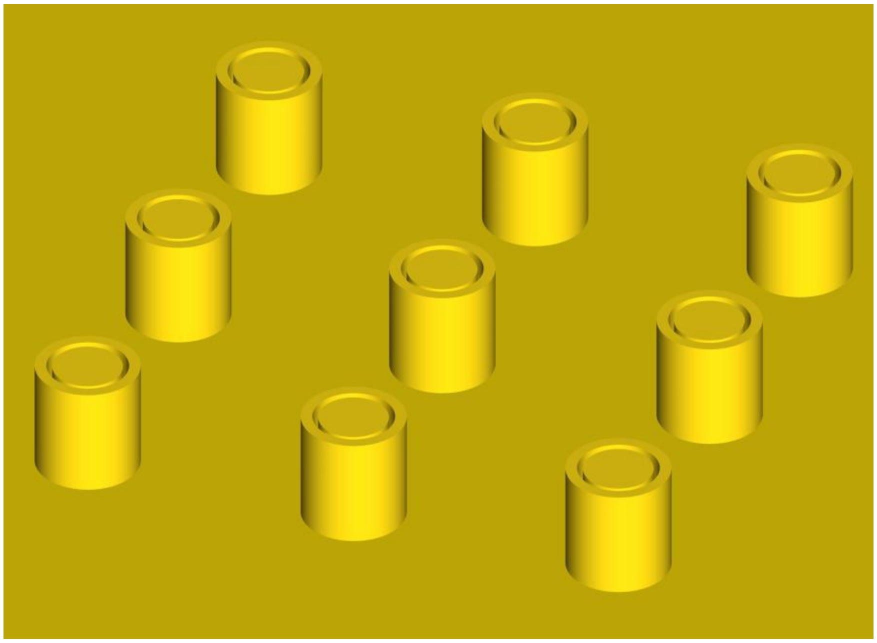

Figure 37: CNP square array.

The extinction spectra for the large array is shown in Figure 38 for 0°, 2°, and 4° incidence over a range of superstrate indices of refraction each with a $\Delta n = 0.01$. As we can see from the results, there is a slight redshifting of all the spectra with increasing superstrate indices. This redshifting is believed to be due to a dynamic depolarization of the plasmonic fields due to the increase in the refractive index of the superstrate. Between around $\lambda = 1025$ and $\lambda = 1095$ we again see an asymmetric resonance characteristic of a Fano resonance. The redshifting of this peak is more dramatic than the rest of the spectra, and we believe that this is due to the coupling with the phase retarded wave reflected from the substrate, and this coupling is enhanced for increasing angle of incidence, as the oblique angle of the excitation beam lends more of its EM momentum to the contributing radial component of the reflected pillar surface plasmon.

The observed resonances in the large array occurs at a spectral position that is redshifted 445 nm with respect to the Fano resonance observed in the spectrum for the metamolecule. In addition, the dark mode has been shifted outside of the simulated frequency range.

In Figure 39, we see the effect of varying the pitch of the metamaterial. We can see that for smaller pitch, there is a broad, superradiant peak atfor the $p = 280$ nm case centered near $\lambda = 877$ nm that becomes dark and redshifted as the pitch is increased. This resonance is highly symmetric at small pitch values and becomes slightly asymmetric as the pitch increases, with the slope of the resonance is steeper on the blue side.

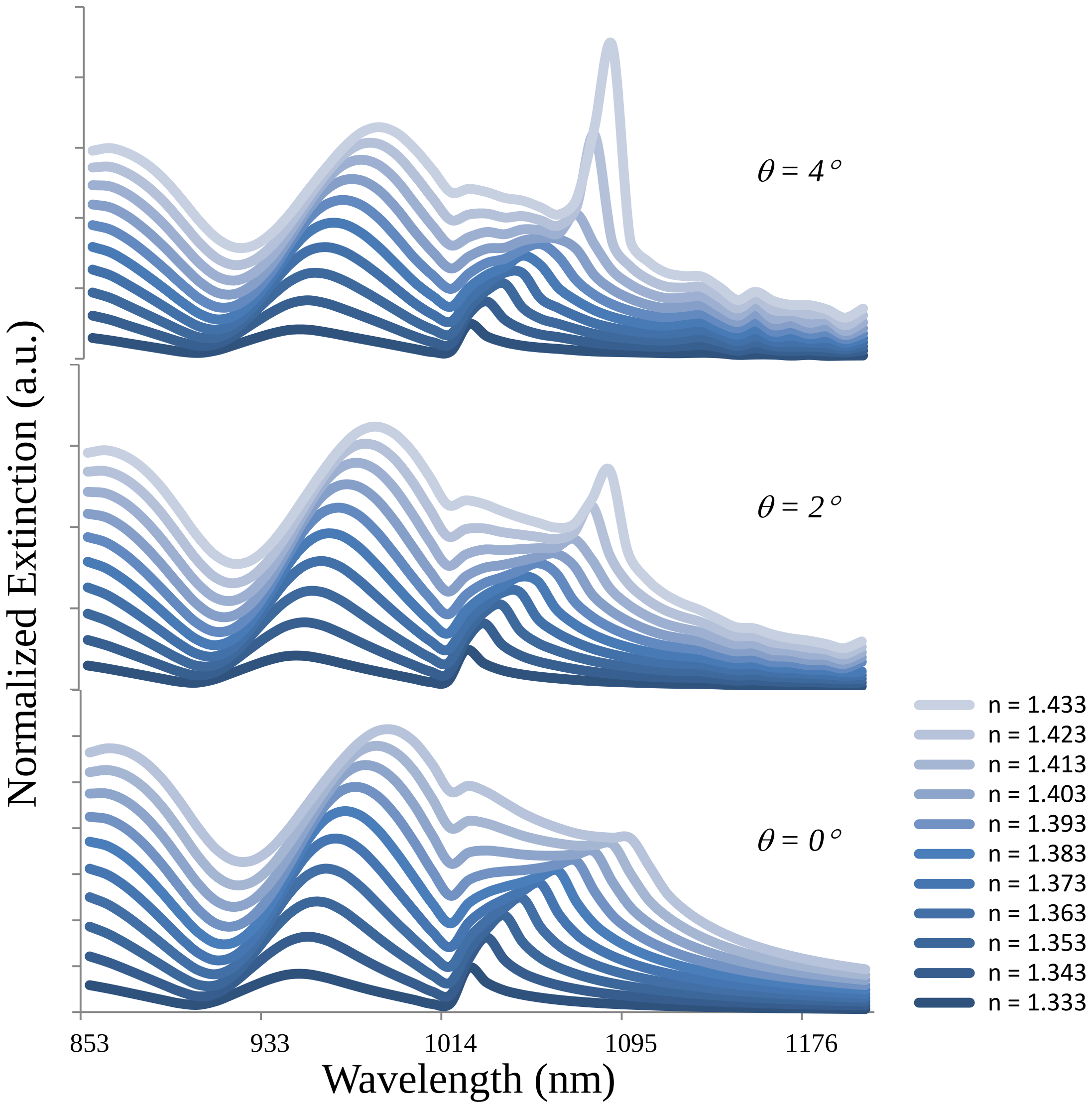

Figure 38: Extinction spectra for various superstrate indices for CNP array with 1500 nm pitch.

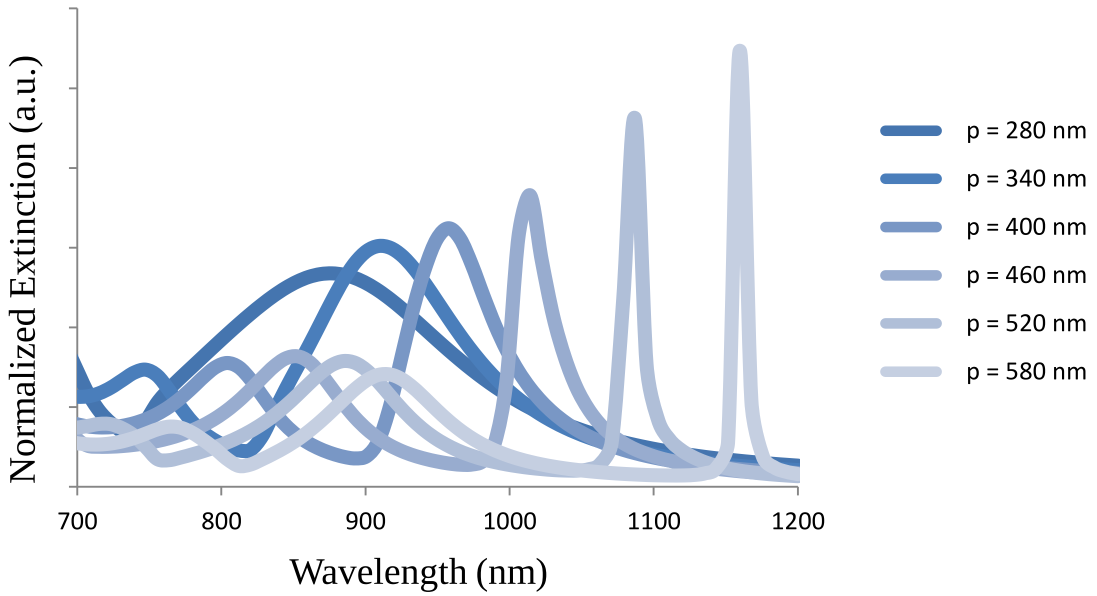

Figure 39: Extinction spectra for CNP array with varying pitch.

§4.5 CONCLUSIONS

A novel gold plasmonic nanostructure that supports plasmonic resonances and also exhibits a Fano resonance in the near infrared region of the spectrum has been studied numerically, and has been found to exhibit high tunability, robust control of its spectral features, and a new path toward designing 3D plasmonic nanostructures.

The presence of the resonance at the top of the CNP is in the ideal position for refractometric sensing, as the ideal plasmonic biosensor will have the resonance localized further into the superstrate so that it can better interact with the analyte. Additionally, the interaction of in-plane and OOP fields creates opportunities in the design of 3D nanostructures with multiple Fano resonances, where resonance from structural symmetry breaking in one plane can interfere with Fano resonances arising from symmetry breaking in another intersecting plane.

Based on the findings of our work, it is evident that the origination of the Fano resonance from asymmetries in 2D plasmonic nanostructures can be extended to include asymmetries in 3D plasmonic nanostructures as well. A broken symmetry in the 3D unit cell can enable the coupling of optically dark modes with a phase retarded bright mode.

CHAPTER 5: CNP FOR REFRACTOMETRIC SENSING

§5.1 INTRODUCTION

In this work, resonant modes in a 3D plasmonic nanostructure are shown to enhance the sensitivity to changes in the local dielectric environment via hybridized surface plasmon resonance. Fabry-Pérot resonant modes excited by linearly polarized incident coherent light, or WGMs excited by circularly polarized light in the near-IR are shown to exhibit dimer-like field enhancement and long resonant lifetimes in a nanostructured cylindrical channel which extends into the bulk of the superstrate. These features enable this CNP metamolecule and its associated metamaterial to be excellent candidates for use as refractometric sensing.

Three-dimensional or quasi-three-dimensional plasmonic nanostructures supporting strong electric field confinement have been found to support resonance from out-of-plane plasmonic resonances.[46, 58, 59] The CNP structure was designed to take advantage of this out-of-plane plasmonic interaction to confine and enhance fields within the gold cylindrical channel and enhance the sensitivity of the array to changes in the bulk dielectric medium.

§5.2 BACKGROUND

The healthcare industry is in need of low-cost biosensors for point of care, real-time diagnosis of diseases in developing countries, and fast genetic mapping.[60] This colorimetric optical detection scheme allows for the fast, real-time identification of biomarkers. Biosensors in general have various configurations and materials, but all operate based on the function of four critical components: 1) a transduction element (such as a plasmonic nanostructure), 2) a medium which carries the analyte to be measured, 3) a binding agent attached to the transducer, and 4) a data read-out system. As an example, Figure 40 shows the setup employed by Chen et al. which illustrates the function of a LSPR biosensor.[61] Gold nanostructures are functionalized with a binding agent (biotin) and are in an aqueous environment. Once the biomolecules (horseradish peroxidase (HRP)) are introduced, the binding event between the HRP and the biotin releases a high refractive index precipitate which shifts the read-out spectrum by some $\Delta\lambda$. As discussed in chapter 2, detection of small changes in the refractive index of a dielectric has been achieved by measuring shifts in the transmission or reflection wavelength of LSPR systems such as the CNP system under investigation. Optical detection of small changes in the local refractive index of a dielectric material serves as a measure of molecular binding events, as the shift in the extinction spectrum of the plasmonic system can be directly correlated to the detection of a known number of molecules. Indeed it has been shown that a wavelength shift of approximately 1 nm corresponds to the binding of one molecule of HRP.[62]

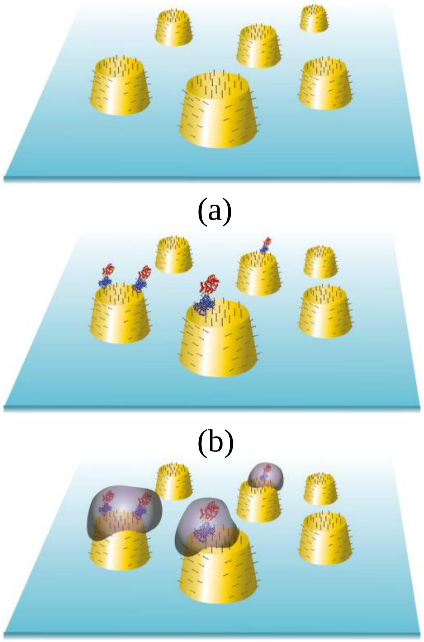

(a)

(b)

(c)

Figure 40: LSPR biosensing setup. a) Functionalized plasmonic nanostructures b) bind with biomarkers and c) release a high refractive index precipitate.

§5.3 RESULTS

For the numerical simulations used in this study, the CNPs had a period of 1500 nm to avoid anomalous scattering effects between metamolecules in the array. While anomalous scattering has been shown to increase the sensitivity of LSPR sensors [46], elucidation of optimal metamolecule geometrical configurations is a more fundamental route to maximize the sensitivity of LSPR biosensors. The CNP metamolecule used in this work had the following dimensions: $(r_2 - r_1)/2 = 60$ nm, h = 130 nm, r_3 = 140 nm.

The numerical reflection data from the CNP metamaterial is reported in

Figure 41, where light is incident on the CNP in the direction of k_{inc}, the linearly polarized wavevector of the excitation source directed normal to the pillar. The refractive index of the superstrate of the CNPs under normal and off-axis illumination was varied, and the resonance peak in the near-infrared regime was used to calculate the sensitivity of the CNP array to changes in the bulk dielectric environment.

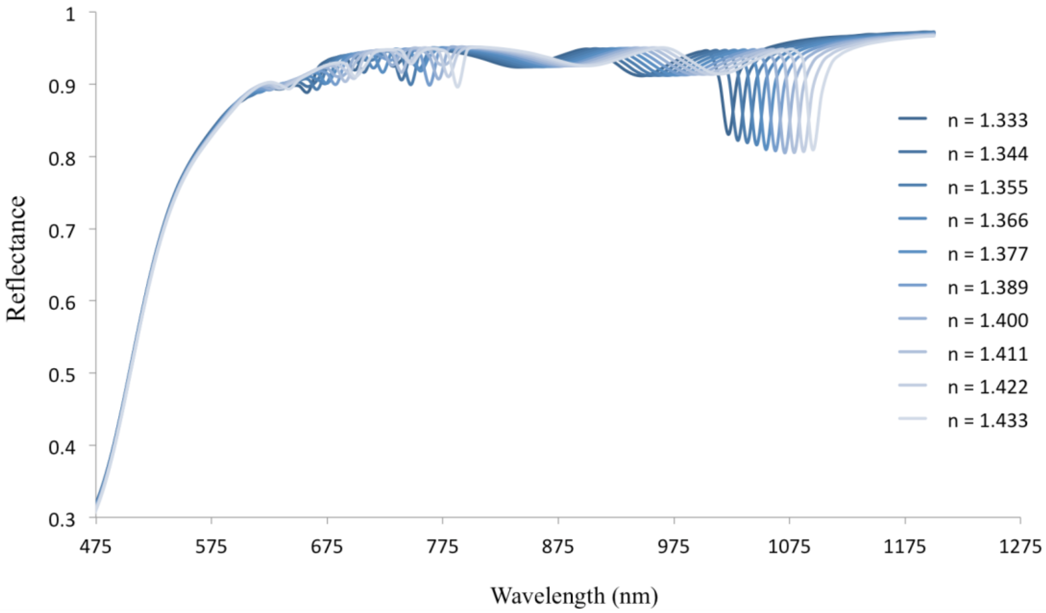

Figure 41: Reflection spectra of CNP array.

Using Equation (23), we can use the reflectance data to calculate the FoM of the CNP array. Examining the dips in the reflection spectrum, we can correlate the shifts in the spectrum with the corresponding refractive indices, as shown in Figure 42 and Figure 43 below. By inspecting the numerical results of the dips between 1022 nm and 1103 nm which have a full width at half maximum of ~12 nm, and an index sensitivity of $\Delta\lambda \cong 8$ nm, a FoM of 68 is found for this system. This is a very competitive FoM for the measurment of a non-Fano resonance peak as compared to the results from recent studies as can be seen in Appendix

§B.1. While not a Fano resonance, the dipolar resonances responsible for the peaks in the plot correspond to maxima in the pillar plasmons outside the CNP, thus the channel plasmon resonane couples with the pillar mode, enhancing the available energy to the channel resonance.

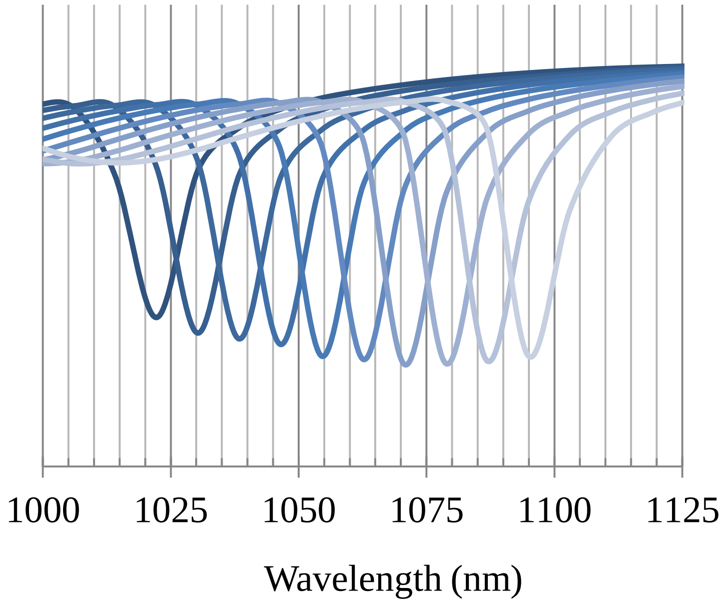

Figure 42: Dip positions in reflectance spectrum for CNP array.

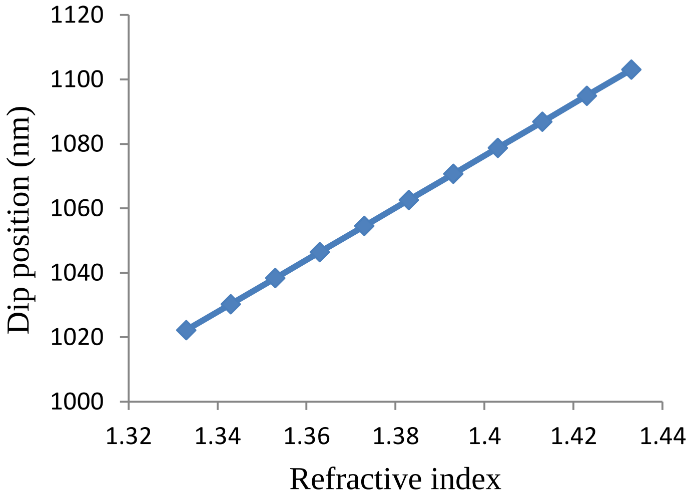

Figure 43: Calculation of FoM - dip position versus superstrate refractive index.

§5.4 CONCLUSIONS

In this chapter, we numerically investigated the dipolar resonances found in the extinction spectra associated with the CNP to determine the nanostructure's ability to function as a refractometric sensor. The spectral range under investigation ranged from 400 nm to 1200 nm excitation wavelengths. Toward the red end of this range, we found that the narrow, dark dipolar resonance which was determined to arise from the excitation of Fabry-Pèrot resonances in the channel due to normally incident light have corresponding reflectance dips that can be easily measured experimentally and have a theoretical FoM of 68.

CHAPTER 6: CNP PLASMONIC TWEEZERS

§6.1 INTRODUCTION

As discussed in section 2.2.2, EM fields can provide trapping forces that can be used for the localization and manipulation of subwavelength particles similar to how classical trapping experiments take advantage of the EM gradient force around a diffraction-limited focus. In this chapter, we theoretically investigate the forces available for plasmonic trapping due to resonances in the CNP nanostructure. We show here an exact calculation of an expression for the forces due to the channel plasmons in the CNP by evaluating the Maxwell stress tensor (MST) of a TM mode in the CNP's cylindrical channel in the limit of an infinite coaxial cable. As only TM modes are possible for surface plasmons, this calculation serves as the full analytical expression of the EM force possible due to an excited channel mode in an infinite coaxial cable. We then numerically solve the MST around a dielectric test particle suspended above the channel of the CNP and find forces exceeding a magnitude of 10.5 nN in the *z*-direction on a 10 nm diameter test sphere in vacuum 10 nm above the surface of the CNP under 100 mW illumination at 626 nm, which is approximately an order of magnitude higher than most other plasmonic trapping systems reported in the literature. Two systems with comparable trapping forces have been identified in the literature, and were realized using a double pillar structure (F_{trap} ~ 2 nN on 1μm diameter polystyrene ($n = 1.6$) microspheres in oil ($n = 1.5$) @ 440 mW incident laser power) [25], and anti-reflection coated titania microspheres (F_{trap} ~ 1.2 nN on 1μm diameter coated (n_{core} = 2.3/ n_{shell} = 1.78) microspheres in water (n = 1.33) @ 1.1 W) [27].

The nanostructure used in this study has a distinct advantage over some of the other nanoplasmonic systems which have shown an ability to impart forces on other dielectric and metallic objects in their vicinity. As we have discussed previously in this work, the CNP is designed to utilize the plasmonic field reflected from the substrate in addition to the resonant fields already present in the system. The phase matching of the reflected field with the channel plasmon creates an extremely strong resonance that can be used for sensing and trapping. Here we demonstrate the capability of our system to produce nanonewton scale forces, and show that stable trapping regions exist above the upper surface of the CNP making this design an important contribution to the field of plasmonic trapping and force transduction.

§6.2 BACKGROUND

As opposed to other force transduction and particle trapping technologies able to trap particles in the range $1\text{ nm} < d < 100\ \mu\text{m}$, where d is a characteristic dimension of the particle, optical tweezing offers several advantages. Other technologies suitable for trapping objects in this size range are hydrodynamic trapping, dielectrophoretic trapping, magnetic trapping, and acoustic trapping. Only optical tweezing offers trapping capabilities of objects at room temperature below 1 μm, making it the exclusive option for the trapping many prokaryotic cells and large molecules. In addition to its high resolution, optical tweezing also can exert forces ten to one hundred times stronger than the other technologies even at low to moderate laser powers.[63] Optical tweezers are the only technology listed that enables *in vivo*, noninvasive trapping of organelles within cells, can be easily extended to multiple traps using a holographic phase grating, enables the trapping and manipulation of single particles without the need for micro/nanostructures or complex sample section configurations, and can be made biologically safe using appropriate materials, laser powers and wavelengths. Optical tweezer systems also have the advantage of being combined with several imaging modes, such as brightfield/darkfield, phase contrast, differential interference contrast, and epifluorescence. They can also be made to exert a variable force by adjusting the laser power.

Traditional optical tweezers utilize a system of optical elements to focus coherent optical light into a tight focus. The focal point of the optical tweezing system has momentum carrying photons traveling through the focus which impart momentum onto a microscale object by refracting through and scattering off of the particle ($\boldsymbol{F}_{scat}$). Additionally, there is a force associated with electric field's intensity gradient around the focal point ($\boldsymbol{F}_{grad}$). The total optical force on a particle, which is composed of scattered and gradient forces is ($\Sigma\boldsymbol{F} = \boldsymbol{F}_{grad} + \boldsymbol{F}_{scat}$). Considering a small dielectric sphere whose radius a is such that the sphere falls within the Rayleigh regime, where $2\pi a \ll \lambda_{inc}$, or at least $a \ll \frac{\lambda_{inc}}{10}$, as when operating within the Rayleigh regime we consider that the particle's entire surface re-radiates with the same phase as the incident light, and we consider the dielectric sphere to be composed of electric dipoles which in the presence of an electric field will polarize such that the scattering force scales as a^6 [64], whereas the gradient force scales like a^3 due to the particle's electric polarizability, and therefore the scattering force decreases with particle size faster than the gradient force. Therefore, the gradient force dominates as particle size decreases in the Raleigh regime. The strong electric field enhancement in plasmonic systems offers a way to increase the optical forces on microscopic and nanoscopic particles by providing this gradient force. As discussed previously, plasmonic trapping systems can be designed to trap particles well under the diffraction limit of the excitation beam. However, as particle size decreases, its position relative to the trap becomes more susceptible to Brownian motion, as can be seen from the Stokes-Einstein equation:

$$\frac{\langle x^2 \rangle}{2t} = \frac{RT}{6\pi\eta a N} \tag{33}$$

where x is the one dimensional position of a trapped particle, R is the universal gas constant, T is the temperature in the local vicinity of the particle, η is the viscosity of the surrounding fluid, N is Avagadro's number, and t is time. Thermal management is therefore a very important consideration when designing plasmonic trapping systems.

The condition for stable trapping of a particle in the Rayleigh regime is such that the EM trapping potential energy overcomes this thermal energy such that $k_B T \ll |U|$, where

$$U \approx -\int \boldsymbol{F}_{grad}\, d\boldsymbol{r} = -\frac{1}{2}|\alpha|\langle \boldsymbol{E}^2 \rangle \tag{34}$$

is the optical potential energy, α is the particle's electric polarizability, and $\langle \boldsymbol{E}^2 \rangle$ is the time-averaged electric field. The right hand side of Equation (34) is the just the Lorentz force acting on an electric dipole in the Rayleigh approximation.

The CNP is considered now for nanometric trapping by theoretically determining the presence of a non-negligible force at the upper face of the CNP, and then numerically evaluating this force on a test particle in the vicinity of the enhanced electric field in the channel above the CNP.

§6.3 METHODOLOGY

In this study, we first derive an analytical expression for the force able to be exerted due to channel plasmons in the CNP. Then full three-dimensional FDTD simulations are conducted to model the plasmonic forces on a test particle above the upper surface of the CNP. The CNP metamolecule has an outer radius *r* = 140 nm, height *h* = 210 nm, a channel gap width *g* = 25 nm located at an average radius of 50 nm with a channel depth of *d* = 50 nm (which is greater than the wavelength of the channel plasmon). As in the previous chapter, the CNP is located on a gold substrate whose negative real anisotropic permittivity is given by Johnson and Christy [50] and whose background medium is a vacuum (*n* = 1). Using Lumerical's multi-coefficient model, a dielectric nanosphere is modeled as having a refractive index n = 2, and is evaluated for various diameters and distances above the CNP. The forces are calculated on this test sphere using the MST $\overleftrightarrow{T}_{ij}$ and the forces are carried by the Poynting vector $\boldsymbol{S}(\boldsymbol{r},t)$; the total force at time t can be derived from the Lorentz force equation and has the form:

$$\boldsymbol{F}(\boldsymbol{r},t) = \boldsymbol{\nabla}\cdot\overleftrightarrow{\mathrm{T}}_{ij} - \frac{1}{c^2}\frac{\partial \boldsymbol{S}(\boldsymbol{r},t)}{\partial t}. \tag{35}$$

In these simulations, force is calculated as the surface integration of $\overleftrightarrow{T}_{ij}$ around a virtual rectangular volume surrounding the test nanosphere.

§6.4 PLASMONIC FORCES IN AN INFINITE COAXIAL CABLE

The TM plasmonic modes in a plasmonic coaxial cable can exert forces due to the momentum flux of the EM field within and around the coaxial cable. The most precise and informative way of describing the forces associated with the EM field is the use of the MST, which can be interpreted as the negative momentum flux of the EM field. The MST can be arrived at in a straightforward way beginning with the Lorentz force equation:

$$\boldsymbol{F}_L = q(\boldsymbol{E} + \boldsymbol{v} \times \boldsymbol{B}) \tag{36}$$

which has a full vectorial expression for the force associated with the EM field:

$$\begin{gathered}\boldsymbol{F}_L = \varepsilon_0[(\boldsymbol{\nabla} \cdot \boldsymbol{E})\boldsymbol{E} + (\boldsymbol{E} \cdot \boldsymbol{\nabla})\boldsymbol{E}] + \frac{1}{\mu_0}[(\boldsymbol{\nabla} \cdot \boldsymbol{B})\boldsymbol{B} + (\boldsymbol{B} \cdot \boldsymbol{\nabla})\boldsymbol{B}] \\ -\frac{1}{2}\boldsymbol{\nabla}\left(\varepsilon_0 E^2 + \frac{1}{2}B^2\right) - \varepsilon_0 \frac{\partial}{\partial t}(\boldsymbol{E} \times \boldsymbol{B}).\end{gathered} \tag{37}$$

This expression can be written in a more compact, and more helpful form:

$$\boldsymbol{F}_L = \boldsymbol{\nabla} \cdot \overleftrightarrow{T}_{ij} = \oint \overleftrightarrow{T}_{ij} \cdot \hat{n}\, d\boldsymbol{a} \tag{38}$$

Where $\overleftrightarrow{T}_{ij}$ is the MST, which is a symmetric dyadic tensor (rank-2 tensor):

$$\overleftrightarrow{T}_{ij} = \varepsilon_0\left(E_iE_j - \frac{1}{2}\delta_{ij}E^2\right) + \frac{1}{\mu_0}\left(B_iB_j - \frac{1}{2}\delta_{ij}B^2\right) \tag{39}$$

which has components in cylindrical coordinates which can be viewed graphically as shown in Figure 44 and represented in a matrix as:

$$\overleftrightarrow{T}_{ij} = \begin{bmatrix} T_{\rho\rho} & T_{\rho\phi} & T_{\rho z} \\ T_{\phi\rho} & T_{\phi\phi} & T_{\phi z} \\ T_{z\rho} & T_{z\phi} & T_{zz} \end{bmatrix}. \tag{40}$$

For TM waves, there is an electric field component in the z and ρ directions, and a magnetic field component in the ϕ direction only. For waveguided EM waves, $\varepsilon E^2 = \mu H^2$, so for a TM wave the MST in the cylindrical channel of the coaxial cable is:

$$\overleftrightarrow{T}_{ch} = \begin{bmatrix} 0 & 0 & \varepsilon E_\rho E_z \\ 0 & 0 & 0 \\ \varepsilon E_\rho E_z & 0 & -\varepsilon E^2 \end{bmatrix}. \tag{41}$$

The diagonal terms in the MST represent *pressures*, and the off-diagonal terms represent *shears*, so there is a momentum flux generating a pressure-like force proportional to εE^2 in the longitudinal direction, and a momentum flux generating a shear-like force with components in the radial and longitudinal directions.

The total force associated with the EM field confined in the channel of the coaxial cable is thus:

$$\boldsymbol{F}_{ch} = \oint \overleftrightarrow{T}_{ch} \cdot \hat{n}\, d\boldsymbol{a} = \varepsilon \oint \left[\left(E_\rho E_z\right)\hat{\rho} + \left(E_\rho E_z - E^2\right)\hat{z} \right] \cdot \hat{n}\, d\boldsymbol{a}, \tag{42}$$

where the surface of integration has its normal in the longitudinal direction for the z-components, and along the radius for the ρ-components.

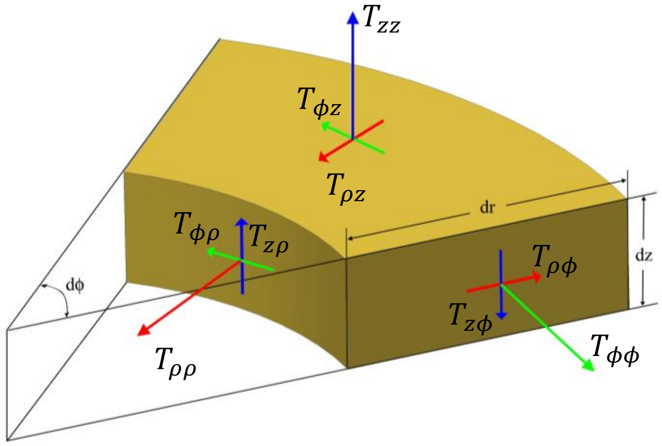

Figure 44: MST components in cylindrical coordinates.

§6.5 RESULTS

We first numerically verify that there are only *z* and *x*-components to the force as measured near the CNP gap. Figure 45 shows a series of results of the MST computation on the test sphere located 40 nm radially away from the center of the CNP, where the force is normalized to the surface area of the sphere and calculated using 100 mW laser power—which is a typical laser power used for traditional optical tweezers. Each simulation is run with at least two mesh points (calculation nodes) within the sphere and between sphere and the CNP upper surface. We can see from these plots that for each simulation, there is a resonance in the *x* and *z*-components of the force at 626 nm, and the *y*-components are zero across all wavelengths for each simulation as well. The *x*-components in these simulations correspond to the radial ρ-components in the cylindrical coordinate system, as used in the previous section. The appearance of only the *x* and the *z*-components of the force on the test sphere resulting from the TM Fabry-Pérot plasmons in the cylindrical gap agrees well with the result for the analytical force prediction, Equation (42). We can see in Figure 45a that at a 10 nm distance from the CNP gap, FDTD results predict forces greater than 10.5 nN on a 10 nm diameter test sphere under 100 mW excitation laser power.

In Figure 45 we also observe that the force on the test sphere falls off quickly with distance from the CNP upper surface. This is expected, since the gradient force is primarily responsible for the EM force on the test sphere in this simulation, so there is a strong dependency on proximity to the concentrated electric fields near the surface of the CNP.

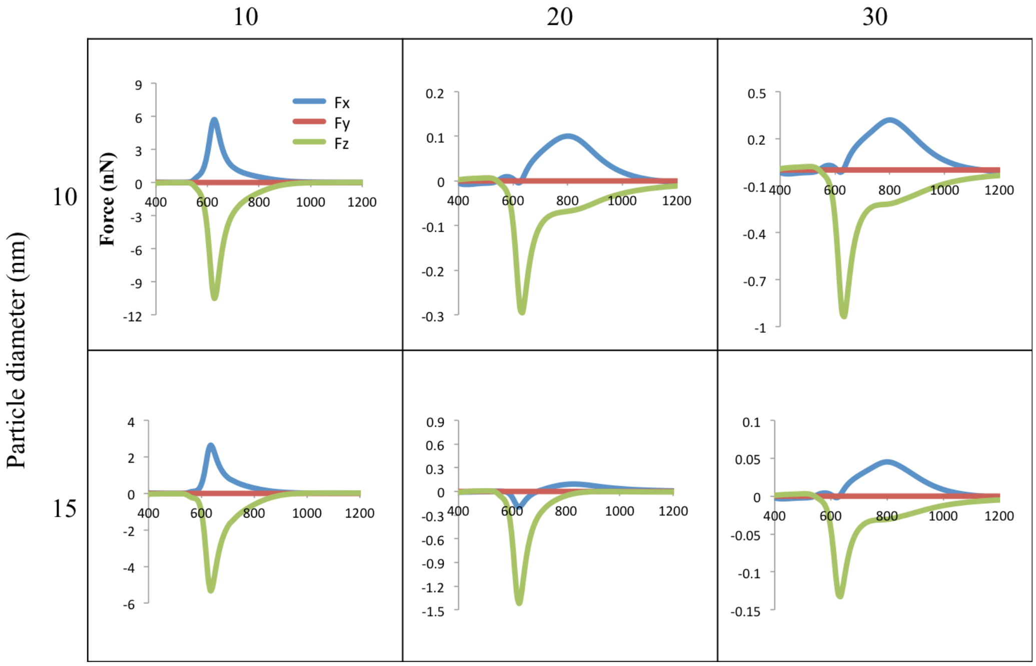

Figure 45: All force components on the test sphere for different conditions 40 nm radially away from the center of the CNP.

This CNP system is capable of exerting forces on particles as small as 1 nm in diameter with force magnitudes sufficient for stable trapping as can be seen in Figure 46.

Next we examine the capability of the CNP to serve as plasmonic tweezers by evaluating its ability create a stable trapping region. Figure 45 shows a stack plot for various distances of the test sphere away from the surface of the CNP. Each plot’s independent axis corresponds to the *x*-component of the force on a 10 nm diameter test sphere under 100 mW excitation at 626 nm, and the dependent axis is the distance away from the center of the CNP. We learn from these results that several stable trapping positions exist along the radius of the CNP’s upper surface.

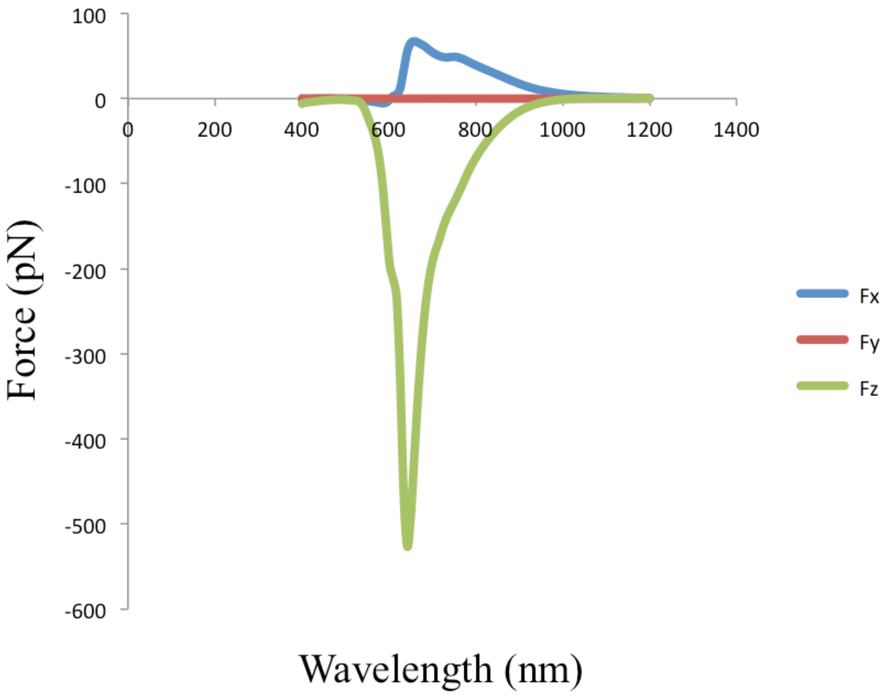

Figure 46: Force components on 1 nm diameter test sphere located 10 nm above the upper surface of the CNP.

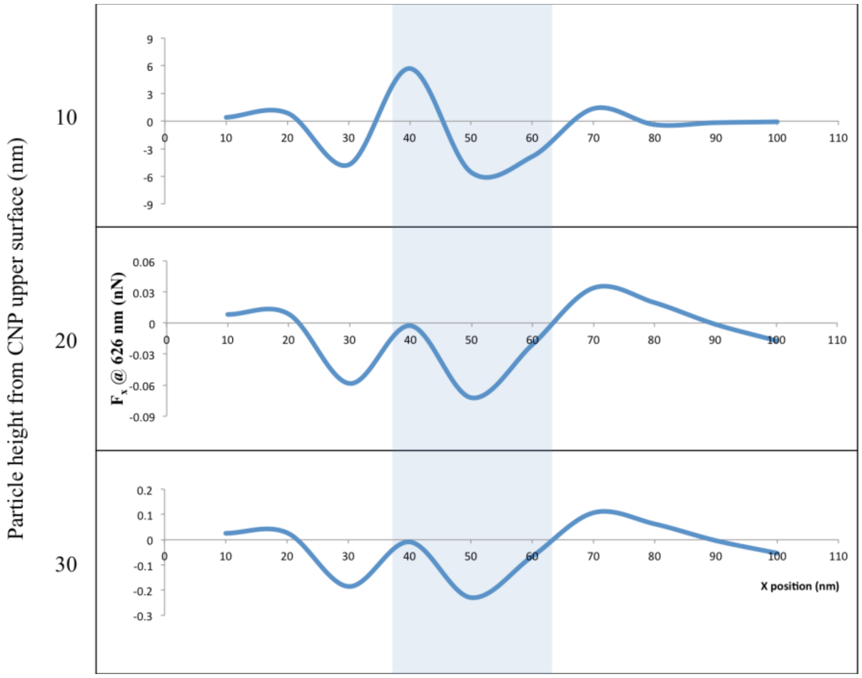

Figure 47: Force along x-axis as a function of sphere position along x relative to cylindrical channel gap position denoted by the grey strip centered at 50 nm.

Similar to Figure 45, this figure also highlights the sensitivity of the system to the proximity to the upper surface of the CNP. In Figure 47 we can see that the condition for a stable trap is only met for the case when the test sphere is located 10 nm away from the CNP upper surface, although weak trapping is still theoretically possible outside the gap even for the case when the test sphere is 30 nm away from the CNP upper surface, as opposing forces with magnitudes in the 100 pN range are still possible in this case.

Figure 46 shows the position of the particle relative to the stable trap when the particle is located 10 nm above the gap. The reason for the offset from the center of the gap toward the center of the CNP may be due to additional momentum gained from the reflected plasmons surrounding the CNP outer perimeter, providing a nonzero radial shearing force which may sum with the channel plasmons to radially displace the test sphere toward the center of the CNP.

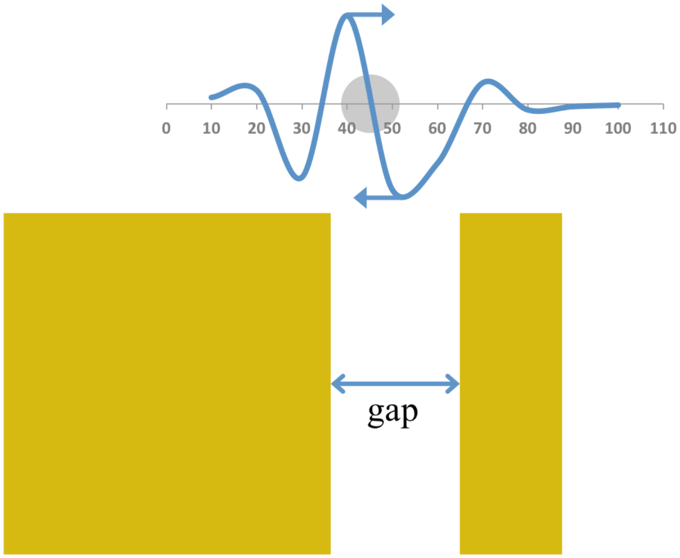

Figure 48: Position of a 10 nm diameter test sphere during a stable trapping event. Graph shows x-component of the force for 626 nm incident radiation.

As we can see from the electric field distribution in Figure 49, there is negligible contribution from the plasmons on the pillar at this wavelength, therefore this increased force on the particle must be due to the coupling of the channel plasmons with the phase retarded reflected light from the substrate. The hybridized mode visible in this figure has the surface charge distribution as determined from the PHT in Figure 13 overlaid in the image. As the resonance is subradiant, it must be due to either the high frequency subradiant or the low frequency subradiant mode from the PHT. In an analysis of the plasmonic modes in the primitive nanostructures which compose the CNP, it has been shown that the CNP core plasmon in the high frequency subradiant mode is antisymmetric with respect to the outer shell plasmon, and it thus has negligible effect on the hybridization of the channel mode.[48]

The force on that object is proportional to the gradient of the electric field of k_{inc} and therefore the E-field enhancement dictates the magnitude of the force felt by particles in the vicinity.

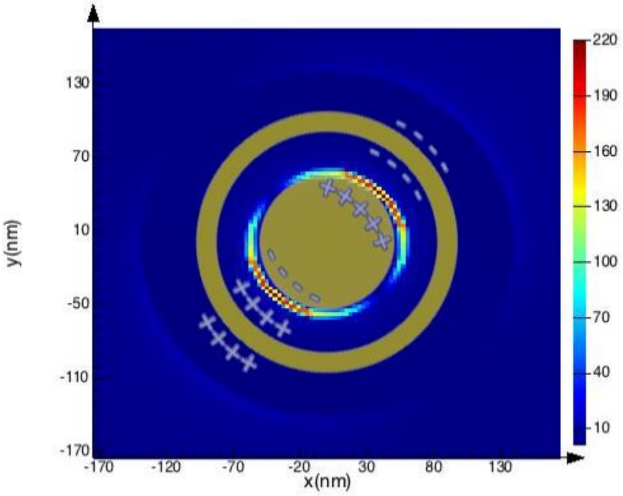

Figure 49: E-field distribution in the *XY* plane at the top of the CNP under normally incident light. Overlaid on the image is the surface charge distribution as determined from the PHT in §3.1.1. The color bar shows the magnitude of the E-field enhancement.

§6.6 CONCLUSIONS

In this study it is shown that minor modifications to gold nanostructures can create large field enhancements that generate strong forces on nearby dielectric particles. It is demonstrated that cavities with sub-wavelength dimensions are able to support surface plasmons and can be used for local field enhancements which can provide increased electric field enhancement capable of generating nanonewton forces; enabling the CNP with design elements such as the reflective plasmonic coupling, to be leveraged to increase field enhancement and provide strong forces on this scale. Additionally, a simulated 626 nm TFSF plane wave source was observed to excite a strong plasmonic eigenmode in the cylindrical channel of the CNP responsible for generating forces on a test sphere at various positions and of different diameters. These results provide evidence that through plasmonic nanostructure design, plasmon resonances can be engineered that enable the nanostructure to perform as a force transducer and the CNP has been shown to be capable of supporting stable trapping events utilizing nanonewton forces.

CHAPTER 7: CONCLUSIONS AND FUTURE DIRECTIONS

§7.1 INTRODUCTION

The work presented in this dissertation is a study of a novel 3D metallic nanostructure on a metallic substrate with multiple applications in the field of plasmonics. Numerical results obtained in chapters 3-6 contain the main contributions of this work. The CNP design boasts many advantages over other nanoplasmonic systems, mostly due to the utilization of the reflected field in the structure. In chapter 4 we discussed the discovery of a Fano resonance in the CNP. The occurrence of this particular Fano resonance is unique in that this OOP Fano resonance is not a result of a Wood's anomaly [46], is not a result of the mixing of higher and lower order resonances in-plane [65], is not a result of a substrate-mediated resonance [31], but rather a new route toward the design of 3D plasmonic nanostructures—the engineering of Fano resonances due to phase-retarded field interactions with other in-plane resonances.

In addition to exhibiting a new manifestation of Fano resonances in plasmonic nanostructures, the CNP extends into the bulk of the superstrate, making it a viable design for refractometric biosensing applications. Chapter 5 of this dissertation discusses the results which show a theoretical FoM of 68 possible for the dimensions chosen for the study when measuring the shift in the narrow dipolar resonance in the extinction spectrum for small changes in the local dielectric index of refraction. Compared to other LSPR biosensors, the FoM for this CNP design is world-competitive. The high FoM is thought to also be due to the contribution of the phase-retarded field on the side of the pillar to the channel plasmon resonance. Lastly, chapter 6 provides numerical evidence that the enhanced resonances found in the CNP system also enable this design to produce EM forces in regions near the nanostructure making it a candidate for plasmonic trapping applications.

The remainder of this chapter is dedicated to the direction of future research in the area of plasmonic sensing and actuation for the CNP nanostructure. Fabrication of the CNP nanostructure, verification of biosensing capabilities of the CNP nanostructure through reflectance spectroscopy analysis of biological analyte binding events, and the plasmonic trapping of aerosol particles for Raman spectroscopy.

§7.2 FABRICATION

To experimentally verify the Fano resonance presented in chapter 4 would requires the development of new techniques that enable the fabrication of ultra-high aspect ratio nanostructures. The dimensions of the CNP exhibiting the strongest simulated Fano resonances has a cylindrical channel with an aspect ratio of 21:1, making it difficult to fabricate. To achieve extremely smooth metallic features suitable for supporting quality surface plasmons, a template stripping (TS) process is employed to fabricate the CNP metamaterial as seen in Figure 50. Due to the lattice constant mismatch between the hydrogen silsesquioxane (HSQ) electron beam (e-beam) resist and gold, the gold is easily removed from the template, and the smooth lithographic features are well preserved in the gold nanostructure.[11] The copper layer acts as a heat sink, and is required since under illumination with moderate laser power, the strong field enhancement in the CNP metamolecules will create a strong local thermal gradient in the superstrate that may be beyond its boiling point.[33] More information regarding the heat associated with the plasmonic field enhancement can be found in sections §3.2.6 and §6.2.

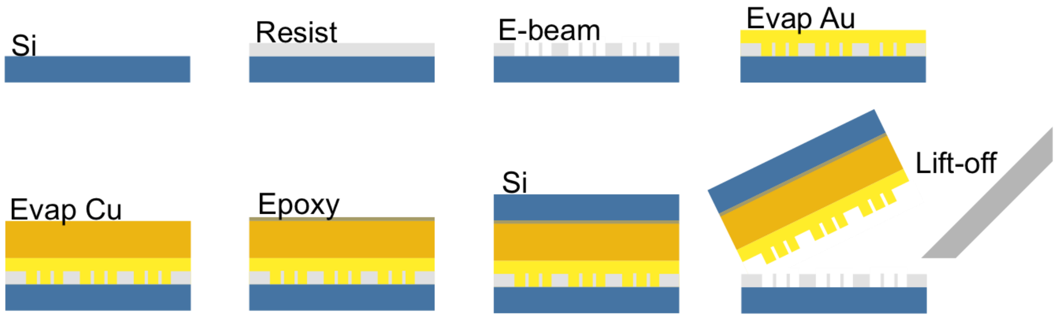

Figure 50: Template stripping process.

The e-beam that was used to pattern the resist was the Vistec 5200 at Penn State University. To create the nanostructure, the machine needed to be coded to create this particular pattern. The code for a particular CNP is given in Appendix §B.2. After the e-beam writing step, tetramethylammonium (TMAH) was used to develop the resist. Once developed, the resulting templates were imaged using a scanning electron microscope (SEM). A characteristic image of a CNP template is shown in Figure 51 highlighting the resolution capabilities of the e-beam. Considering these CNPs have a height h = 130 nm, for a gap size g = 30 nm, this equates to at 4.33:1 aspect ratio. Aspect ratios above this are difficult to fabricate and work is ongoing to fabricate the higher aspect ratios.

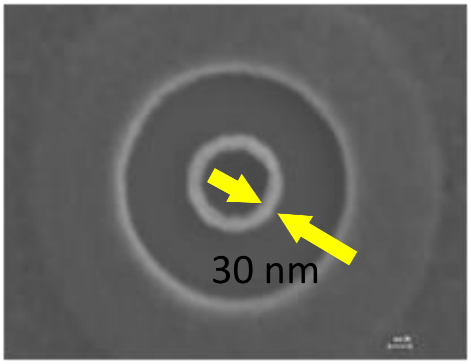

Figure 51: SEM image of HSQ template showing a 30 nm gap size.

Once the template was created, 99.999% pure 1/8” diameter gold pellets and 99.999% pure 1/8” diameter copper pellets obtained from the Kurt J. Lesker Company were thermally evaporated using a Thermionics VE 90 thermal evaporator. Using a quartz crystal thickness monitor on the thermal evaporator, gold was deposited onto the template by passing 100 A of current through a tungsten “boat” which evaporated the metal onto the substrate suspended approximately 16” above the boat. For 2.25 g of gold, the quartz monitor measured a thickness of 464 nm and using 4.5 g of copper, the quartz monitor measured a thickness of 906 nm. Once the metals were deposited onto the template, a small amount of epoxy was applied to the rear face of the copper layer and a silicon wafer was applied to act as the substrate. After a 24 hour curing time for the epoxy, the two wafers were separated mechanically by prying them apart with a razor blade. The resulting sample was again imaged in the SEM to verify that the pillars were successfully removed from the template. Figure 52 shows a completed CNP array fabricated with the TS method (scale bar reads 300 nm). Figure 53 shows a close-up image of an individual pillar (scale bar reads 30 nm).

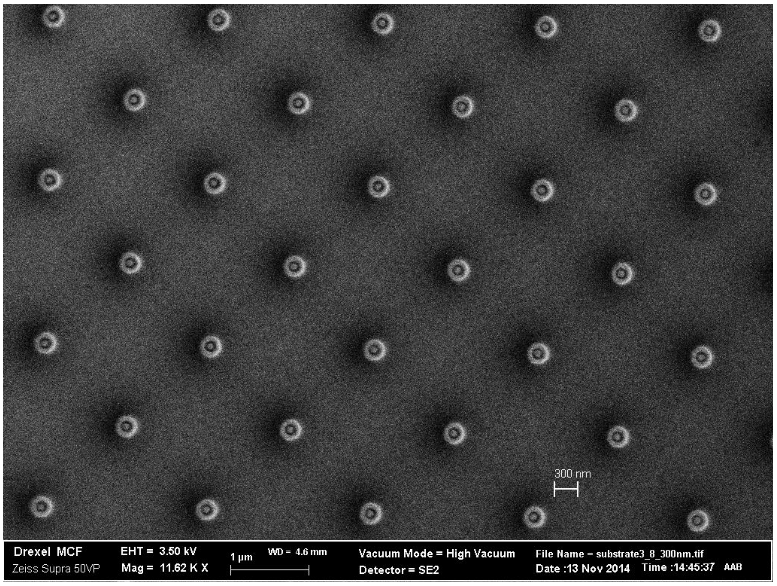

Figure 52: SEM image of a fabricated CNP array (scale bar reads 300 nm).

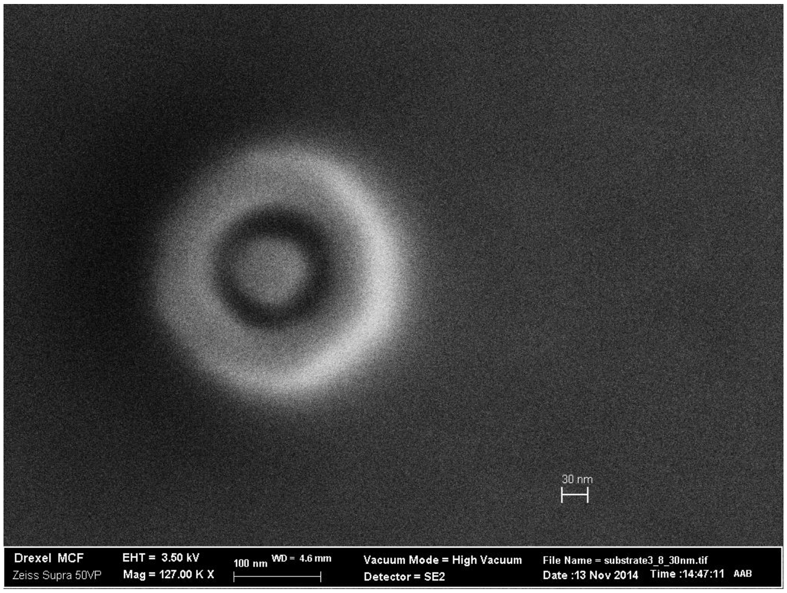

Figure 53: SEM image of a fabricated individual CNP (scale bar reads 30 nm).

While the fabrication of the high-aspect ratio templates is still a challenge, the numerical simulations of the CNP design show a lot of promise for applications in the field of plasmonics. In addition to its prospects as a refractometric biosensor, this particular design could possibly be utilized in a SERS system, enabling the simultaneous trapping and inspection of deep sub-micron sized particles.

§7.3 FUTURE DIRECTIONS

Naturally, the future direction for theoretical work is experimental verification of the results. Due to limitations in the resolution of current electron beam fabrication techniques, verification of some of the results presented in this thesis will have to wait until the techniques are developed further. However, in the following subsections, experiments are discussed which can be performed using larger CNP gap sizes, as the Fano resonance is not needed in these applications of the CNP.

§7.3.1 BIOSENSING

The aim of this dissertation was to numerically and analytically evaluate a 3D plasmonic nanostructure for the applications of refractometric sensing and force transduction for plasmonic trapping. Once the high aspect ratio CNP arrays are fabricated accurately, the experimental verification of the biosensing capabilities of the CNP nanostructure can be accomplished through a reflectance spectroscopy analysis of biological analyte binding events. Figure 54 shows the reflectance white light spectroscopy experimental configuration which will be used to evaluate the refractometric sensing performance of the CNP arrays.

Water with varying concentrations of ethylene glycol will produce the various indices of refraction for testing the metamaterial's response to the incident light spectrally broad in the near-IR range. Spectra from the ethylene glycol experimentation will be verified against the numerical results presented in chapter 5. Once the experimental sensitivity is determined, various biological analytes will be introduced to the CNP metamaterial to determine the sensitivity of the CNP to various concentrations of biomolecules.

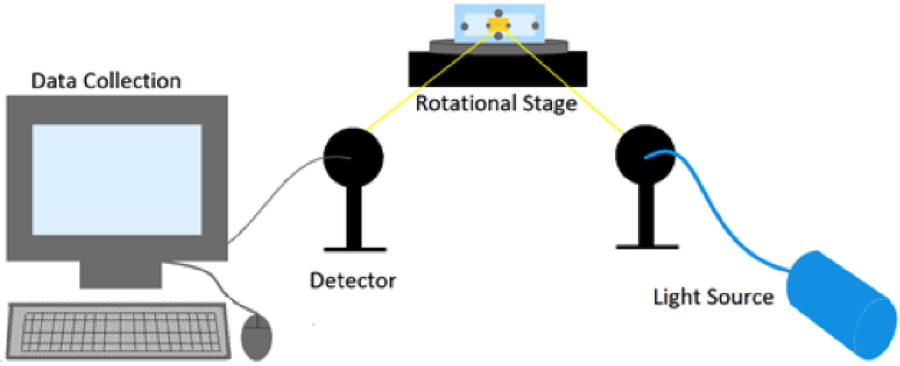

Figure 54: Reflectance setup for refractometric sensing performance analysis.

§7.3.2 PLASMONIC TRAPPING OF SUBMICRON AEROSOL PARTICLES

Optical trapping has been achieved for particles in the gas phase.[66, 67] However there is much difficulty is trapping particles smaller than 1 μm using a traditional OT setup. As discussed in chapter 6, the force on particles in this regime results primarily from the gradient force. The gradient force is established in traditional optical tweezers using a diffraction-limited laser focus and has been used to trap aerosol droplets within the range of $1\,\mu\text{m} < d < 10\,\mu\text{m}$ where d is the diameter of the droplet. While this range encompasses many aerosol particles such as pollen, plant spores, clouds and fog; sub-micron techniques are needed to analyze black carbon, smog, combustion particles and volatile organic compounds whose origins are both natural and anthropogenic and some of these compounds arising from both outdoor and indoor environmental sources have been shown to be hazardous to human health.

Using plasmonic methods similar to the work completed by Changjun Min et al discussed in chapter 2, structureless plasmon resonances can be created that have a much higher spatial resolution than the diffraction-limited laser focus of traditional optical tweezers.

The air chemistry community would benefit from a real-time, in-situ Raman spectroscopy method for the fingerprinting of sub-micron aerosol particles. POTs offers a possible solution for the stable trapping of individual sub-micron aerosol particles. A parametric study via numerical simulations can be performed to elucidate the optimal geometric configuration of the plasmonic trapping, and experimentation can be implemented using the optical tweezer setup described in Appendix A.

References

1. Maxwell, J.C., *A Dynamical Theory of the Electromagnetic Field.* 1865. **155**: p. 459-512.
2. Ritchie, R.H., *Plasma Losses by Fast Electrons in Thin Films.* Physical Review, 1957. **106**(5): p. 874-881.
3. Wood, R.W., *On a Remarkable Case of Uneven Distribution of Light in a Diffraction Grating Spectrum.* 1902. **18**(1): p. 269-275.
4. Otto, A., *Excitation of Nonradiate Surface Plasma Waves in Silver by the Method of Frustrated Total Reflection.* 1968. **216**: p. 398-410.
5. Kretschmann, E., *Die Bestimmung optischer Konstanten von Metallen durch Anregung von Oberflachenplasmaschwingungen.* 1971. **241**(4): p. 313-324.
6. Maier, S.A., *Plasmonics: Fundamentals and Applications*. 2007: Springer.
7. Dionne, J., et al., *Plasmon slot waveguides: Towards chip-scale propagation with subwavelength-scale localization.* Physical Review B, 2006. **73**(3): p. 9.
8. Fontecchio, B.T.a.A., *Polaritonic metamaterial for super resolution trapping and sensing*. 2013, IEEE Xplore. p. 554-555.
9. W. C. Chew, J.J., E. Michielssen, J. Song *Fast and Efficient Algorithms in Computational Electromagnetics*. 2001, Boston: Artech House.
10. D. S. Macintyre, S.T., *Comparison of hydrogen silsesquioxane development methods for sub-10 nm electron beam lithography using accurate linewidth inspection.* J. Vac. Sci. Technol. B, 2011. **29**(6): p. 6.
11. Xinli Zhu, Y.Z., Jiasen Zhang, Jun Xu, Yue Ma, Zhiyuan Li, Dapeng Yu, *Ultrafine and smooth full metal nanostructures for plasmonics.* Adv Mater, 2010. **22**(39): p. 5.
12. Jeffrey N. Anker, W.P.H., Olga Lyandres, Nilam C. Shah, Jing Zhao, Richard P. Van Duyne, *Biosensing with plasmonic nanosensors.* Nature Materials, 2008. **7**: p. 12.
13. Kevin A. Tetz, L.P., Yeshaiaju Fainman, *High-resolution surface plasmon resonance sensor based on linewidth-optimized nanohole array transmittance.* Optics Letters, 2006. **31**(10): p. 3.
14. Brolo, A.G., *Plasmonics for future biosensors.* Nature Photonics, 2012. **6**: p. 5.
15. Carolina Novo, A.M.F., Ann K. Gooding, Paul Mulvaney, *Electrochemical charging of single gold nanorods.* J. Am. Chem. Soc., 2009. **131**: p. 3.
16. Amanda J. Haes, C.L.H., Richard P. Van Duyne. *Nanosphere lithography: Self-assembled photonic and magnetic materials*. in *Mat. Res. Soc. Symp.* 2001.
17. Linda S. Jung, C.T.C., Timothy M. Chinowsky, Mimi N. Mar, Sinclair S. Yee, *Quantitative interpretation of the response of surface plasmon resonance sensors to adsorbed films.* Langmuir, 1998. **14**: p. 14.
18. Michelle Duval Malinsky, K.L.K., George C. Schatz, Richard P. Van Duyne, *Chain length dependence and sensing capabilities of the localized surface plasmon resonance of silver nanoparticles chemically modified with alkanethiol self-assembled monolayers.* J. Am. Chem. Soc., 2001. **123**: p. 12.
19. Amanda J. Haes, R.P.V.D., *A unified view of propagating and localized surface plasmon resonance biosensors.* Anal Bioanal Chem, 2004. **379**: p. 11.
20. Manas Ranjan Gartia, A.H., Anusha Pokhriyal, Sujin Seo, Gulsim Kulsharova, Brian T. Cunningham, Tiziana C. Bond, Gang Logan Liu, *Colormetric plasmon resonance imaging using nano lycurgus cup arrays.* Adv. Optical Mater. , 2013. **1**: p. 9.
21. Ahmet A. Yanik, A.E.C., Min Huang, Alp Artar, S. Hossein Mousavi, Alexander Khanikaev, John H. Connor, Gennady Shvets, Hatice Altug, *Seeing protein monolayers with naked eye through plasmonic Fano resonances.* PNAS, 2011. **108**(29): p. 6.
22. Amr A. E. Saleh, J.A.D., *Toward efficient optical trapping of sub-10-nm particles with coaxial plasmonic apertures.* Nano Lett, 2012. **12**(11): p. 6.
23. A. Ashkin, J.M.D., J. E. Bjorkholm, Steven Chu, *Observation of a single-beam gradient force optical trap for dielectric particles.* Optics Letters, 1986. **11**(5): p. 3.
24. Changjun Min, Z.S., Junfeng Shen, Yuquan Zhang, Hui Fang, Guanghui Yuan, Luping Du, Siwei Zhu, Ting Lei, Xiaocong Yuan, *Focused plasmonic trapping of metallic particles.* Nat Commun, 2013. **4**: p. 7.
25. A. N. Grigorenko, N.W.R., M. R. Dickinson, Y. Zhang, *Nanometric optical tweezers based on nanostructured substrates.* Nature Photonics, 2008. **2**: p. 6.
26. Farbod Shafiei, F.M., Khai Q. Le, Xing-Xiang Liu, Thomas Hartsfield, Andrea Alu, Xiaoqin Li, *A subwavelength plasmonic metamolecule exhibiting magnetic-based optical Fano resonance.* Nat Nanotechnol, 2013. **8**(2): p. 6.
27. Anita Jannasch, A.F.M., Peter D. J. van Oostrum, Alfons van Blaaderen, Erik Schaffer, *Nanonewton optical force trap employing anti-reflection coated, high-refractive-index titania microspheres.* Nature Photonics, 2012. **6**: p. 5.
28. Y. J. Zheng, H.L., S. M. Wang, T. Li, J. X. Cao, L. Li, C. Zhu, Y. Wang, S. N. Zhu, X. Zhang, *Selective optical trapping based on strong plasmonic coupling between gold nanorods and slab.* Applied Physics Letters, 2011. **98**(9): p. 3.

29. Q. Zhang, J.J.X., X. M. Zhang, Y. Yao, H. Liu, *Reversal of optical binding force by Fano resonance in plasmonic nanorod heterodimer.* Optics Express, 2013. **21**(5): p. 8.
30. M. Righini, P.G., S. Cherukulappurath, V. Myroshnychenko, F. J. Garcia de Abajo, R. Quidant, *Nano-optical trapping of rayleigh particles and ecoli bacteria with resonant optical antennas.* Nano Lett, 2009. **9**(10): p. 5.
31. Shunping Zhang, K.B., Naomi J. Halas, Hongxing Xu, Peter Nordlander, *Substrate-induced Fano resonances of a plasmonic nanocube: a route to increased-sensitivity localized surface plasmon resonance sensors revealed.* Nano Lett, 2011. **11**(4): p. 7.
32. Jing Zhang, L.C., Wenli Bai, Guofeng Song, *Hybrid waveguide-plasmon resonances in gold pillar arrays on top of a dielectric waveguide.* Optics Letters, 2010. **35**(20): p. 3.
33. Kai Wang, K.B.C., *Plasmonic trapping with a gold nanopillar.* Chemphyschem, 2012. **13**(11): p. 10.
34. Hui Wang, D.W.B., Fei Le, Peter Nordlander, Naomi J. Halas, *Nanorice: a hybrid plasmonic nanostructure.* Nano Lett, 2006. **6**(4): p. 6.
35. Fang-Fang Ren, K.-W.A., Jiandong Ye, Mingbin Yu, Guo-Qiang Lo, Dim-Lee Kwong, *Split Bull's eye shaped aluminum antenna for plasmon-enhanced nanometer scale germanium photodetector.* Nano Lett, 2011. **11**(3): p. 5.
36. Daniel W. Brandl, P.N., *Plasmon modes of curvilinear metallic core/shell particles.* J Chem Phys, 2007. **126**(14): p. 144708.
37. J. Berthelot, S.S.A., M. L. Juan, M. P. Kreuzer, J. Renger, R. Quidant, *Three-dimensional manipulation with scanning near-field optical nanotweezers.* Nat Nanotechnol, 2014. **9**(4): p. 295-9.
38. Niels Verellen, Y.S., Heidar Sobhani, Feng Hao, Victor V. Moshchalkov, Pol Van Dorpe, Peter Nordlander, Stefan A. Maier, *Fano resonances in individual coherent plasmonic nanocavities.* Nano Lett, 2009. **9**(4): p. 6.
39. Ertugrul Cubukcu, S.Z., Yong-Shik Park, Guy Bartal, Xiang Zhang, *Split ring resonator sensors for infrared detection of single molecular monolayers.* Applied Physics Letters, 2009. **95**(4): p. 3.
40. Arif E. Cetin, H.A., *Fano resonant ring-disk plasmonic nanocavities on conducting substrates for advanced biosensing.* ACS Nano, 2012. **6**(11): p. 7.
41. Feng Hao, P.N., Yannick Sonnefraud, Pol Van Dorpe, Stefan A. Maier, *Tunability of subradiant dipolar and Fano-type plasmon resonances in metallic ring disk cavities-implications for nanoscale optical sensing.* ACS Nano, 2009. **3**(3): p. 10.
42. Yuan Hsing Fu, J.B.Z., Ye Feng Yu, Boris Luk'yanchuk, *Generating and manipulating higher order fano resonances in dual-disk ring plasmonic nanostructures.* ACS Nano, 2012. **6**(6): p. 8.
43. Lifang Niu, J.B.Z., Yuan Hsing Fu, Shripad Kulkarni, Boris Luk'yanchuk, *Fano resonance in dual disk ring plasmonic nanostructures.* Optics Express, 2011. **19**(23): p. 8.
44. Yannick Sonnefraud, N.V., Heidar Sobhani, Guy A. E. Vandenbosch, Victor V. Moshchalkov, Pol Van Dorpe, Peter Nordlander, Stefan A. Maier, *Experimental realization of subradiant, superradiant, and fano resonance in ring-disk cavities.* ACS Nano, 2010. **4**(3): p. 7.
45. Rene A. Nome, M.J.G., Norbert F. Scherer, Stephen K. Gray, *Plasmonic interactions and optical forces between Au bipyramidal nanoparticle dimers.* Journal of Physical Chemistry A, 2009. **113**: p. 8.
46. Yang Shen, J.Z., Tianran Liu, Yuting Tao, Ruibin Jiang, Mingxuan Liu, Guohui Xiao, Jinhao Zhu, Zhang-Kai Zhou, Xuehua Wang, Chongjun Jin, Jinfang Wang, *Plasmonic gold mushroom arrays with refractive index sensing figures of merit approaching the theoretical limit.* Nature Communications, 2013. **4**(2381): p. 10.
47. E. Prodan, C.R., N. J. Halas, P. Nordlander, *A hybridization model for the plasmon response of complex nanostructures.* Science, 2003. **302**(5644): p. 5.
48. Moradi, A., *Plasmon hybridization in coated metallic nanowires.* J. Opt. Soc. Am. B, 2012. **29**(4): p. 5.
49. J. B. Pendry, L.M.-M., F. J. Garcia-Vidal, *Mimicking surface plasmons with structured surfaces.* Science, 2004. **305**(6): p. 2.
50. P. B. Johnson, R.W.C., *Optical constants of the noble metals.* Physical Review B, 1972. **6**(12): p. 10.
51. Palik, E.D., *Handbook of Optical Constants of Solids III*. Vol. 1. 1991: Academic Press.
52. Urzhumov, Y., *Sub-wavelength electromagnetic phenomena in plasmonic and polaritonic nanostructures: from optical magnetism to super-resolution*. 2007.
53. Fano, U., *Effects of configuration interaction on intensities and phase shifts.* Physical Review 1961. **124**(6): p. 13.
54. Gallinet, B., *Fano resonances in plasmonic nanostructures: fundamentals, numerical modeling and applications*. 2012.
55. N. I. Zheludev, S.L.P., N. Papasimakis, V. A. Fedotov, *Lasing spaser.* Nature Photonics, 2008. **2**: p. 4.
56. K. Bao, N.A.M., P. Nordlander, *Fano resonances in planar silver nanosphere clusters.* Applied Physics A, 2010(100): p. 333-339.
57. M. Hentschel, D.D., R. Vogelgesang, H. Giessen, N. Liu, *Plasmonic oligomers: The role of individual particles in collective behavior.* ACS Nano, 2011. **5**(3): p. 2042-2050.
58. B. Terranova, A.F., *Tunable Fano resonance of whispering gallery modes from out-of-plane structural symmetry breaking in press*, 2015.
59. Wei Zhou, T.W.O., *Tunable subradiant lattice plasmons by out-of-plane dipolar interactions.* Nat Nanotechnol, 2011. **6**(7): p. 5.

60. D. A. Giljohann, C.A.M., *Drivers of biodiagnostic development.* Nature, 2009. **462**(26): p. 4.
61. Si Chen, M.S., Richard P. Van Duyne, Mikael Kall, *Plasmon-enhanced colorimetric ELISA with single molecule sensitivity.* Nano Lett, 2011. **11**(4): p. 1826-30.
62. S. Chen, M.S., R. P. Van Duyne, M. Kall, *Plasmon-enhanced colorimetric ELISA with single molecule sensitivity.* Nano Lett, 2011. **11**: p. 5.
63. J. Nilsson, M.E., B. Hammarstrom, T. Laurell, *Review of cell and particle trapping in microfluidic systems.* Analytica Chimica Acta, 2009. **649**: p. 17.
64. Ysuhiro Harada, T.A., *Radiation forces on a dielectric sphere in the Rayleigh scattering regime.* Optics Communications, 1996. **124**: p. 13.
65. Feng Hao, Y.S., Pol Van Dorpe, Stefan A. Maier, Naomi J. Halas, Peter Norlander, *Symmetry breaking in plasmonic nanocavities: subradiant LSPR sensing and a tunable Fano resonance.* Nano Letters, 2008. **8**(11): p. 6.
66. Knox, K., *Light-induced processes is optically-tweezed aerosol droplets*. 2011. p. 209.
67. M. D. King, K.C.T., A. D. Ward, *Laser tweezers raman study of optically trapped aerosol droplets of seawater and oleic acid reacting with ozone: implications for cloud-droplet properties.* J. Am. Chem. Soc., 2004. **126**: p. 2.
68. Grier, D., *A revolution in optical manipulation.* Nature 2003. **424**: p. 7.

APPENDIX A: OPTICAL TWEEZER CONSTRUCTION

§A.1 INTRODUCTION

Traditional optical tweezers (OTs) primarily utilize two forces associated with a tightly focused coherent, three dimensional beam of optical light. In section 6.2 we discussed these two forces, the scattering force (or radiation pressure), and the gradient force (due to the intensity gradient of the focus). Figure 55 shows a schematic of a traditional optical trap indicating regions of the trap which are dominated by either the scattering or gradient forces on a colloidal particle. To create stable OTs, the most commonly employed method is to create a system of optical components to focus coherent light into a tight focal point. The use of high numerical aperture microscope objectives is a convenient way of realizing an optical trap which provides sufficient gradient forces to stabilize a microscale particle in three dimensions.

In this chapter, we will discuss the construction of a traditional OT system from common optical components, with descriptions of the trapping system, the viewing system, the steering system and its characterization, and the initial verification of the OT operation. At the end of the chapter, ongoing work and future directions for the use of the OT apparatus are discussed.

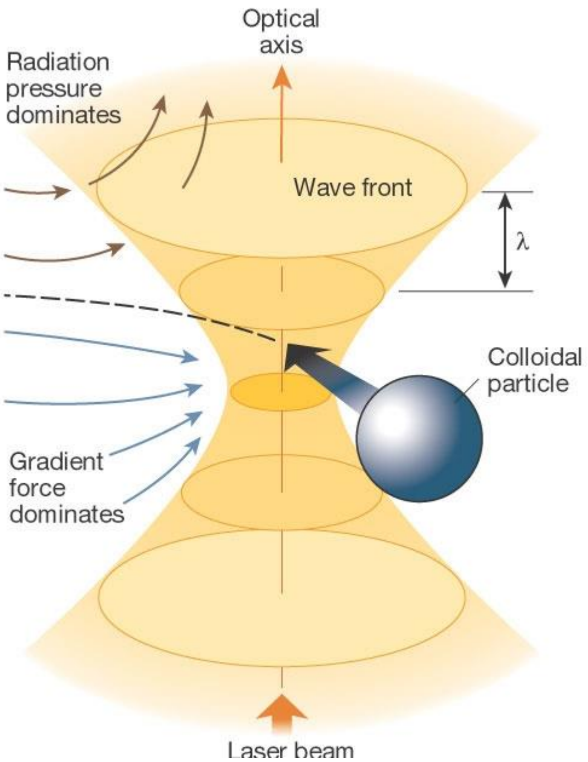

Figure 55: Traditional optical trap.[68]

§A.2 CONSTRUCTION OF OPTICAL TWEEZERS

When designing OTs, there are many factors to consider. Aside from fiber optic OT setups, most OT systems require sending the laser beam out of the plane of the optical table, thus safety becomes more of a concern. Typical colloidal tweezing setups require approximately 10 – 100 mW of laser power at the microscope objective to produce stable traps after all power losses in the system are accounted for. Since there are optical power losses throughout the setup, typical laser powers are around 100 – 200 mW, and at these laser powers, extended exposure of the eye to specularly reflected laser light becomes a serious consideration when sending the beam out of plane.

The optical system that has been constructed resembles a typical OT setup and is pictured in Figure 56. The out of plane portion of the optical tweezer system has a full aluminum enclosure accessible by vertical sliding panels. An enclosure such as this is necessary to include in any free space optics optical tweezing system design where the beam is exposed.

§A.2.1 THE TRAPPING SYSTEM

The laser in the figure is the Verdi G5 optically pumped semiconductor laser from Coherent, Inc. which emits a linearly polarized (perpendicular to the plane of the optical table) beam centered at λ = 532 nm. The laser light is passed through a collimating lens L_1, iris (not pictured), and then projected onto a digital micromirror device (DMD). The DMD is used as a two-dimensional phase grating, programmatically switching mirrors on its surface to dynamically adjust the wavefront which effectively acts as a 2D beam steering system in the setup. The DMD's surface is characterized later in this chapter. The reflected wavefront from the DMD is then sent out-of-plane of the optical table using a dichroic mirror sensitive to green light. The prepared wavefront is then incident on a high numerical aperture (N.A. = 1.25, magnification = 100x) infinity-corrected microscope objective and is subsequently focused at a half angle given by the numerical aperture equation ($\theta = \sin^{-1}\frac{1.25}{n}$), where n is the refractive index of the medium the objects to be trapped are immersed in. For water, this equates to a half angle of ~70°. Light waves passing through the sample stage are then collected by a condenser lens system and passed to another dichroic mirror after passing through L_2. Laser light that leaves the condenser is composed of rays that pass through the sample and also rays that are scattered from the trapped particle as well. The scattered light is more intense due to the large divergence of the unscattered light leaving the focal point. The laser light that reflects from the dichroic mirror above the condenser is then focused using lens L_2 into a quadrant photodiode (QPD). The QPD can track the position of the trapped particle by measuring the positional change of the beam spot resulting from the trapped particle's scattered light. The signal from the QPD is fed into a data acquisition system (National Instruments USB-6211) which is controlled by a LabVIEW virtual instrument on the USB-connected computer.

To achieve stable trapping of microscale objects, roughly in the range of 1 μm to 100 μm, one must generate at least piconewton forces. As discussed in the previous chapter, when the circumference of the particle is sufficiently smaller than the wavelength of the incident light, then the Rayliegh approximation yields analytical approximations of the forces on particles in the small particle range; however, for particles whose characteristic dimension falls outside of the Rayleigh regime, one must consider Mie theory, which provides an analytical solution of Maxwell's equations for the EM field scattering from spherical particles. This however only works for spherical particles. Experimentally, the forces in an optical trap obey the following relationship:

$$|\boldsymbol{F}| = Q\frac{n_2 P}{c} \tag{43}$$

where n_2 is the refractive index of the surrounding fluid, P is the incident laser optical power, c is the speed of light in vacuum, and Q is a quality factor which depends on the size of the sphere and the index difference between the sphere and the fluid. Dimensional analysis of this equation reveals why one would expect pN forces from a mW laser.

§A.2.2 THE IMAGING SYSTEM

To image the trapped particles, an inverted microscope is realized using the same arrangement of optics as also shown in . A white light source provides incoherent imaging light which travels through our trapping system in the reverse direction. White light passes from a lamp into the condenser, through the sample (without affecting the trapped particle(s)), through the objective, through the dichroic mirror (minus the reflected wavelengths), into a mirror M, through a filter (not pictured), into a lens L3 which focuses the image onto the sensor of a charge coupled device (CCD) high definition camera.

§A.2.3 THE TRAPPING REGION

The design of the sample holder is an important feature to consider when designing an OT system. The microscope objective's working distance determines how far the focal point is from the top surface of the objective. This parameter imposes constraints on the design of the trapping region. The working distance for the objective used in our system is 0.23 mm, so the trapping region's dimensions below the trap must be within that range. Using a microscope coverslip with a specified thickness of 0.15 mm, this allows the trap to reside approximately 80 μm above the surface of the glass coverslip. Figure 57 shows the trapping region and the various relevant geometries surrounding the optical trap.

Initial testing of the OT system was performed using a simple 3D printed sample tray which had a recess to hold a coverslip. Thereafter, a flow chamber was designed and 3D printed that could be used for flowing specimens into the trapping region. Figure 58 shows a cross-section of the designed OT flow chamber which includes an appropriately designed trapping region, recesses for Teflon gaskets, and a recess for the microscope objective.

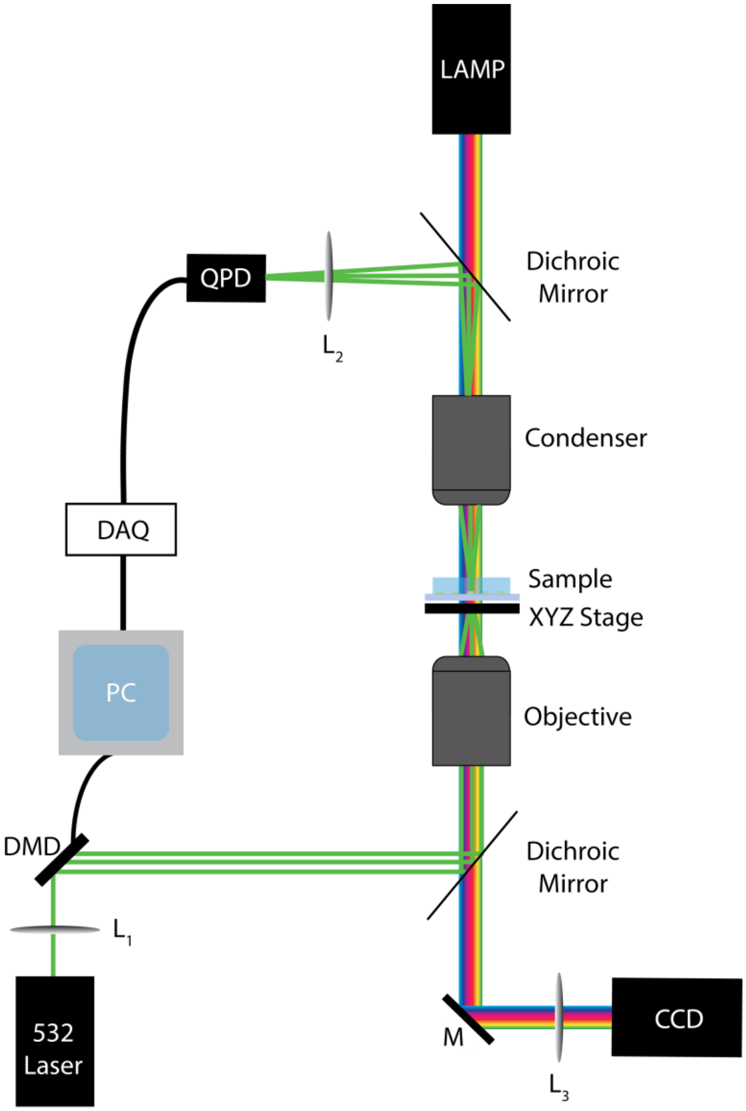

Figure 56: Optical tweezing system for colloidal particle trapping.

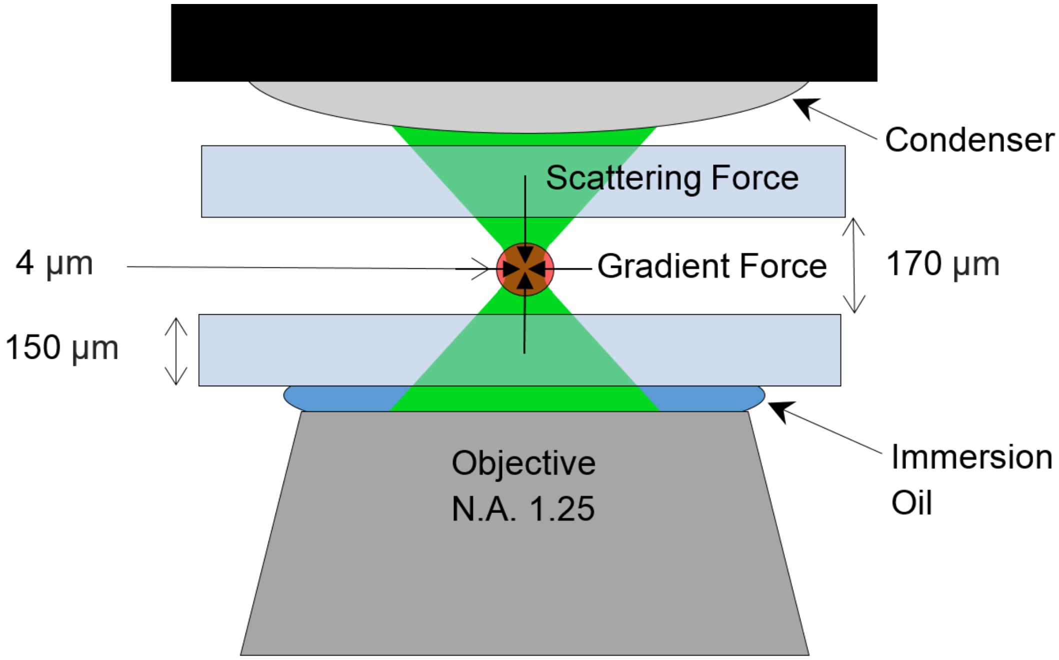

Figure 57: Trappring region within the sample.

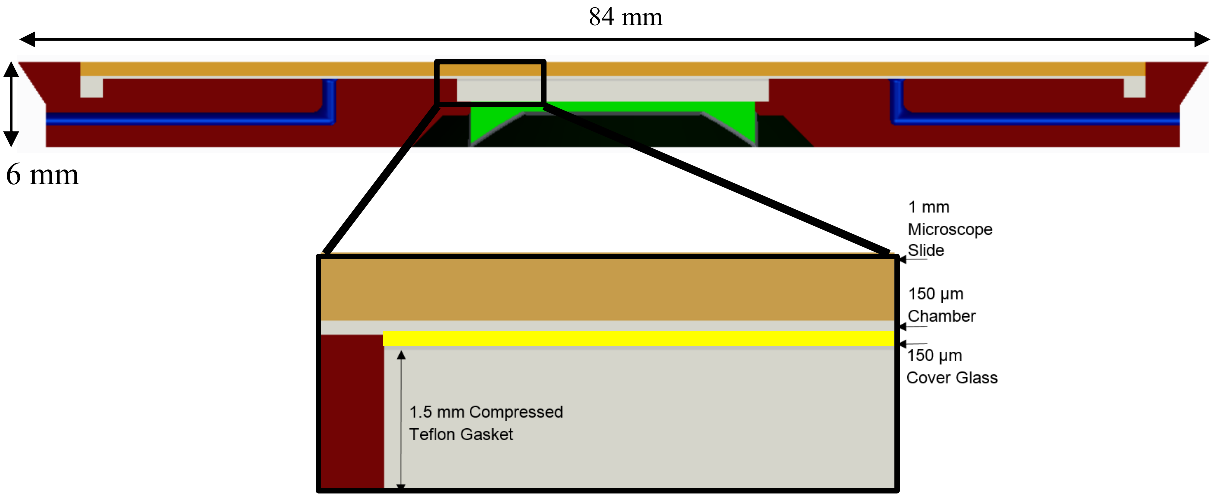

Figure 58: OT flow chamber with exploded view highlighting the trapping region in yellow.

§A.3 SYSTEM CHARACTERIZATION

To determine the optical power at the microscope objective, one must measure the optical power loss after each element along the optical path length of the laser beam. Figure 59 shows a histogram that tracks the optical loss due to the optical components along the optical path length of the laser beam which was obtained using an optical power meter. The physical realization of this combined trapping and imaging system is shown in Figure 60, where the optical components are labeled in this figure corresponding to their position along the optical path length of the beam.

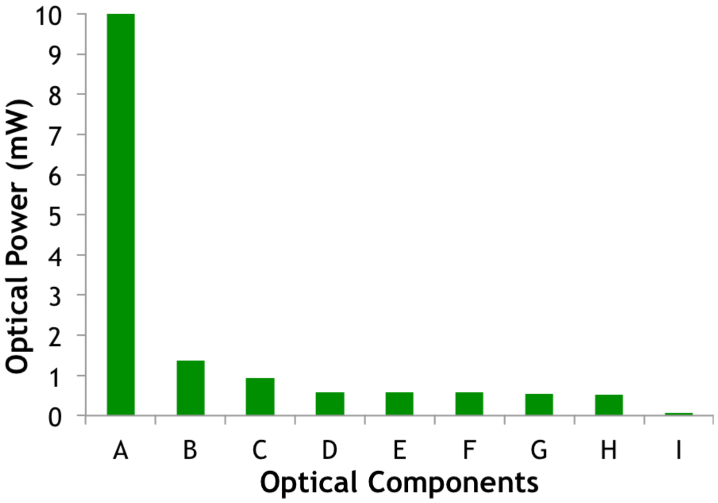

Figure 59: Power loss associated with various optical components along the optical path length in the OT system.

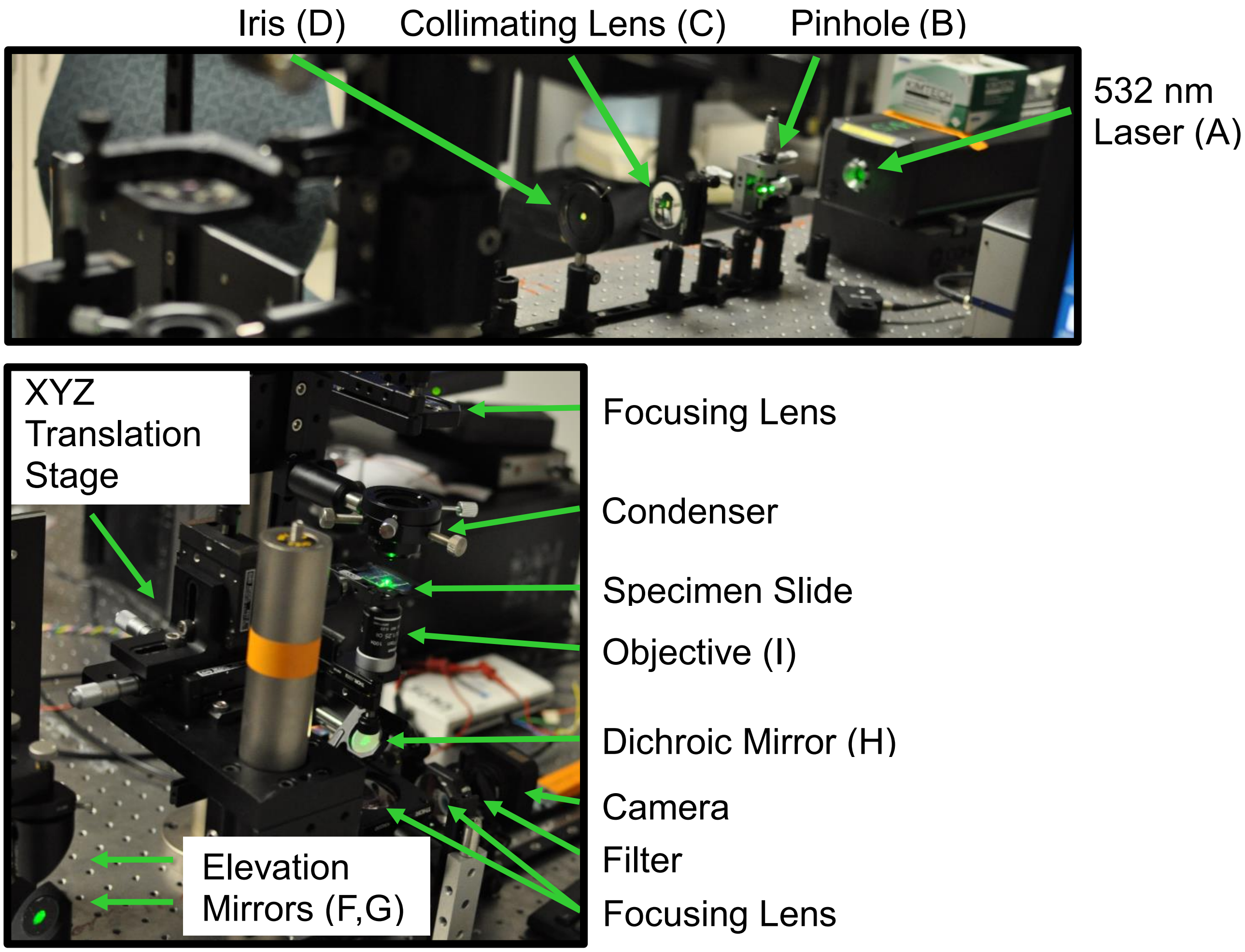

Figure 60: OT setup and associated optical elements.

To move the optical trap and thus the trapped particle, a steering system is needed. To translate the particle within the 2D sample plane, we implemented the use of a DMD. To be certain that the DMD surface would perform as well as a conventional mirror, we characterized its surface using a Shack-Hartmann wavefront sensor (WFS) system (Adaptive Optics Associates Wavescope). Upon reflection of a clean beam (pin hole and iris) from the surface of a clean DMD (Isopropyl alcohol then compressed N_2 let onto sample) into the WFS which measures the wavefront deviation from a reference wavefront and calculates Zernike coefficients which can be plotted to reproduce the wavefront. Figure 61 shows an *XY*-plane cross section (where *z* is the direction of propagation in Cartesian coordinates) taken at the mean amplitude position in the *z*-direction. Figure 62 shows the full 3D plot of the reconstructed DMD wavefront. The reconstructed DMD wavefronts are determined by the WFS and plotted using MATLAB.

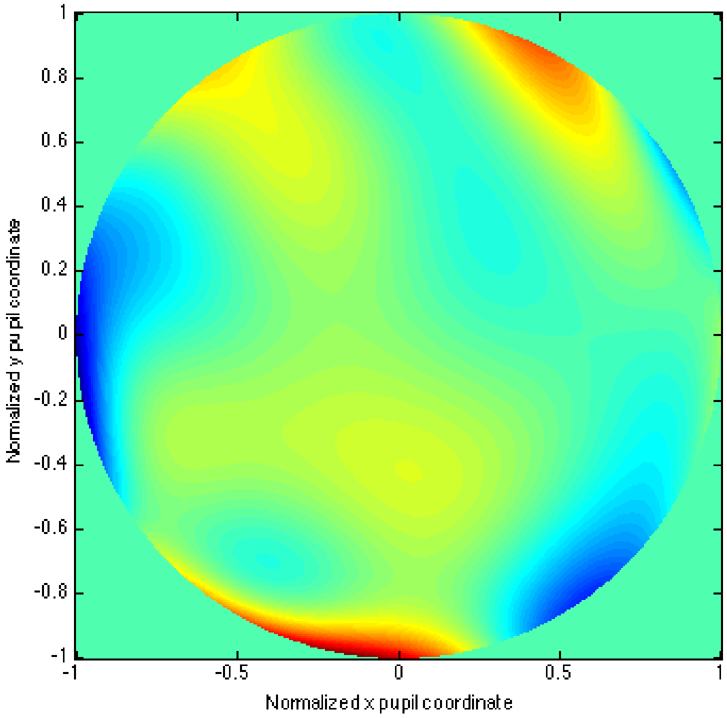

Figure 61: *XY* cross section (z - direction of propagation) of reconstructed DMD wavefront.

In addition to the wavefronts, the point spread function (PSF) was calculated for the DMD by the WFS. The PSF is the DMD's response to a point source and is shown in the usual way in Figure 63.

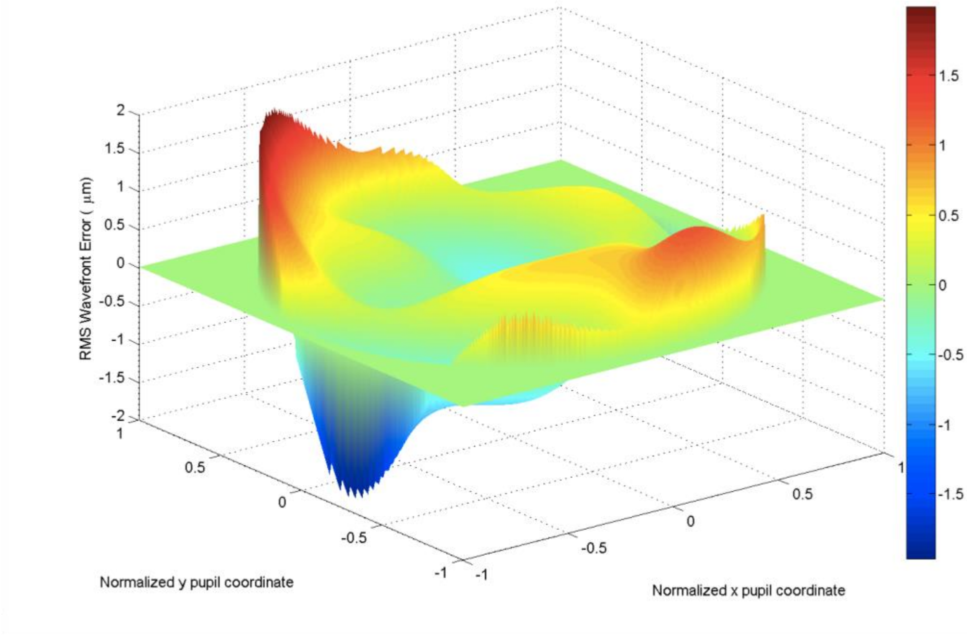

Figure 62: 3D DMD reconstructed wavefront.

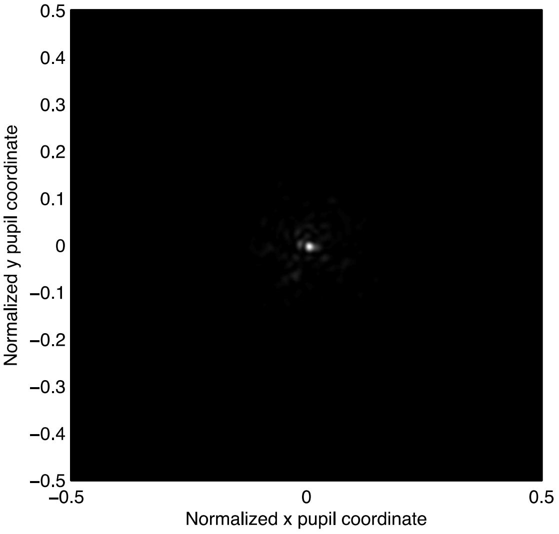

Figure 63: PSF for the DMD.

§A.4 INITIAL TESTING

To demonstrate the viability of the OT system, test particles were trapped and their motion was captured using the imaging system. Using 3 μm radii PS microspheres obtained from Bangs Labs, shows the stable trapping of a microsphere as a time sequence of micrographs obtained from the CCD camera of the OT system. In this series of images there are a few other microspheres in the vicinity of the trap and there is a microsphere already in the optical trap which is out of the focal plane during this experiment. The time interval between t_0 and t_1 and also between t_1 and t_2 is approximately 5 seconds, as the microsphere is dragged slowly through the fluid due to the gradient force associated with the trap.

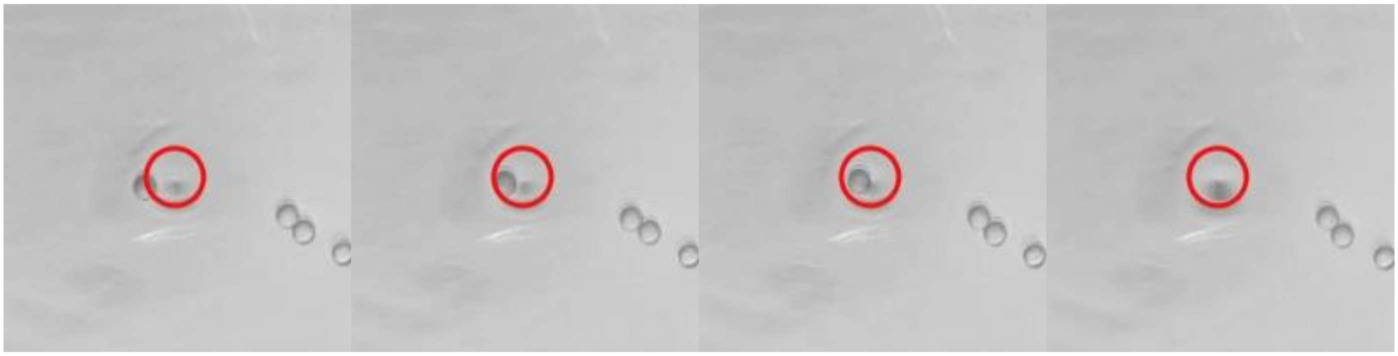

t_0 t_1 t_2 t_3

Figure 64: Time sequence of a microsphere being trapped in the OT system.
Red ring has a radius of 6 μm.

APPENDIX B: TABLES AND CODE

§B.1 PLASMONIC BIOSENSOR FOM COMPARISON TABLES

Table 1: Refractive index sensitivities and FOM values of plasmonic metal nanostructures for LSPR sensors without the occurrence of Fano resonance in the research community.[46]

Reference	Nanostructures	Single or ensemble	Resonance wavelength (nm/eV)*b*	FWHM (nm/eV)*b*	Sensitivity (nm/eV per RIU)*b*	FOM
Wang, Langmuir 2008, 24, 5233	Au nanospheres	Ensemble	527/2.353	73/0.327	44/0.196	0.6
Wang, Langmuir 2008, 24, 5233	Au nanostars	Ensemble	1141/1.087	878/0.981	703/0.785	0.8
Halas, J. Phys. Chem. B 2004, 108, 17290	(Au core)/(SiO2 shell)	Ensemble	770/1.61	350/0.732	314/0.657	0.9
Xia, Anal. Chem. 2002, 74, 5297	(Au core)/(AuS shell)	Ensemble	700/1.77	400/1.012	409/1.035	1.0
Halas, Nano Lett. 2006, 6, 827	Au nanowires	Ensemble	1600/0.775	600/0.291	801/0.388	1.3
Mulvaney, Langmuir 1994, 10, 3427	Au nanospheres	Ensemble	530/2.34	60/0.265	90/0.397	1.5
Raschke, Nano Lett. 2004, 4, 1853	(Au core)/(AuS shell)	Single	660/1.88	77/0.22	117/0.333	1.5
Wang, Langmuir 2008, 24, 5233	Au nanocubes	Ensemble	538/2.305	55/0.236	83/0.354	1.5
Van Duyne, Nano Lett. 2005, 5, 2034	Ag nanocubes	Single	510/2.43	91/0.433	146/0.695	1.6
Wang, Langmuir 2008, 24, 5233	Au nanorods	Ensemble	846/1.466	169/0.296	288/0.504	1.7
Wang, Langmuir 2008, 24, 5233	Au nanobipyramids	Ensemble	645/1.922	88/0.264	150/0.449	1.7

Van Duyne, J. Am. Chem. Soc. 2001, 123, 1471	Ag nanoprisms	Ensemble	564/2.2	104/0.405	191/0.745	1.8
Hafner, Nano Lett. 2006, 6, 683	Au nanostars	Single	675/1.84	125/0.34	238/0.649	1.9
Wang, Langmuir 2008, 24, 5233	Au nanorods	Ensemble	728/1.703	107/0.251	224/0.528	2.1
Mock, Nano Lett. 2003, 3, 485	Ag nanospheres	Single	520/2.38	73/0.335	160/0.734	2.2
Wang, Langmuir 2008, 24, 5233	Au nanorods	Ensemble	653/1.899	75/0.219	195/0.57	2.6
Wang, Langmuir 2008, 24, 5233	Au nanobipyramids	Ensemble	735/1.687	76/0.174	212/0.488	2.8
Van Duyne, Nano Lett. 2003, 3, 1057	Ag nanoparticles	Single	585/2.12	49/0.178	203/0.736	4.1
Wang, Langmuir 2008, 24, 5233	Au nanobipyramids	Ensemble	886/1.4	93/0.148	392/0.621	4.2
Mock, Nano Lett. 2003, 3, 485	Ag nanoprisms	Single	760/1.63	80/0.172	350/0.751	4.4
Wang, Langmuir 2008, 24, 5233	Au nanobipyramids	Ensemble	1096/1.131	120/0.124	540/0.559	4.5
Hafner, Nano Lett. 2006, 6, 683	Au nanostars	Single	770/1.61	124/0.26	664/1.41	5.4
Van Duyne, Nano Lett. 2005, 5, 2034	Ag nanocubes on substrates	Single	430/2.88	22/0.146	118/0.792	5.4

Table 2: Refractive index sensitivities and FOM values of plasmonic metal nanostructures for LSPR sensors with the occurrence of Fano resonance in the research community.[46]

Reference	Nanostructures	Single or ensemble	Resonance wavelength		FWHM		Sensitivity		FOM
			nm	eV	nm	eV	nm per RIU	eV per RIU	
Huang, Appl. Phys. Lett. 2012, 100, 173114	Au nanorings	Array	798		112		350		3.1
Verellen, Nano Lett. 2011, 11, 391	"XI" nanostructures	Single	1305		145		685		4.7
Nordlander, Nano Lett. 2010, 10, 3184	Au nanodisks	Cluster	900			0.093		0.53	5.7
Lodewijks, Nano Lett. 2012, 12, 1655	Au nanodisks	Array	850		25		208		8.3
Atwater, ACS Nano 2011, 5, 8167	Split-ring resonators	Array	1420		141		1192	0.497	8.5
Atwater, ACS Nano 2011, 5, 8167	Split-ring resonators with bars	Single	1450		121		1225	0.488	10.1
Jin, Plasmonics 2013, 8, 885	Au nanoprisms	Prism dimer	1300			0.062		0.99	16.1
Lodewijks, Nano Lett. 2012, 12, 1655	Au nanorings	Array	980		23		380		16.5
Nordlander, Nano Lett. 2011, 11, 1657	Ag nanocubes	Single	400			0.065		1.3	20
Cattoni, Nano Lett. 2011, 11, 3557	Microcavities	Array	900		19		405		21

§B.2 MATLAB CODE USED TO CONTROL THE VISTEC 5200 E-BEAM FOR THE FABRICATION OF THE CNP ARRAYS

The code below was created by Chad Eichfeld and Brandon Terranova:

```
CircleRadius=140;  %in nanometers
InnerRingR1=57.5; %smaller in nanometer
InnerRingR2=62.5;%larger in nanometers
ArraySize=1; %timestorepeatstructunitinnxandyforeachunitcell
ArraySizeTotal=4489; %timestorepeatcellinnxandy mulitply both to get
total
BeamStepSize=5; %in nanometers
Resolution=0.0005; %subfield resolution in microns
MainFieldRes=.001;
Multiplier=BeamStepSize/(Resolution*1000); %multiplier for BSS>jumps
SquareSize=1500; %in nanometers ie period
CenterX=SquareSize/2; %X coordinate for the center point of the circle
CenterY=SquareSize/2; %Y coordinate for the center point of the circle
NumberLines=SquareSize/BeamStepSize;
Layer=1; %layer to replace
DataLayer=0; %datalayer to replace
RectHeight=SquareSize * ArraySize /1000; %height of box to replace in um
RectWidth=SquareSize * ArraySize/1000; %width of box to replace in um
NumberOfRings=((InnerRingR2-InnerRingR1)/BeamStepSize);
filename='A1';

fid2 = fopen([filename '.seq'],'w');
fid3 = fopen([filename '.txl'],'w');

stringtemp='';

%%%Start Writing seq File
stringtemp=sprintf('%s BEAMER_GPF_Sequence_Definition\r\n',stringtemp);
stringtemp=sprintf('%s \r\n',stringtemp);
stringtemp=sprintf('%s SubFieldResolution
%.4f\r\n',stringtemp,Resolution);
stringtemp=sprintf('%s BeamStepSize
%.4f\r\n',stringtemp,BeamStepSize/1000);
stringtemp=sprintf('%s \r\n',stringtemp);
stringtemp=sprintf('%s !Sequence Definition\r\n',stringtemp);
stringtemp=sprintf('%s Replace Rect %.0f(%.0f) %.3f %.3f
\r\n',stringtemp,Layer,DataLayer,RectWidth,RectHeight);



stringtemp=sprintf('%s Sequence Lineclear X 0 reljmp\r\n',stringtemp);


YcircleMax=(CenterY+CircleRadius)/BeamStepSize;
YcircleMin=(CenterY-CircleRadius)/BeamStepSize;
YringR1Max=(CenterY+InnerRingR1)/BeamStepSize;
YringR1Min=(CenterY-InnerRingR1)/BeamStepSize;
YringR2Max=(CenterY+InnerRingR2)/BeamStepSize;
YringR2Min=(CenterY-InnerRingR2)/BeamStepSize;

IndexX=1; IndexXY=1;
Xn=0;Yn=0;
```

```
fprintf(fid2,stringtemp);
stringtemp='';

for ArrayY=1:1:(ArraySize)

    for ArrayX=1:1:(ArraySize)
    LineY=(SquareSize*(ArrayY-IndeXY));
    LineX=(SquareSize*(ArrayX-IndexX));
    Xjump=-1*(Xn)*Multiplier;
    Yjump=-1*(Yn)*Multiplier;
    IndexX=ArrayX; IndeXY=ArrayY; Xn=0;Yn=0;
    stringtemp=sprintf('%s
!index=%.0f,%.0f\r\n',stringtemp,ArrayX,ArrayY);
    stringtemp=sprintf('%s Sequence Jump %.0f %.0f
BBONJMP\r\n',stringtemp,Xjump,Yjump);
    stringtemp=sprintf('%s Sequence Line X %.0f
BBONSTEPS\r\n',stringtemp,(LineX/BeamStepSize));
    stringtemp=sprintf('%s Sequence Line Y %.0f
BBONSTEPS\r\n',stringtemp,(LineY/BeamStepSize));
    stringtemp=sprintf('%s Sequence Line X 0 reljmp\r\n',stringtemp);

    %NumberLines=1;
        for Y=0:1:NumberLines
            for X=0:1:NumberLines
                if Y < YcircleMin || Y > YcircleMax
                Xjump=(X-Xn)*Multiplier;
                Yjump=(Y-Yn)*Multiplier;
                stringtemp=sprintf('%s Sequence Jump %.0f %.0f
JMP\r\n',stringtemp,Xjump,Yjump);
                Xn=X;
                Yn=Y;
                else
                Xsq=realsqrt((CircleRadius^2)-(((Y*BeamStepSize)-
CenterY)^2));
                X1=(CenterX-Xsq)/BeamStepSize;
                X2=(CenterX+Xsq)/BeamStepSize;
                    if X < X1 || X > X2
                    Xjump=(X-Xn)*Multiplier;
                    Yjump=(Y-Yn)*Multiplier;
                    stringtemp=sprintf('%s Sequence Jump %.0f %.0f
JMP\r\n',stringtemp,Xjump,Yjump);
                    Xn=X;
                    Yn=Y;
                    end
                end

            end
            fprintf(fid2,stringtemp);
               stringtemp='';
        end

            for Rn=0:1:NumberOfRings
                Radius=InnerRingR1+(Rn*BeamStepSize);
                AngleIncrement=asind(BeamStepSize/Radius);
                for Angle=0:AngleIncrement:359
                    %convert degrees to radians
                    AngleRad = Angle * (3.141592654 / 180);
                    %convert polar to rect coordinates
                    X = (Radius * cos(AngleRad)) + CenterX;
                    Y = (Radius * sin(AngleRad)) + CenterY;
                    X = round(X*Multiplier/BeamStepSize)/Multiplier;
%round to nearest res unit
```

```
                    Y = round(Y*Multiplier/BeamStepSize)/Multiplier;
%round to nearest res unit
                    Xjump=round((X-Xn)*Multiplier); %round to nearest
res unit
                    Yjump=round((Y-Yn)*Multiplier); %round to nearest
res unit
                    stringtemp=sprintf('%s Sequence Jump %.0f %.0f
JMP\r\n',stringtemp,Xjump,Yjump);
                    Xn=X;
                    Yn=Y;
                end
                fprintf(fid2,stringtemp);
                stringtemp='';
            end

    end
end
stringtemp=sprintf('%s Sequence Jump 0 0 \r\n',stringtemp);
fprintf(fid2,stringtemp);
stringtemp='';


%%%Start Writing TXL File
fprintf(fid3,'LETXTLIB 1.0.0\r\n');
fprintf(fid3,'UNIT MICRON\r\n');
fprintf(fid3,'RESOLVE %.4f\r\n',BeamStepSize/1000); %set resolution to
BSS
fprintf(fid3,'BEGLIB\r\n');
fprintf(fid3,'\r\n');
fprintf(fid3,'STRUCT Square\r\n');
fprintf(fid3,'LAYER %.0f\r\n',Layer);
fprintf(fid3,'DATATYPE %.0f\r\n',DataLayer);
fprintf(fid3,'B -%.5f,-%.5f %.5f,-%.5f %.5f,%.5f -%.5f,%.5f ENDB\r\n'...

,RectWidth/2,RectHeight/2,RectWidth/2,RectHeight/2,RectWidth/2,RectHeigh
t/2,RectWidth/2,RectHeight/2);
fprintf(fid3,'ENDSTRUCT\r\n');
fprintf(fid3,'\r\n');
fprintf(fid3,'STRUCT Array\r\n');
fprintf(fid3,'AREF Square 0.00000,0.00000 %.0f %.5f,0.00000 %.0f
0.00000,%.5f\r\n',ArraySizeTotal,RectWidth,ArraySizeTotal,RectHeight);
fprintf(fid3,'ENDSTRUCT\r\n');
fprintf(fid3,'\r\n');
fprintf(fid3,'ENDLIB\r\n');

%%Count number of jumps
text=fileread([filename '.seq']);
jumps=strfind(text, 'JMP');
numberjumps=numel(jumps);
stringtemp=sprintf('%s !Number of jumps %.0f',stringtemp,numberjumps);
area=BeamStepSize*numberjumps;
stringtemp=sprintf('%s \r\n',stringtemp);
stringtemp=sprintf('%s !Total area %.0f',stringtemp, area);
newsquaresize=sqrt(area);
roundedsquaresize=round(newsquaresize);
stringtemp=sprintf('%s \r\n',stringtemp);
stringtemp=sprintf('%s !Square size %.0f
nm',stringtemp,roundedsquaresize);
bias=((RectHeight*1000)-(roundedsquaresize))/2;
stringtemp=sprintf('%s \r\n',stringtemp);
stringtemp=sprintf('%s !Bias %.0f nm',stringtemp,bias);
fprintf(fid2,stringtemp);
stringtemp='';
```

VITA

BRANDON TERRANOVA
bbt25@drexel.edu
3141 Chestnut St.
Philadelphia, PA 19104
(215) 512-2642

RESEARCH INTERESTS

Light-matter interactions, plasmonics, optical tweezing, light guiding, optical nanomanufacturing and electromagnetic trapping.

EDUCATION

Drexel University
Doctor of Philosophy in Electrical Engineering/Electrophysics, November 2015
Thesis: *The Physics and Applications of a 3D Plasmonic Nanostructure*

Binghamton University, SUNY
Master of Science in Physics, May 2009
Thesis: *Design and Optimization of VCSEL-based Optical Interconnects on Package*

University of Delaware
Bachelor of Science in Physics, May 2005
Minor in Mathematics

PROFESSIONAL EXPERIENCE

Assistant Teaching Professor, April 2015—Present
Drexel University, College of Engineering
In this role, I am responsible for ENGR100, 101, 102, and 103 which comprise an introduction to CAD, and the three part freshman design course sequence.

Instructor and Laboratory Manager, November 2009—March 2015
Drexel University, Department of Mechanical Engineering and Mechanics (MEM)
Along with other instructors, I am responsible for MEM311, MEM331 and MEM351 which take place on Drexel and Burlington County Community college campuses. I have taught all three courses and developed video lectures for all content in those courses. I manage all equipment necessary for these laboratory-based courses, and continually develop course material along with the professors. I work closely with undergraduates on senior design and other projects involving laboratory equipment and research.

- Taught and developed content for MEM311, MEM331 and MEM351.
- Managed 8 different workstudies between 2012-2014

- Assist with various computer, building, and technological projects and problems within the department.
- Work with Drexel Health and Safety to coordinate safety instruction, audit and maintenance.
- Assisted with renovations to the MEM undergraduate lab in 2012, 2013, and 2014.

Adjunct Professor, October 2009—May 2011
Missouri College Online
I have been teaching introductory math courses part-time online at this professional school which caters primarily to the healthcare sector.

- All grading and preparation of powerpoints, rubrics and homework assignments.
- Developed introductory physics course (Phys113)

Research Assistant, July 2007—May 2009
SUNY Binghamton, Binghamton, NY
Our research was primarily concerned with the design and testing of waveguiding structures suitable for use in planar lightwave circuits intended for use in optical interconnects.

- Use CAD and beam simulation (FDTD and BPM routines) software to evaluate waveguiding structures
- Design, create and run laboratory experiments
- Selection and ordering of scientific equipment/software

Teaching Assistant, July 2008—May 2009
SUNY Binghamton, Binghamton, NY

- Summer 2008: Phys121 Physics 1 (non-calculus based physics)
- Fall 2008: Phys131 Physics 1 (calculus based physics)
- Spring 2008: Phys131 and Phys122 (non-calculus based EM, was responsible for managing other TAs)

Teacher, October 2004—June 2007
St. Mark's HS, Wilmington, DE
Was a full-time teacher at St. Mark's High School where I taught General Science to freshman, and Physics to seniors.

- Six lectures/labs a day for three years. Taught over 550 students in total.
- Held three workshops for teachers in a school-wide technology immersion project
- Designed over 200 original assignments/quizzes/tests/labs/presentations/projects

AWARDS/MEMBERSHIPS

- Sigma Pi Sigma, Physics Honors Society
- Eta Kappa Nu, IEEE Honors Society
- Society of Physics Students, President and Founder of University of Delaware Chapter
- GAANN Fellow, 2014
- SPIE member
- IEEE member

EQUIPMENT AND LABORATORY SKILLS

Various educational equipment	Perkin-Elmer DSC-7 DSC
Various mechanical and electronics testing tools	Prusa i3 3D printer/Makerbot Replicator 2
Dimatix Inkjet printer	Thermionics Thermal Evaporator VE 90
Ecomet 3 and Metprep 3 polishing tools	Vistec EBPG5200 Electron Beam Lithography
FEI Strata DB235 Focused Ion Beam	Wavescope Shack-Hartmann wavefront sensor
Laurell WS 650 Spin Coater	Zeiss EVO50XVP SEM
Newport DC Linear Stages/ESP300 controller	Zeiss Supra 55 SEM
Nikon Epiphot 200 Light Microscope	Zygo NewView 7300 Profilometer
Nikon D40 and D5000 Digital SLR Camera	

COMPUTER AND SOFTWARE SKILLS

100+ PC builds	Maple, Mathematica, MatLab
Adobe Photoshop CS3/CS4, Dreamweaver CS3/CS4, Illustrator CS3/CS4	Microsoft Office (Word, Excel, Publisher, Powerpoint)
RSoft BeamProp (BPM software)	Microsoft Windows XP, Vista, 7
RSoft FullWave (FDTD software)	PTC Creo, Sketchup, Anim8or
Lumerical FDTD solutions	Various audio and video editing programs
Mac OSX	HTML, LabVIEW, Fortran 90, and LaTeX

STUDENTS/PROJECTS ADVISED

1. George Cimini, STAR student 2012: "Construction of Optical Tweezers"
2. Freshman design team (John Sommer, Nathan Wall, Brett Moore, Chase Connell, Johnny Clark) 2014: "Portable Optical Tweezers for Undergraduate Education"
3. Nathan Wall, STAR student 2014: "Towards Aerosol Optical Tweezers"

WORKSHOPS

1. Technology Immersion Project at St. Mark's high school: "Garageband in the classroom", 2005.
2. Technology Immersion Project at St. Mark's high school: "Multimedia for teaching", 2005.
3. DIY 3D printers for Drexel research, *in preparation*

SPONSORED RESEARCH ACTIVITIES

1. "Design and Optimization of Optical Interconnects", CAM research center, Binghamton University, 2007-2009.
2. "Solution processing of thin films for FIPEL technology", CeeLite Technologies, Drexel University, 2014.

SELECTED CONFERENCE/UNIVERSITY/COMPANY PRESENTATIONS

1. EM Trapping and Plasmonics, Invited Lecture, Drexel University, December 2014.
2. The world of 3D printing, Outreach event, Greenfield elementary school, November 2014.
3. 3D Printing Design for Practical Applications, Invited Lecture, Drexel University, November 2014.
4. Cylindrical channel plasmon resonance for refractometric sensing, SPIE Photonics West, February 2014.
5. Poster on Cylindrical channel plasmon resonance for refractometric sensing, U.S. Army Armament Research, Development and Engineering Center, Drexel University, February 2014.
6. 3D printing technology at Drexel University, MEM Seminar, Drexel University, November 2013.
7. Polaritonic metamaterial for super-resolution trapping and sensing, IEEE Photonics Conference, September 2013.
8. Fano resonance in plasmonic coaxial nanopillars, Nanophotonics symposium, Drexel University, September 2013.
9. Poster on Polaritonic metamaterial for super-resolution trapping and sensing, Research Day, Drexel University, March 2013.
10. Plasmonic nanostructures for nanomanipulation, Nanophotonics symposium, Drexel University, September 2012.
11. Holographic optical tweezers for bulk nanowire alignment, Nanophotonics symposium, Drexel University, September 2011.

12. Progress on design and optimization of optical interconnects on package, presented to the Technical Advisory Board for Small Scale Systems Integration and Packaging Center, June 2009.
13. Poster on design and optimization of optical interconnects on package, presented to the Technical Advisory Board for Small Scale Systems Integration and Packaging Center, June 2008.
14. Progress on design and optimization of optical interconnects on package, presented to the Technical Advisory Board for Small Scale Systems Integration and Packaging Center, November 2007.
15. Berry’s phase in spin-orbit interactions, presented to the Quantum Transport Theory Group, University of Delaware, August 2004.

PUBLICATIONS

1. Terranova, B., Wall, N., Waring, M., and Fontecchio, A., ***Submicron aerosol optical tweezers using structureless surface plasmons***, journal article, *in preparation.*
2. Terranova, B., Wall, N., Waring, M., and Fontecchio, A., ***Optical tweezers using structureless surface plasmons***, META 2015 conference proceedings, *in preparation.*
3. Terranova, B., Bellingham, A., and Fontecchio, A., ***Plasmonic coaxial nanopillar refractometric biosensor***, Advanced Materials, *in preparation*.
4. Terranova, B. and Fontecchio, A., ***Tunable Fano resonance of whispering gallery modes from out-of-plane structural symmetry breaking***, Nature Nanotechnology, *in preparation*.
5. Terranova, B., ***The Physics and applications of a 3D plasmonic nanostructure***, PhD dissertation, Drexel University, 135 pgs., 2015.
6. Terranova, B., Bellingham, A., Herbert, S., Fontecchio, A. ***Cylindrical channel plasmon resonance for single-molecule sensing***, SPIE Proceedings, 2014.
7. Terranova, B. and Fontecchio, A. ***Metamaterial for Trapping and Sensing Applications***, IEEE Xplore Conference Proceedings, 2013.
8. Terranova, B., Wargo, E., Agar, E., Dennison, C., Kumbur, E.C., Stacck, D., Farouk, B., ***MEM311 Thermal & Fluid Science Laboratory Manual***, Drexel University, 78 pgs., 2010.
9. Terranova, B., ***Design and Optimization of VCSEL-Based Optical Interconnects on Package***, Master’s Thesis, Binghamton University, 154 pgs., 2009.
10. Terranova, B., ***Learning at the Speed of Light***, Book, *in preparation.*
11. Terranova, B., ***SPS Newsletter,*** Four published articles, 2005.

REFERENCES

Adam Fontecchio,
Professor
Drexel University
(215) 895 0234
fontecchio@ece.drexel.edu

Oana Malis,
Associate Professor
Purdue University
(765) 494 3039
omalis@purdue.edu

Charles Nelson,
Professor
SUNY Binghamton
(607) 777 4317
cnelson@binghamton.edu